

A BROAD BANDWIDTH SUM FREQUENCY GENERATION
SPECTROSCOPIC INVESTIGATION OF ORGANIC LIQUID SURFACES

DISSERTATION

Presented in Partial Fulfillment of the Requirements for
the Degree Doctor of Philosophy in the Graduate
School of The Ohio State University

By

Elizabeth L. Hommel, M.S.

The Ohio State University
2003

Dissertation Committee:

Professor Heather Allen, Advisor

Professor Sherwin Singer

Professor James Coe

Approved by

Advisor
Department of Chemistry

ABSTRACT

Advances in surface broad bandwidth sum frequency generation (BBSFG) spectroscopy and investigations of liquid surfaces are discussed in this dissertation. The technique implemented uses a double amplifier ultrafast laser system to produce a narrow bandwidth visible beam and a broad bandwidth infrared beam. The two beams are overlapped in time and space on a liquid surface to produce a broad bandwidth sum frequency signal. The double amplifier system allows for higher peak powers resulting in a stronger sum frequency generation response from characteristically low signal liquid surfaces. Several organic liquids are investigated using BBSFG spectroscopy and Raman spectroscopy to investigate the surface structure and the bulk liquids, respectively. The series of liquids selected are applicable to atmospheric aerosol processing. Initially, a surrogate hydrophilic compound ethylene glycol was investigated. In addition to ethylene glycol, several aromatic compounds were probed at their air-liquid interfaces. The aromatic compounds studied were benzene, toluene, ethylbenzene, o-xylene, m-xylene, p-xylene, and mesitylene. The final aromatic compound to be studied was 1-methyl naphthalene. The surface of the neat 1-methyl naphthalene liquid is dramatically altered upon the addition of small amounts of water into the bulk liquid.

ACKNOWLEDGMENTS

I wish to thank Professor Heather Allen for being more than an advisor. She has been a mentor and a friend. She has given me the support and encouragement, which made it possible for me to accomplish the research necessary to complete this degree. I also wish to thank all of the Allen Lab members. In particular, Dr. Gang Ma has been a friend for the last three years. He is always quick to help wherever possible. Lisa Van Loon has been a great friend and my personal trainer keeping me in the gym on a regular basis. The workouts allowed me to maintain the level sanity necessary to finish the work. Jacob Schlegel has provided the chocolate necessary for this work to proceed and Jacob has helped wherever possible.

I also want to thank Dennis Walsh. He is my best friend, providing a lot of encouragement and support. My family has also been very important for the achievement of this goal. My mother has always encouraged me to work towards my goal and stop nothing short.

I acknowledge The Ohio State University Environmental Science Molecular Institute (EMSI) for financial support. It has been exciting to be involved in the EMSI from the beginning. The EMSI selected me to attend the National Coalition for Scientific Funding in Washington, D. C. This is an opportunity very few students get to experience.

VITA

July 29, 1969 Born – Houston, Texas

1991 – 1992 Undergraduate Teaching Assistant
University of North Texas

1992 Undergraduate Research Assistant
University of North Texas

1993 B. S. Chemistry
University of North Texas

1993 – 1994 High School Chemistry Teacher
Midlothian High School

1994 – 1995 Graduate Teaching and Research Assistant
University of North Texas

1995 M. S. Chemistry
University of North Texas

1995 – 2000 Graduate Teaching and Research Assistant
University of Oregon

2000 – 2003 Graduate Research Assistant
The Ohio State University

PUBLICATIONS

Research Publications

1. E. L. Hommel, G. Ma and H. C. Allen, "Broadband Vibrational Sum Frequency Generation Spectroscopy of a Liquid Surface", *Analytical Sciences*, 2001, V17, Issue 11, pp. 1325-1329.
2. E. L. Hommel and H. C. Allen, "Broadband Sum Frequency Generation with Two Regenerative Amplifiers: Temporal Overlap of Femtosecond and Picosecond Light Pulses", *Analytical Sciences*, 2001, V17, Issue 1, pp. 137-139.
3. A. Goumri, D. Laakso, J-D. Rocha, E. Francis [Hommel] and P. Marshall, "An Investigation of the Gas-Phase Kinetics of the Reaction $K + SO_2 + Ar$ ", *Journal of Physical Chemistry*, 1993, V97, Issue 20, pp. 5295-5297.

FIELDS OF STUDY

Major Field: Chemistry

TABLE OF CONTENTS

	Page
Abstract.....	ii
Acknowledgments.....	iii
Vita.....	iv
List of Tables	viii
List of Figures	ix
List of Abbreviations	xii
Chapter:	
1. Introduction	1
Ethylene Glycol / Water.....	2
Benzene and Benzene Derivatives.....	2
Benzene, Toluene, m-Xylene, and Mesitylene	3
Toluene and Ethylbenzene	4
Xylene.....	4
1-Methyl Naphthalene and the Hydration Effects	4
Sum Frequency Generation Background	7
2. Building the Laser System	10
2.1 Broadband Sum Frequency Generation with Two Regenerative Amplifiers: Temporal Overlap of Femtosecond and Picosecond Light Pulses	10
Introduction.....	10
BBSFG System	12
Conclusion	17
2.2 BBSFG from a Liquid Surface.....	18
Introduction.....	18

Experimental	20
Results and Discussions	23
Summary	29
3. Ethylene Glycol–A Model Hydrophilic Aerosol	31
Introduction	31
Experimental	31
Results and Discussion	33
Summary	38
4. Benzene, Toluene, m-Xylene, and Mesitylene: A Series of Methyl Substituted Benzenes	41
Introduction	41
Experimental	41
Results and Discussion	44
Conclusions	55
5. BBSFG of Benzene Derivatives at Their Respective Air–Liquid Interfaces	58
Introduction	58
Experimental	58
5.1 Toluene and Ethylbenzene	61
Results and Discussion	61
Conclusions	66
5.2 Xylenes	66
Results and Discussion	66
Conclusions	69
6. Observation of the Hydrophobic Effect at the Air–Hydrated 1-Methyl Naphthalene Interface	71
Introduction	71
Experimental	71
Results and Discussion	74
Atmospheric Implications	84
Conclusions	87
References	88
Appendix A – Coherent Peak Profile Fits Using Igor	95
A.1 The Lorentzian Profile	95
A.2 The Voigt Profile	97
A.3 Procedure – Using Igor 4.05A for SFG Data	99

LIST OF TABLES

<u>Table</u>		<u>Page</u>
4.1	Summary of the peak assignments	57

LIST OF FIGURES

Figure	Page
2.1	Graph of the fs and ps fundamental beams to illustrate the difference in FWHM bandwidths 14
2.2	Spectrally dispersed CCD image of the sum frequency generation obtained from temporally and spatially overlapping the fs and ps pulses in a KTP nonlinear crystal..... 17
2.3	The laser setup for the BBSFG experiment . (a) Nd:YVO ₄ laser pumps the (b) Ti:Sapphire oscillator. (c) Nd:YLF laser pumps the (d) ps and (e) fs regenerative amplifiers, which are seeded with (b). (f) An optical parametric amplifier (OPA) is used to convert the fs 800 nm light to mid-infrared light. The infrared light is then directed through (g) a periscope, which rotates the polarization from horizontal to vertical polarized light. The ps 800 nm path includes (h) a delay line for temporal overlap and (i) a pair of waveplates and a Glan-laser polarizer for control of the power and polarization of the ps 800 nm beam. This beam is overlapped on (j) the sample surface with the infrared beam to produce the BBSFG spectra. The resultant BBSFG wavelengths are dispersed using (k) a monochromator and then detected with the (l) CCD array. A (m) HgCdTe detector can be selected to spectrally analyze the infrared beam. 22
2.4	Infrared spectra produced in the OPA and a FTIR spectrum of ambient air for comparison. The fs infrared beam travels through ~ 1 meter of air before detection. Evidence of IR absorption from gas phase water and carbon dioxide in the air is evident in spectra a-d; (a) lowest energy region with the OPA centered at ~ 1650 cm ⁻¹ ; (b) OPA IR is centered at ~2100 cm ⁻¹ ; (c) OPA IR is centered at ~2400 cm ⁻¹ ; and (d) the OPA is tuned to the highest energy region where the OPA IR is centered at ~ 2900 cm ⁻¹ 26
2.5	BBSFG ($P_{SFG}P_{vis}P_{IR}$) from a bare gold surface spectrally dispersed onto the CCD array; 1 second exposure..... 27

2.6	BBSFG spectra ($S_{\text{SFG}}S_{\text{vis}}P_{\text{IR}}$) from the surface of a 1 mM sodium dodecyl sulfate solution; 30, 10, and 5 second exposures are superimposed with the IR spectrum of the OPA output. Inset: 500 ms exposure.....	30
3.1	The surface BBSFG of several ethylene glycol/water solutions. The Raman spectrum of neat ethylene glycol is superimposed with a black line representing the data points	34
3.2	The red data points (\square) are the surface tension versus mole fraction of ethylene glycol, while the blue data points (\circ) are the square root of the surface BBSFG intensity of the CH_2 -SS peaks.....	36
3.3	Ratio of the peak area of the symmetric stretch to the peak area of the asymmetric stretch of the CH_2 peaks from the ethylene glycol in the EG / water solutions at the corresponding ethylene glycol mole fraction.....	39
3.4	(Top graph) The BBSFG spectra of EG / water solution with the BBSFG GaAs spectra collected on 1/23/03. (Bottom graph) The BBSFG of the same EG / water solution and GaAs crystal collected on 1/26/03	40
4.1	Raman (column 1), IR (column 2), surface BBSFG (column 3) spectra of benzene (row a), toluene (row b), m-xylene (row c), and mesitylene (row d). The individual deconvoluted peaks are also shown. Vertical lines are drawn to aid the eye for relative peak positions	48
4.2	The benzene vibrational modes adapted from Varsanyi	49
4.3	The integrated peak areas for the CH_3 -SS (\blacklozenge $2918 \pm 2 \text{ cm}^{-1}$) and CH_3 -AS (\blacksquare $2948 \pm 3 \text{ cm}^{-1}$ and \blacktriangle $2979 \pm 4 \text{ cm}^{-1}$) for toluene (1 CH_3), m-xylene (2 CH_3), and mesitylene (3 CH_3); (a) is the Raman intensity, (b) is the IR intensity, and (c) is the square root of the surface BBSFG intensity	51
4.4	The square root of the BBSFG intensity (solid diamonds) and the square root of the Raman intensity times the square root of the IR intensity (hollow diamonds). The BBSFG intensities are normalized to the Raman-IR intensities using the toluene CH_3 -SS intensity.....	53
4.5	A cartoon representation of a benzene molecule oriented at an air-liquid interface	54
5.1	The Raman spectra of toluene (red) and ethylbenzene (purple).....	62
5.2	The surface $S_{\text{SFG}}S_{\text{vis}}P_{\text{IR}}$ BBSFG spectra of toluene (red) and ethylbenzene (purple)	64

5.3	The surface $S_{\text{SFG}}P_{\text{vis}}S_{\text{IR}}$ BBSFG spectra of toluene (red) and ethylbenzene (purple)	65
5.4	Raman and surface BBSFG spectra of the xylenes. The red data points represent the BBSFG spectra and the blue line represents the Raman spectra. Top graph is o-xylene, middle graph is m-xylene, and the bottom graph is p-xylene	70
6.1	Neat 1-methyl naphthalene Raman spectrum (data points) with a Lorentzian peak profile and the deconvoluted peaks. The $2\delta_s$ represents the overtone of the methyl symmetric bending mode, the ν_s is the methyl symmetric stretch, the ν_a is the methyl asymmetric stretch, 2ν (C=C) is the overtone of the carbon/carbon stretching mode, and ν (=CH) is the aromatic C-H stretching mode	75
6.2	The solid lines in the main figures are the Raman spectra and data points are the surface $S_{\text{SFG}}S_{\text{vis}}P_{\text{IR}}$ BBSFG spectra of a) neat 1-methyl naphthalene and b) hydrated 1-methyl naphthalene. The Lorentzian peak fits for each of the BBSFG spectra are shown as solid lines in the inset. The inset in a) has both the symmetric (ν_s) and the asymmetric stretching (ν_a) peaks expanded 4x for clarity	77
6.3	Proposed stacking of the 1-methyl naphthalene molecules at the surface of a) neat 1-methyl naphthalene and b) hydrated 1-methyl naphthalene. The plane of the surface is perpendicular to the aromatic rings	81
6.4	Surface $S_{\text{SFG}}P_{\text{vis}}S_{\text{IR}}$ BBSFG spectra of a) neat (dry) 1-methyl naphthalene and b) fully hydrated (wet) 1-methyl naphthalene are shown. The only discernable peak is the asymmetric stretching mode of the methyl group and is shown in b)	83
6.5	Surface $S_{\text{SFG}}S_{\text{vis}}P_{\text{IR}}$ BBSFG spectra of a) neat 1-methyl naphthalene, b) partially hydrated 1-methyl naphthalene, and c) fully hydrated 1-methyl naphthalene	85

LIST OF ABBREVIATIONS

1-MN	1-Methyl Naphthalene
AgGaS ₂	Silver gallium sulfide
AS	Asymmetric stretch
BBO	β-barium borate
BBSFG	Broad bandwidth sum frequency generation
CCD	Charged coupled device
EG	Ethylene glycol
EB	Ethylbenzene
fs	femtosecond
OPA	Optical parametric amplifier
ps	picosecond
SDG	Synchronized delay and generator
SFG	Sum frequency generation
SS	Symmetric stretch
SP	SpectraPhysics
β	beta – molecular first hyperpolarizability
χ	chi – bulk susceptibility

CHAPTER 1

INTRODUCTION

Surfaces and buried interfaces have been recognized to play important roles in catalytic processes and more recently have been recognized to play critical roles in the processing of molecules in the atmosphere, including pollutants.¹⁻⁵ Atmospheric aerosol surface chemistry, polar stratospheric cloud surface chemistry, and soil-water interfacial chemistry are examples of environmentally relevant interfaces that are not well understood at the molecular level. In light of the need to understand the molecular-level details of these interfacial systems, advances in the field of surface spectroscopy, in particular, broad bandwidth sum frequency generation (BBSFG) spectroscopy is presented in this dissertation. Scanning SFG spectroscopy has been applied to numerous interfacial systems.

Broad bandwidth sum frequency generation technology is gaining recognition for studying solid-surface structure and chemistry.⁶⁻¹³ However, acquiring BBSFG spectra from liquid surfaces has been more elusive due to the inherently low reflectivity of the nonlinear response from many liquid surfaces. In the Allen lab, we have measured the first BBSFG spectra from liquid surfaces.¹⁴

The structure of molecules at various gas–liquid and solid–liquid interfaces are important to understand since the orientation of the molecules that exist in the surface region of atmospheric aerosols may control the subsequent reaction pathways. Yet, the orientation of many molecules at their air–liquid interfaces has not been directly probed previously. This was mainly due to lack of surface-selective experimental techniques such as surface vibrational sum frequency spectroscopy (e.g. BBSFG).

Ethylene Glycol/Water

Many organic compounds are detected at increasing levels in urban regions. These compounds are initially emitted as un-substituted hydrocarbons, which are typically hydrophobic. As they react in the atmosphere with inorganic species such as nitrates, sulfates, ozone, and other oxidizing agents, these hydrocarbons gain functional groups resulting in a hydrophilic hydrocarbon. Ethylene glycol (EG) is a low molecular weight molecule with functionalities representative of hydrophilic secondary aerosols.¹⁵ Thus, it was selected as an initial compound for the surface studies presented here.

EG is frequently used to de-ice airplanes, airport runways, and as automobile antifreeze.¹⁶⁻¹⁸ During the winter months, a significant increase in the detection of EG is observed in the groundwater near airports.^{17,18}

Benzene and Benzene Derivatives

Aromatic hydrocarbons have been measured in significant concentrations in the atmosphere of urban regions,^{19,20} and in surface and ground water.²¹⁻²³ These compounds are emitted into the environment from many sources,²⁴ including fuel combustion.^{25,26} In the environment, aromatic hydrocarbons exist in the gas, liquid or particle phase or as an adsorbate on existing particles such as sediments or atmospheric aerosols.^{19,20} Many of

these hydrocarbons pose health risks in their emitted form and/or can react to form mutagenic compounds.²⁷⁻²⁹ Therefore, these studies are a first step in a series of planned interfacial experiments investigating the role that benzene and its derivatives have on surface reaction pathways. Orientation of these molecules at a surface is an important factor when considering surface reaction mechanisms.

Benzene, Toluene, m-Xylene, and Mesitylene. In the spectroscopic studies presented here, benzene, toluene, 1,3-dimethylbenzene (m-xylene), and 1,3,5-trimethylbenzene (mesitylene) have been selected to systematically study the structure of these molecules at their respective air–liquid interfaces. These studies are the first sum frequency generation (SFG) spectra to be reported from the air–liquid interfaces of benzene, toluene, m-xylene and mesitylene.³⁰ Raman and infrared spectra collected from these same liquids are used for comparison of the bulk liquid spectra to the surface broadband sum frequency generation spectra. The BBSFG spectra show that sum frequency symmetry forbidden modes for benzene that do in fact arise at its liquid surface. Even though the hyperpolarizability, β , of benzene is zero,^{31,32} we observe a strong sum frequency response from the air–liquid interface of neat benzene arising from resonant CH vibrational transitions. This is intriguing in that it implies that a dipole is induced in benzene in its air–liquid interfacial region. Equally interesting is the comparison of the toluene, m-xylene, and mesitylene surface spectra. Complete cancellation of sum frequency from the methyl symmetric stretching modes due to the symmetry of these vibrations for mesitylene is expected to occur from a simple vector addition model. Yet, this does not happen. Mesitylene, on average, partly experiences a gas-phase environment and the other half of the molecule experiences a more liquid-like

environment. The interfacial region is complex, the molecule can be thought of as having two different environments, one on each end of the aromatic ring.

Toluene and Ethylbenzene. A comparison of the surface BBSFG of toluene and ethylbenzene is also presented in this dissertation. The same substitution pattern causes an expectation for the aromatic CH vibrations to have similar appearances. Yet, the methyl and ethyl constituents will have spectroscopic differences.

Xylenes. The surface BBSFG spectroscopy of o-xylene, m-xylene, and p-xylene will further elucidate the orientation of the aromatic compounds at an air–liquid interface. The intensity of surface BBSFG response from the xylenes is expected to be low. In particular, p-xylene (which has a zero β value^{31,32}) is not expected to have a surface BBSFG response. The observed response from the p-xylene is explained by the same rationale as the surface BBSFG response from benzene that is a dipole is induced in p-xylene at the air–liquid interface.

1-Methyl Naphthalene and the Hydration Effects. Alkyl naphthalenes are common constituents of urban atmospheres. Urban atmospheric measurements of gas phase methyl naphthalenes have indicated that these molecules exist in significant concentrations up to 700 ng/m³.^{33,20} Measurements of particulates using standard collection methods show that 3-ring and larger polycyclic aromatic hydrocarbons (PAHs), with correspondingly lower vapor pressures, are the primary species in PAH-rich particulates^{26,34,35,19} and that alkyl naphthalenes exist primarily in the gas phase due to their relatively higher volatility. However, partitioning of molecules between the gas and the particle phase is dependent upon the compound's vapor pressure, the atmospheric aerosol number density, the sizes of organic aerosols present, as well as the ambient

temperature.^{36,37} Alkyl naphthalenes are difficult to quantify in the particulate phase due to the fact that these semi volatile species can vaporize into the gas phase during and after particulate collection, prior to chemical analysis. Despite this, there are a few observations of naphthalenes and alkyl naphthalenes associated with the particulate phase of atmospheric aerosols. These studies have identified alkyl naphthalenes including 1-methyl naphthalene (1-MN) in aerosols collected from traffic tunnels in Sweden³⁸ and in dustfall samples in Macao, China.³⁹

Polycyclic aromatic hydrocarbons, which include alkyl naphthalenes, are commonly introduced into the environment from a variety of fuel sources,^{26,40,25,41-43} diesel fuel exhaust being a major source.^{40,25,41} The unburned components of the diesel fuel contribute to these exhaust emissions and other aromatic hydrocarbons, which are emitted as partially combusted diesel fuel. 1-MN is a constituent of diesel fuels and its emission is therefore thought to be due to incomplete combustion of the diesel fuel in light and heavy-duty diesel vehicles.²⁵ The tailpipe emissions from gasoline-powered vehicles also include 1-MN.²⁶ Significant concentrations of 1-MN are also found in oceanic regions contaminated by crude oil, for example, the 1989 Exxon Valdez oil spill in the Gulf of Alaska⁴² as well as the 1991 Gulf War oil spill along the Saudi Arabian coast.⁴³

In the atmosphere, 1-MN and other alkyl naphthalenes are precursors to mutagenic nitro-methyl naphthalenes and are therefore of concern for health related reasons.⁴⁴ Recent studies show a correlation between PAH particulates (diameters < 2.5 μm) and chronic respiratory disease, lung cancer and cardiopulmonary disease.⁴⁵⁻⁴⁸

1-MN is a low molecular weight PAH which exists as a liquid at ambient conditions. Its Henry's Law constant and vapor pressure are $45 \text{ Pa}\cdot\text{m}^3/\text{mol}$ for aqueous solutions and $6.7 \times 10^4 \text{ Pa}$ (0.066 Torr at 25°C), respectively.⁴⁴ Gas-phase reactions of 1-MN with NO_2 in the presence of OH or NO_3 radicals have been shown to nitrate the naphthalene ring leading to the formation of mutagenic methyl nitro-naphthalenes (MNN).^{49,50} The atmospheric lifetime of gas phase 1-MN due to reactions with OH radical, NO_3 radical, and O_3 is 2.8 hours, 250 days and greater than 125 days, respectively.^{44,50} Currently, the chemistry at the air-liquid interface of atmospheric organic aerosols is not well understood and may in fact be very different than the corresponding purely gas and liquid phase reaction pathways.^{51,15,52} In the studies presented here, the air-liquid interface of 1-MN and the bulk 1-MN liquid are investigated. The molecular structure of the air-1-MN liquid interface is investigated before and after water hydration. When 1-MN exists in the aerosol phase, orientation of 1-MN at the aerosol surface may play a significant role in determining the subsequent reaction pathways.

BBSFG and Raman spectroscopy are used to investigate the surface and the bulk structure of the liquid surface, respectively. The nonlinear optical surface technique, BBSFG, utilized in these studies is sensitive to the molecular arrangement at an interface. Since the surface-selectivity and the sensitivity to molecular arrangement, specifically surface orientation, is of primary interest in these studies, a brief introduction to the theory of vibrational sum frequency generation (SFG) is given.

Sum Frequency Generation Background. A more in depth account of the sum frequency generation theory is found in the literature.⁵³⁻⁶⁰ As a surface-sensitive spectroscopic technique, SFG has been used to study a variety of surfaces and interfaces relevant to surface science and material science.^{6,7,59,61-65} More recently, SFG has been applied to study solid and liquid surfaces of atmospheric relevance.^{58,66-70}

SFG spectroscopy is a second order nonlinear optical technique where the macroscopic nonlinear susceptibility, $\chi^{(2)}$, is probed. The macroscopic polarization of the medium is described in the electric dipole approximation shown in equation 1.

$$P = \chi^{(1)} \cdot E + \chi^{(2)} : EE + \chi^{(3)} : EEE + \dots \quad (1)$$

Where the E represents an electric field and the respective χ tensors represent the polarizability of the medium. The second-order macroscopic nonlinear susceptibility, $\chi^{(2)}$, is probed in SFG experiments. Within the electric dipole approximation, only environments lacking inversion symmetry will give rise to the SFG response. Therefore, at an interface the asymmetry of the molecular environment needs to be taken into account. The SFG intensity, I_{SFG} , is shown in equation (2a) where the intensity is proportional to the absolute square of the macroscopic nonlinear susceptibility, $\chi^{(2)}$, and the intensity of both the 800 nm, $I(\omega_{800})$,

$$I_{SFG} \propto \left| \chi^{(2)} \right|^2 I(\omega_{IR}) I(\omega_{800}) \quad (2a)$$

$$\left| \chi^{(2)} \right| = \left| \chi_{NR}^{(2)} + \sum_v \chi_v^{(2)} \right| \quad (2b)$$

and the infrared, $I(\omega_{IR})$, beams. The nonlinear susceptibility is described in equation (2b) where it is broken down into a non-resonant term, $\chi_{NR}^{(2)}$, and the sum of the resonant terms, $\chi_v^{(2)}$. The resonant response dominates the nonlinear susceptibility when the frequency of an incident infrared beam, ω_{IR} , is resonant with a vibrational mode, ν , and the intensity of the resultant SFG is enhanced. The resonant macroscopic nonlinear susceptibility, $\chi_v^{(2)}$, is shown in equation (3), where A_ν is the strength of the ν^{th} transition

$$\chi_v^{(2)} \propto \frac{A_\nu}{\omega_\nu - \omega_{IR} - i\Gamma_\nu} \quad (3)$$

moment and the relative phase between two peaks is denoted by the sign of A_ν . The center frequency of the transition moment is represented by ω_ν and the dampening factor, Γ_ν , describes the half-width at the half-maximum (HWHM) of the transition. The amplitude, A_ν , includes both the Raman and the infrared contributions; therefore, the SFG is allowed when the vibrational transition is both Raman and infrared active. To further illustrate this point, the molecular susceptibility, $\beta_{lmn,\nu}$, can be described by equation (4),

$$\beta_{lmn,\nu} = \frac{\langle g | \alpha_{lm} | \nu \rangle \langle \nu | \mu_n | g \rangle}{\omega_{IR} - \omega_\nu + i\Gamma_\nu} \quad (4)$$

where $\langle g | \alpha_{lm} | \nu \rangle$ represents the Raman transition moment and $\langle \nu | \mu_n | g \rangle$ represents the IR transition moment for the molecule. An Euler angle transformation relates the molecular coordinate system (l, m, n) to the laboratory coordinate system (I, J, K) .^{56,71,72} The transformation is shown in equation (5) where $\mu_{IJK:lmn}$ is the Euler angle transformation

$$\beta_{IJK,\nu}^{(2)} = \sum_{lmn} \mu_{IJK:lmn} \beta_{lmn,\nu}^{(2)} \quad (5)$$

between the laboratory-coordinates (l, J, K) and the molecule-coordinates (l, m, n) . The macroscopic susceptibility, $\chi_{lJK,v}$, is calculated from the molecular susceptibility, $\beta_{lJK,v}$, as shown in equation (6), where $\chi_{lJK,v}$ is equal to the number density, N , multiplied by the orientational average of $\beta_{lJK,v}$.

$$\chi_{lJK,v}^{(2)} = N \langle \beta_{lJK,v} \rangle \quad (6)$$

Typically, vibrational SFG experiments are accomplished by combining a narrow bandwidth visible laser pulse with a narrow bandwidth infrared laser pulse. The infrared beam is scanned across the region of interest and the SFG intensity arises when the infrared photons are resonant with an infrared and Raman allowed transition of the molecules at the surface. In the present study, femtosecond broad bandwidth technology is employed. The BBSFG system utilizes a broad bandwidth IR beam ($\sim 600 \text{ cm}^{-1}$ bandwidth, ~ 100 femtosecond pulse duration) rather than a narrow IR bandwidth beam as is used in scanning SFG technologies. Therefore, scanning of the infrared frequency is not necessary. As a result, the vibrational SFG spectrum can be obtained theoretically within one laser pulse leading to shorter acquisition times, larger SFG signals and thus, better signal to noise ratios as compared to scanning SFG spectroscopy instruments. BBSFG spectroscopy was utilized in these experiments.

The BBSFG technology is an emerging experimental technique. In order to perform the experiments presented in the dissertation, significant instrumental advances were necessary and the advances are discussed in Chapter 2.

CHAPTER 2

BUILDING THE LASER SYSTEM

2.1 Broadband Sum Frequency Generation with Two Regenerative Amplifiers:

Temporal Overlap of Femtosecond and Picosecond Light Pulses

Introduction

A novel approach in the development of broad bandwidth sum frequency generation is presented that can improve the analytical capability of sum frequency generation vibrational spectroscopy. The development of a SFG spectroscopy system combining femtosecond (fs) broad bandwidth infrared and picosecond (ps) narrow bandwidth visible coherent light (i.e. BBSFG) has application to the molecular level understanding of time-resolved interfacial processes.⁶ SFG is becoming widely used as an analytical technique to understand a variety of interfaces⁷³⁻⁸¹ since it is surface-selective, provides spectroscopic data, i.e. molecular level information, and it can be utilized in most pressure regimes, e.g. atmospheric pressures to high vacuum.

The initial goal of the Allen lab was to design a BBSFG system that can acquire vibrational spectra of gas-liquid interfaces with sub-millisecond temporal resolution incorporating commercially available laser systems. An investigator encounters many experimental problems in designing such a system for the application of examining low

nonlinear response gas-liquid interfaces. For example, sufficient peak powers (as opposed to average power)⁸² are necessary, but not always obtainable, to acquire an interfacial vibrational spectrum of a low nonlinear response gas-aqueous liquid interface. Scanning SFG instrumental designs lack the ability to acquire a complete spectrum from each sum frequency generated pulse, thereby making it very difficult to monitor surface processes over times less than several minutes. In addition, if the molecules at the interface were reacting on the time scale of the scan, an accurate spectrum would not be obtained. Infrared beam movement from angle tuning of nonlinear crystals during scans causes problems with spatial overlap at the interface, resulting in spectrum reproducibility difficulties. These experimental issues place limits on current scanning SFG experiments.

In the recent past, Van der Ham et al.^{83,13} (IR free electron laser 50 cm⁻¹ bandwidth) and Richter et al.^{6,84} (~ 400 cm⁻¹ IR bandwidth) have shown that BBSFG spectroscopy has potential for acquiring time-resolved studies of interfacial phenomena and thus allowing for more accurate time resolved SFG spectra. Richter et al. used a Ti:Sapphire-based BBSFG laser setup, which is relevant to the work presented here.⁶ Richter et al. obtained the BBSFG spectra from a self-assembled monolayer of octadecanethiol on gold using the Ti:Sapphire-based laser system. The work presented by Richter et al. utilized a broad bandwidth IR pulse mixed with a narrow bandwidth visible pulse that resulted in a high signal-to-noise ratio data acquisition over a 400 cm⁻¹ spectral region. This was accomplished without scanning the IR frequency, thus eliminating the need to move the nonlinear crystals. This prevented the loss of spatial overlap during the

acquisition of the spectral region. This new approach for SFG spectroscopy provided a foundation for a new generation of SFG experimental design.

The BBSFG system currently being designed in this laboratory differs from that of Richter et al. in that it incorporates two regenerative amplifiers (ps and fs). The system designed in this laboratory circumvents the problems associated with scanning SFG instruments (also accomplished by Richter et al.) and the problems associated with insufficient peak powers. The double amplifier design provides increased energies while still maintaining laser mode quality and high contrast ratios (pulse to background intensities). In studies of gas–liquid interfaces of low nonlinear response, it is usually necessary to increase the intensity of the IR and visible beams (i.e. with a constant pulsewidth). Recall equation (1) from SFG theory.^{85,86,54,53}

$$I(\omega_{\text{SFG}}) \propto |\chi^{(2)}|^2 I(\omega_{\text{IR}}) I(\omega_{\text{vis}}) \quad (1).$$

If the second order macroscopic susceptibility, $\chi^{(2)}$, is small (i.e. low nonlinear response) for a given interface (e.g. air-water), the intensity of the incoming beams needs to be increased to compensate for this effect in order to maintain high SFG signal-to-noise ratios.

BBSFG System

The double amplifier design for this BBSFG system is unusual in that the 800 nm pulse produced in the oscillator (Spectra Physics (SP), sub 50 fs Tsunami pumped by 4.7 W from a SP, Millennia Vs) is split with a 50/50 beamsplitter to seed two regenerative amplifiers, one fs (90 fs; Positive Light fs Spitfire) and one ps (1.6 ps; Positive Light, Picomask Spitfire). The system produces $\sim 1\text{mJ}$ for the fs and ps pulses at 1 kHz. The regenerative amplifiers (upgradeable to the higher power versions) were pumped with

20W (8 and 12 W, respectively) from a Nd:YLF (SP, Merlin) Q-switched laser. (In December 2001, the Merlin laser was replaced with a diode pumped Nd:YLF laser.)

To evaluate the fs and ps fundamental beams, a 150 mm focal length monochromator (1200 g/mm grating blazed at 500 nm) attached to a thermoelectrically cooled back-illuminated CCD camera (SpectruMM 256B GS, 256 x 1024 pixels, loaned for this experiment from Roper Scientific) was used. In Figure 2.1, the spectrum of the fs broad bandwidth beam after appropriate attenuation with neutral density filters is shown. The broad bandwidth spectrum covers a range of more than 400 cm^{-1} ($\sim 280 \text{ cm}^{-1}$ FWHM) and is centered near $12,540 \text{ cm}^{-1}$ ($\sim 797 \text{ nm}$). The fs pulse was measured to be 80 fs with a single shot autocorrelator (SP) prior to the spectrum being imaged. The spectrally resolved CCD image of the ps narrow bandwidth fundamental centered at $12,430 \text{ cm}^{-1}$ ($\sim 805 \text{ nm}$) is also shown in Figure 2.1. The bandwidth of the ps beam is much narrower as expected with a 15 cm^{-1} FWHM (by using a ps mask inside the stretcher). Narrowing the bandwidth of the ps pulse is optional depending on the required resolution of the experiment. Since the fs infrared has a broad bandwidth, the SFG spectral resolution must come from the ps narrow bandwidth pulse ($\omega_{\text{IR}} + \omega_{\text{vis}} = \omega_{\text{SFG}}$).

Without using additional synchronization electronics, temporally overlapping the fs and ps laser pulses is experimentally challenging since the two pulses are generated from separate amplifiers. By splitting a single seed source for injection into the amplifiers, this process is simplified without the addition of costly electronics for seed pulse synchronization. In addition, since both amplifiers are pumped by the same Nd:YLF laser, amplifier pulse optimization is straightforward. Yet, making the path lengths equivalent from the seed source to the injection pockel cell is insufficient for

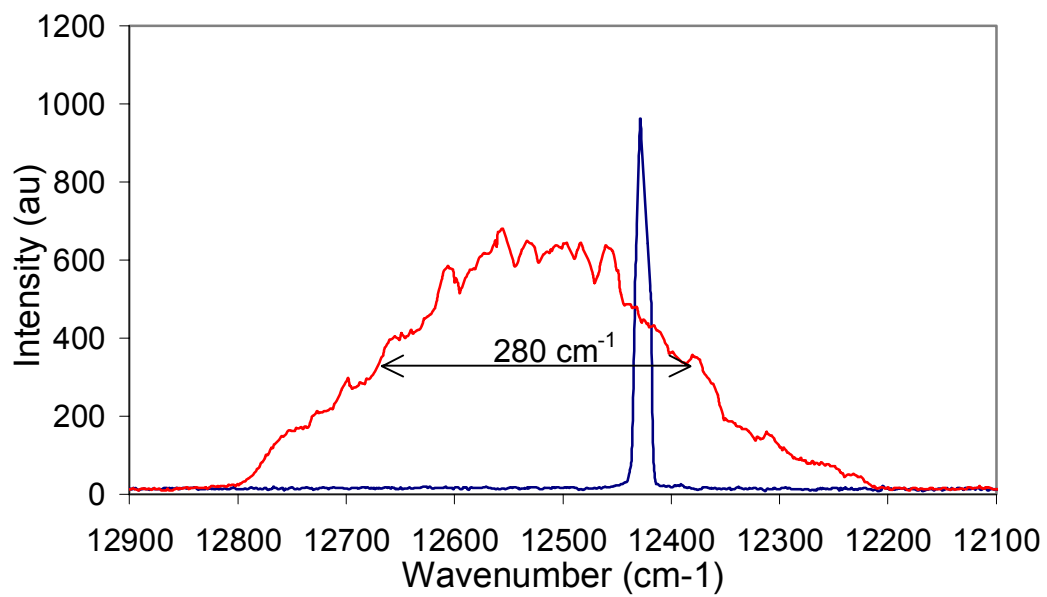


Figure 2.1: Graph of the fs and ps fundamental beams to illustrate the difference in FWHM bandwidths.

temporal overlap to occur at the output of the amplifiers. (There are two pockel cells in each amplifier, one for seed pulse injection, and one for amplified pulse ejection.) The path lengths that the pulses travel in the fs and ps regenerative cavities are different depending on the build-up time (number of round trips) the pulse needs before the “exit” pockel cell ejects the pulse into its respective compressor. (The fs amplifier requires a longer build-up time relative to the ps amplifier.) In addition, if the pockel cell electronics for the fs and ps amplifiers are not temporally calibrated to one another, this process is nontrivial.

To match the pulses in time at a set distance from their respective compressor outputs, 2 fast photodiodes (Bill White, PL private communication) and a 2-channel 350 MHz analog oscilloscope (Tektronix 485) were used. The analog scope was triggered from the output on the synchronized and delay generator (SDG) from the fs amplifier. Jitter in the temporal response from the non-triggered pulse on the scope (appearing as two peaks) was deciphered by testing both options. The ps delay line (retroreflector) was adjusted for temporal overlap of the ps pulse relative to the fs pulse from the photodiode responses on the oscilloscope. Since the Ti:Sapphire oscillator has a repetition rate of 82 MHz, a sub-50 fs pulse is emitted every 12 nanoseconds. Therefore, a seed pulse is available to be injected into the amplifier every 12 ns. The ejection pockel cell timing must be moved in the same temporal direction as the injection timing to allow for proper amplification time. The fast photodiodes were placed the same distance from a KTP crystal with BNC cords of the same length to avoid electronic response-time mismatch. While watching the signal of the fast photodiodes on the oscilloscope, the appropriate seed pulse was chosen for each amplifier, as was the position of the retroreflector until

the peaks were temporally overlapped. The fast photodiodes were then removed and the KTP crystal, which had been placed in the path of the spatially overlapped beams, was used for fine-tuning of the temporal overlap. The position of the retroreflector was adjusted using a micrometer while watching the sum frequency generation signal appear between the fs and ps pulses on a white card. To optimize the angle of the KTP crystal, we previously split one of the amplifier outputs and overlapped the pulses temporally and spatially in the KTP crystal. Then, using the same input angles, but now with the separately generated fs and ps pulses, these laser pulses were spatially and temporally overlapped in the KTP crystal. (Horizontal polarization was maintained for both the fs and ps input beams.) The resulting SFG spectrum centered at $\sim 24,900 \text{ cm}^{-1}$ is shown in Figure 2.2. This SFG bandwidth, observed from the CCD image in Figure 2.2, is consistent with the fs second harmonic generation (SHG) bandwidth, but broader than the ps SHG bandwidth, as one would expect.

The process of building a laser system requires continual update and optimization of the system. It was later discovered that using a single SDG box to trigger both amplifiers completely eliminates the jitter observed. The two seed injection pockel cells need to operate approximately 1 ns relative to each other to assure optimal acceptance of the same pulse. The time difference occurs because of the additional time it takes for the seed pulse to arrive at the second amplifier (fs). The coaxial cable connected to the fs amplifier is approximately 2 feet longer than the cable connected to the ps amplifier. This cable length difference introduces about 1 ns delay between the two injection pockel cells. The pulse ejection pockel cells are triggered from the same SDG box, but the

relative cable lengths need to be optimized to optimize the required buildup time for the pulses in the amplifier.

Conclusions

Broad bandwidth sum frequency generation spectroscopy has tremendous potential as an analytical tool to help understand interfaces at the molecular level in a time-resolved manner. The system described in this paper will be used to obtain SFG data on interfaces that would typically be hard to probe due to insufficient SFG response and low signal-to-noise ratios. We have shown that temporal overlap of independently amplified fs and ps pulses can be completed in a time and cost efficient manner allowing future BBSFG experiments fewer experimental constraints. We have also adjusted for path length compensation to overlap the fs broad bandwidth IR with the ps narrow bandwidth 800 nm. Research presented in the dissertation focuses on using this technique to probe the BBSFG produced at low nonlinear response interfaces of interest.

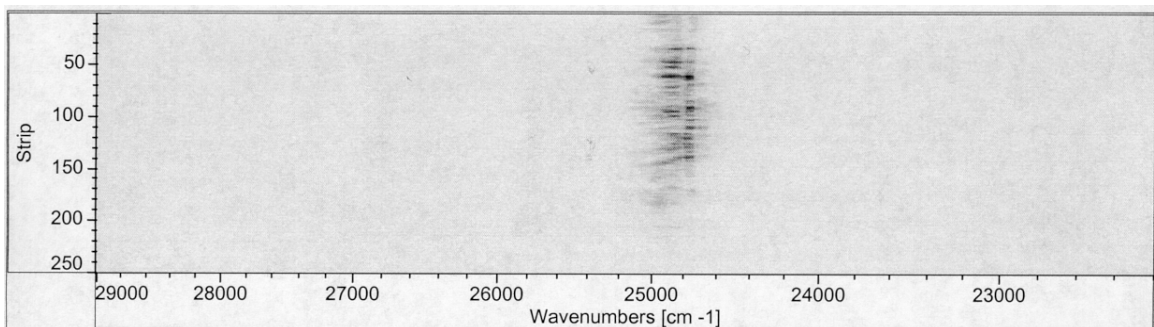


Figure 2.2: Spectrally dispersed CCD image of the sum frequency generation obtained from temporally and spatially overlapping the fs and ps pulses in a KTP nonlinear crystal.

2.2: BBSFG from a Liquid Surface

Introduction

There have been a significant number of surface spectra published using scanning SFG instruments from liquid surfaces; however, until now a BBSFG spectrum from a liquid surface had not been obtained. A new double-amplifier design, which is explained in Part I and in a previously published paper,⁸⁷ was used for the acquisition of these BBSFG spectra. The data presented here show that BBSFG can now be successfully utilized to probe the vibrational modes of molecules at liquid surfaces. We also demonstrate the time-resolved capability of this BBSFG system to acquire data in as little as 500 ms.

Visible-infrared BBSFG spectroscopy provides molecular-level information about species at an interface in the form of polarization-dependent vibrational data from the surface molecules. The strength of BBSFG spectroscopy lies in its inherent ability to attain a full surface spectrum within one pulse of the laser system, thus potentially allowing temporally resolved spectroscopic data from reactions occurring at an interface.

Vibrational sum frequency generation spectroscopy experiments have mainly been performed using scanning SFG instruments with pulse-widths in the ps (picosecond)^{67,88-90,77} or ns (nanosecond)⁹¹⁻⁹⁴ time regime that produce relatively narrow spectral bandwidths. In a scanning SFG system, the nonlinear crystals used to convert a portion of the visible wavelength beam to an infrared beam are angle tuned. The angle tuning causes small directional changes in the beam path, which can affect the spatial overlap of the two incident beams at the sample surface. This can compromise the

spectral reproducibility and the shape of the scanning SFG spectrum. Scanning SFG systems, by the nature of the system, are primarily used on equilibrium or static interfaces. Although scanning sum frequency instruments are still considered state-of-the-art for surface spectroscopic technology, a new generation of broad bandwidth (non-scanning) SFG instruments have taken center-stage because of their ability to capture a full spectrum within one pulse of the laser, thereby providing time-resolved surface data in addition to static or equilibrium surface data.

The system utilized here combines a picosecond (ps) narrow bandwidth 800 nm beam with a femtosecond (fs) broad bandwidth mid-infrared beam on an air-liquid interface. The broad bandwidth infrared beam allows for probing a large spectral region without scanning the infrared frequencies during acquisition of a spectrum. In scanning SFG systems the infrared bandwidth is typically anywhere from 1 cm^{-1} to 25 cm^{-1} depending on the system (nanosecond versus picosecond). In our BBSFG system, the infrared bandwidth is $\sim 600 \text{ cm}^{-1}$ and therefore the resolution in a BBSFG spectrum is derived from resolving the sum frequency response, where $\omega_{800 \text{ nm}} + \omega_{\text{IR}} = \omega_{\text{SFG}}$. Thus, the limit of the BBSFG resolution lies in the narrow bandwidth of the ps 800 nm beam ($\omega_{800 \text{ nm}}$) and the detection system. Since the interface (or surface) is probed with one pulse using BBSFG, integration of BBSFG intensity is only necessary to improve the signal to noise ratio. Therefore, a BBSFG spectrum can be acquired theoretically in 2 ps, which is the pulse-width of the longest pulse. In addition, acquiring real-time data from reactions on the surface are then limited by the laser repetition rate, which is 1 kHz (one pulse every ms) for our BBSFG system.

Experimental

Chemicals. Sodium dodecyl sulfate (SDS) was purchased from Fisher Scientific and used as received. The 1 mM SDS solution was prepared using Nanopure water with a resistivity of 18.3 M Ω ·cm.

Instrumentation. The laser system utilized for the broad bandwidth sum frequency generation (BBSFG) experiments shown in Figure 2.3, consists of two regenerative amplifiers both seeded with a Ti:Sapphire oscillator (Spectra Physics (SP), Tsunami, sub 50 fs, 82 MHz centered at 800 nm, ~ 350 cm $^{-1}$ bandwidth). The Ti:Sapphire oscillator is pumped with 4.7 W from a Nd:YVO $_4$ laser (SP, Millennia Vs) frequency doubled to 532 nm. The regenerative amplifiers are both pumped with a Nd:YLF Q-switched, 1 kHz laser (SP, Super Merlin) frequency doubled to 527 nm (In December 2001, the Nd:YLF was switched out with a diode pumped Nd:YLF laser.). The amplifiers produce horizontally polarized 800 nm light by amplifying the pulses from the Ti:Sapphire oscillator. The femtosecond (fs) regenerative amplifier (Positive Light, fs Spitfire) produces 1 mJ, <90 fs broad bandwidth pulses (~ 300 cm $^{-1}$) at 1 kHz repetition rate. The picosecond (ps) amplifier (Positive Light, Picomask Spitfire) produces 1 mJ, 2 ps narrow bandwidth pulses (~ 15 cm $^{-1}$) also at 1 kHz. The optical parametric amplifier ((OPA) SP, OPA-800CF) is pumped using the amplified femtosecond beam to produce a broad bandwidth infrared beam that is tunable from 3500 cm $^{-1}$ to 1400 cm $^{-1}$. The OPA consists of a sapphire crystal, a double pass beta-barium borate (BBO) crystal, and a silver gallium sulfide (AgGaS $_2$) crystal in addition to polarization, focusing, and reflective optics to convert the 800 nm light to mid-infrared light. The 800 nm beam in the OPA is split into three beams using two beam splitters. The first portion of the beam

(< 5%) produces a white light continuum when focused into the sapphire crystal. The second portion of the 800 nm beam (~15%) is mixed with the white light in the BBO crystal, resulting in the amplification of a region of the spectrum from the white light. The angle of the BBO crystal determines the wavelengths from the white light that are amplified. The near-infrared light produced is further amplified when it is mixed with the remainder of the 800 nm beam in the BBO crystal during a second pass. The amplified near infrared photons then pass through the AgGaS₂ crystal and difference frequency mixing results in mid-infrared photons. Pulsewidths of 85 fs have been measured for the broad bandwidth fs 800 nm beam that is used to produce the infrared. A slight broadening of the infrared pulsewidth is expected to occur since conversion of broad bandwidth 800 nm to infrared requires that the 85 fs beam passes through optics that cause group velocity dispersion. Infrared energy is typically 11 – 12 μJ per pulse in the 3000 cm⁻¹ region and decreases to less than 2 μJ in the 1700 cm⁻¹ region.

A BBSFG spectrum is produced when the broad bandwidth infrared beam is incident (~ 67° from the surface normal) onto a liquid surface and overlapped temporally and spatially with the narrow bandwidth 800 nm beam (~ 58° from the surface normal). The temporal overlap using the double amplifier system has previously been addressed.⁸⁷ The resultant SFG response propagates from the surface of the sample according to momentum conservation requirements (~ 60° from the surface normal). The BBSFG photons are dispersed using a 500 mm focal length monochromator (Acton Research SpectraPro 500i) containing a turret with 3 gratings (1800 grooves/mm holographic, 1200 grooves/mm and 150 grooves/mm) and a movable mirror to select between two separate

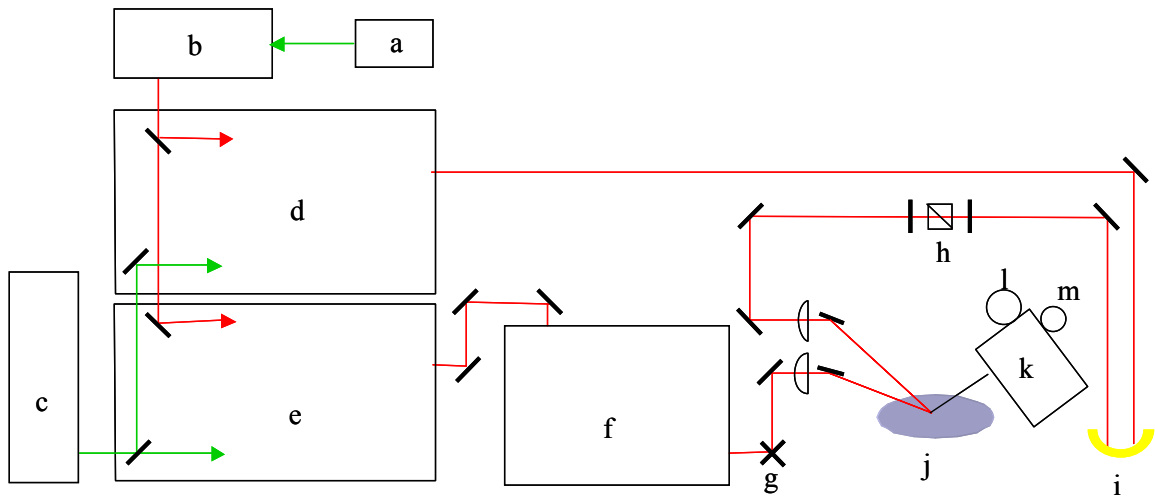


Figure 2.3: The laser setup for the BBSFG experiment. (a) Nd:YVO₄ laser pumps the (b) Ti:Sapphire oscillator. (c) Nd:YLF laser pumps the (d) ps and (e) fs regenerative amplifiers, which are seeded with (b). (f) An optical parametric amplifier (OPA) is used to convert the fs 800 nm light to mid-infrared light. The infrared light is then directed through (g) a periscope, which rotates the polarization from horizontal to vertical polarized light. The ps 800 nm path includes (h) a delay line for temporal overlap and (i) a pair of waveplates and a Glan-laser polarizer for control of the power and polarization of the ps 800 nm beam. This beam is overlapped on (j) the sample surface with the infrared beam to produce the BBSFG spectra. The resultant BBSFG wavelengths are dispersed using (k) a monochromator and then detected with the (l) CCD array. A (m) HgCdTe detector can be selected to spectrally analyze the infrared beam.

exit ports. The BBSFG spectra presented here were dispersed using the 1200 grooves/mm grating blazed at 750 nm and a liquid nitrogen cooled back-illuminated charged coupled device ((CCD) Acton Research, SpectruMM:400B, 1340 × 400 pixels) was used for detection. This detection system allows for collecting the entire spectral region simultaneously. The spectrometer was calibrated using the Hg lines from a fluorescent lamp.

The amplified 800 nm beams (fs and ps) were characterized using the CCD and the 1800 grooves/mm holographic grating. The infrared beam was characterized using a Mercury Cadmium Telluride detector (Infrared Associates, Inc. MCT-12-2.0) at the second exit port of the monochromator and the 150 grooves/mm grating blazed at 4000 nm was used to select the desired wavelength. For the infrared characterization, the 150 grooves/mm grating was stepped at 5 nm increments and the MCT detector response was averaged for 2 seconds using a virtual instrument program written in LabView 6.0i to record the infrared spectral data points. A polystyrene sample was used to verify the calibration of the infrared detection system.

All BBSFG spectra and images are shown plotted as a function of incident infrared wavenumber for ease of interpretation although the BBSFG intensity is detected in the visible wavelength region (sum of the two incident frequencies).

Results and Discussion

Before acquisition of BBSFG spectra, it is important for the infrared beam produced in the OPA (i.e. the fs 800 nm light is converted to infrared light) to be characterized with respect to the energy of each wavelength region. The shape of the intensity versus wavenumber curve has a direct impact on the shape of the resultant sum

frequency spectrum since one of the two incident beams is the infrared beam. Spectral characterization of the infrared beam as described above is shown in Figure 2.4. This graph depicts four infrared spectral regions produced with the OPA. A FTIR spectrum of ambient air is shown for comparison since the OPA is open to the laboratory air (i.e. the IR beam from the OPA propagates through ~ 1 meter of air before detection). Each IR curve is attained by spectrally centering the IR output using the required polarization and BBO and AgGaS₂ crystal angles (i.e. the appropriate phase-matching conditions). The IR spectral intensity shown in curve A extends from $\sim 1900\text{ cm}^{-1}$ to $\sim 1400\text{ cm}^{-1}$ and is attenuated by the vibrational bending mode from gas-phase water molecules in the laboratory air (typically 35% relative humidity) and as a result, the peak center and true bandwidth are difficult to determine. (We are currently setting up to purge our system with dry air.) The IR intensity for a different spectral region is shown in curve B ranges from $\sim 2500\text{ cm}^{-1}$ to $\sim 1700\text{ cm}^{-1}$. The short wavenumber side is attenuated by the vibrational water-bending mode. The high frequency side of curve B shows attenuation of the IR intensity at $\sim 2350\text{ cm}^{-1}$ by the CO₂ stretching mode of the CO₂ molecules in the laboratory air, causing additional distortion of the bandwidth. Curve C, a third IR spectral region, shows a significant CO₂ absorption, has a bandwidth of $\sim 700\text{ cm}^{-1}$, and is centered at $\sim 2400\text{ cm}^{-1}$. The largest average IR intensity (typically 11 μJ) and broadest spectral bandwidth ranging from 3500 cm^{-1} to 2400 cm^{-1} is shown in curve D. The short wavenumber edge of the IR intensity shown in curve D is slightly attenuated by the CO₂ stretch. Curve D shows a bandwidth approaching 1100 cm^{-1} and the peak is centered at $\sim 2900\text{ cm}^{-1}$.

The infrared spectral curves shown in Figure 2.4 demonstrate that the OPA of the BBSFG system has the capability to probe infrared resonances in broad infrared spectral regions when combined with the ps 800 nm beam. Tuning the infrared to another spectral region (curves A-D) is relatively simple. In addition, purging the system will improve the infrared intensity and bandwidth particularly for curves A - C. As stated above, this is currently taking place. Tuning between 1400 cm^{-1} and 1000 cm^{-1} should be obtainable with this system and this IR region is currently being examined. It is important to note that short pulses in the fs time regime provide high peak powers that may improve the nonlinear response from liquid surfaces even though the total stated IR energy is distributed over all of the IR wavelengths being produced in the broad bandwidth. This is a critical point since the SFG response from an interface is proportional to the energies of the incident ps 800 nm and fs infrared beams.

BBSFG spectra were initially obtained from a gold surface since gold surfaces typically give large nonlinear responses and are therefore best suited for capturing and optimizing the SFG signal. The ps 800 nm beam (attenuated to $25\text{ }\mu\text{J}$) and the fs infrared beam ($7.7\text{ }\mu\text{J}$) were overlapped temporally and spatially on the gold surface. The resultant BBSFG intensities that were spectrally dispersed on the CCD array are shown in Figure 2.5. The broad bandwidth sum frequency response was detected with a 1 second exposure to the CCD array. The polarizations used for this experiment were P_{SFG} , P_{vis} , and P_{IR} since this combination is known to have a large response from the gold surface. The P polarized light has its electric field vector parallel to the plane of incidence, and S polarized light has its electric field vector pointing perpendicular to the plane of

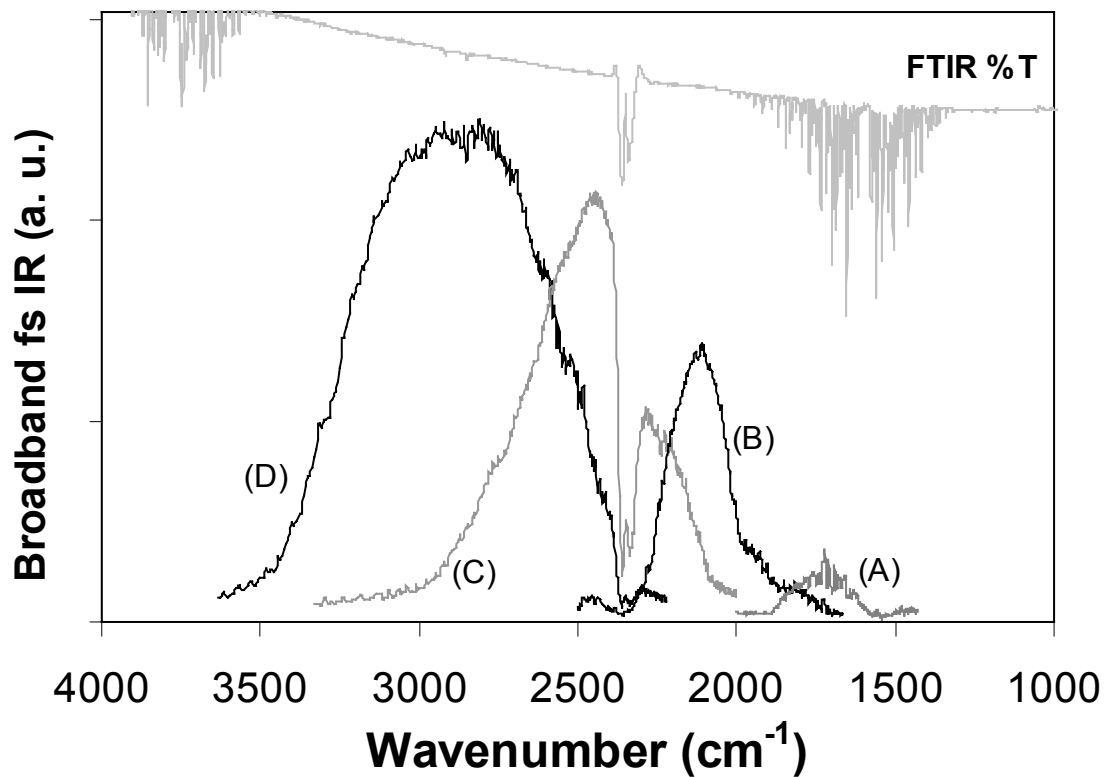


Figure 2.4: Infrared spectra produced in the OPA and a FTIR spectrum of ambient air for comparison. The fs infrared beam travels through ~ 1 meter of air before detection. Evidence of IR absorption from gas phase water and carbon dioxide in the air is evident in spectra a-d; (a) lowest energy region with the OPA centered at $\sim 1650 \text{ cm}^{-1}$; (b) OPA IR is centered at $\sim 2100 \text{ cm}^{-1}$; (c) OPA IR is centered at $\sim 2400 \text{ cm}^{-1}$; and (d) the OPA is tuned to the highest energy region where the OPA IR is centered at $\sim 2900 \text{ cm}^{-1}$.

and that P polarized light is used for both the incident visible (in this case 800 nm) light and the incident infrared light. The $S_{\text{SFG}}S_{\text{vis}}P_{\text{IR}}$ polarization combination from a gold surface produced a significantly lower BBSFG response, as expected from a nonresonant SFG response of a metal surface. Observing the BBSFG intensity on the CCD array during continuous acquisition allowed us to optimize the spatial and temporal overlap on the gold surface. Acquiring the BBSFG spectrum from a gold surface, although not trivial, is the simplest first step before acquiring BBSFG spectra from liquid surfaces.

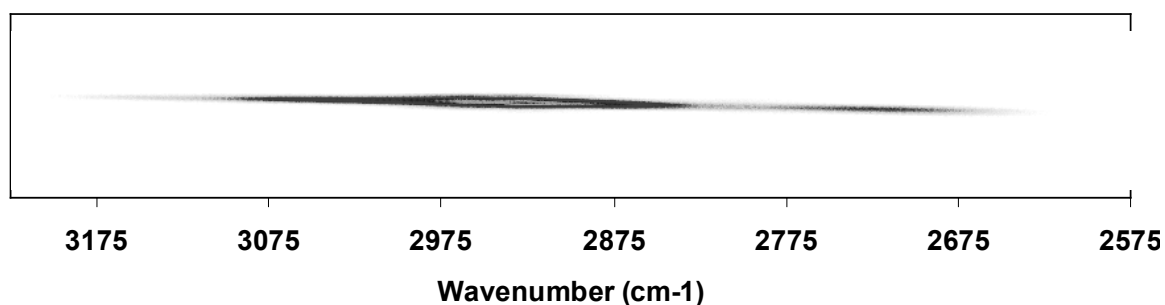


Figure 2.5: BBSFG ($P_{\text{SFG}}P_{\text{vis}}P_{\text{IR}}$) from a bare gold surface spectrally dispersed onto the CCD array; 1 second exposure.

BBSFG spectra from a liquid surface were obtained from a 1mM sodium dodecyl sulfate solution surface using $S_{\text{SFG}}S_{\text{vis}}P_{\text{IR}}$ polarization conditions. The ps 800 nm beam energy was $\sim 240 \mu\text{J}$ and the infrared energy was $\sim 7.7 \mu\text{J}$. The BBSFG spectra were obtained with 500 ms, 5s, 10 s, and 30 s acquisition times. The resultant BBSFG spectra are shown in Figure 2.6 with the infrared spectrum from the OPA superimposed. The

Figure 2.6 inset shows a peak at $\sim 2935\text{ cm}^{-1}$ that is attributed to the CH_3 Fermi resonance. For the exposure times of 5s, 10s, and 30s shown in Figure 2.6, the peaks at 2935 cm^{-1} , 2872 cm^{-1} , and 2844 cm^{-1} are attributed to the CH_3 Fermi resonance, the CH_3 symmetric stretch, and the CH_2 symmetric stretch of SDS at the solution surface, respectively. The peak assignments are consistent with previously assigned vibrational modes of SDS obtained using a scanning SFG system.⁷⁵ Furthermore, a broad peak is observed at $\sim 3100\text{ cm}^{-1}$ and is attributed to the water symmetric stretching vibrational mode from the water molecules at the surface of the SDS solution.

The infrared beam bandwidth is sufficiently broad, as seen in Figure 2.6, to observe the CH stretches from SDS and the lower energy region of the symmetric stretch from the water. All data points in each spectrum were collected simultaneously without tuning of the central infrared frequency. The inset spectrum in Figure 2.6 demonstrates that with this BBSFG system, a spectrum from a liquid surface can be acquired in as short as 500 ms. The acquisition of this spectrum illustrates the potential for obtaining time-resolved data using BBSFG spectroscopy. Obtaining a series of 500 ms BBSFG snapshots of the surface spectroscopy will allow researchers to probe reactions and processes occurring at the surface of liquids. This will help shed light on reaction rates of surface mediated reactions and will provide molecular-level surface structural information. Acquiring vibrational spectra from liquid surfaces has particular relevance to the understanding of surface-processing of atmospheric aerosols and will begin to elucidate the mechanisms that are involved in uptake processes that are currently being studied in other laboratories.^{51,95,96} Signal to noise ratios limit the detection limits in all types of spectroscopy. BBSFG is not different in this respect; however, by increasing the

exposure time, BBSFG signals are improved substantially as shown in Figure 2.6. The signal to noise ratio increases significantly as the acquisition time is increased from 500 ms to 30 s. The spectra shown here reveal that acquisition times on the order of 5 to 10 seconds work well for improving signal to noise ratios for liquid solution surfaces.

Summary

BBSFG technology is designed to acquire a large SFG spectral region in each laser pulse, thereby surpassing the capabilities of scanning SFG systems for the utilization in time domain studies of surfaces. BBSFG, like scanning SFG is inherently surface-specific and in the dipole approximation only gives vibrational data from a surface. The BBSFG spectra presented here illustrate the successful utilization of our double amplifier design to acquire vibrational spectra from a liquid surface. We have demonstrated the ability of this system to acquire liquid-surface spectra in as few as 500 ms. The improved signal to noise ratios for BBSFG spectra at liquid surfaces are enhanced by the utilization of a liquid-nitrogen cooled CCD array, which integrates the BBSFG intensity and therefore limits the background noise. Current work in our laboratory is aimed at decreasing the time of acquiring a BBSFG spectrum to less than 10 ms. Most notable in the work presented here is that vibrational spectra from liquid surfaces have been obtained using broad bandwidth sum frequency generation spectroscopy. This work reveals that BBSFG technology has the potential to play a significant role in understanding the molecular-level details of liquid surface structure and moreover, shedding light on the complex nature of chemical reactions occurring at liquid surfaces.

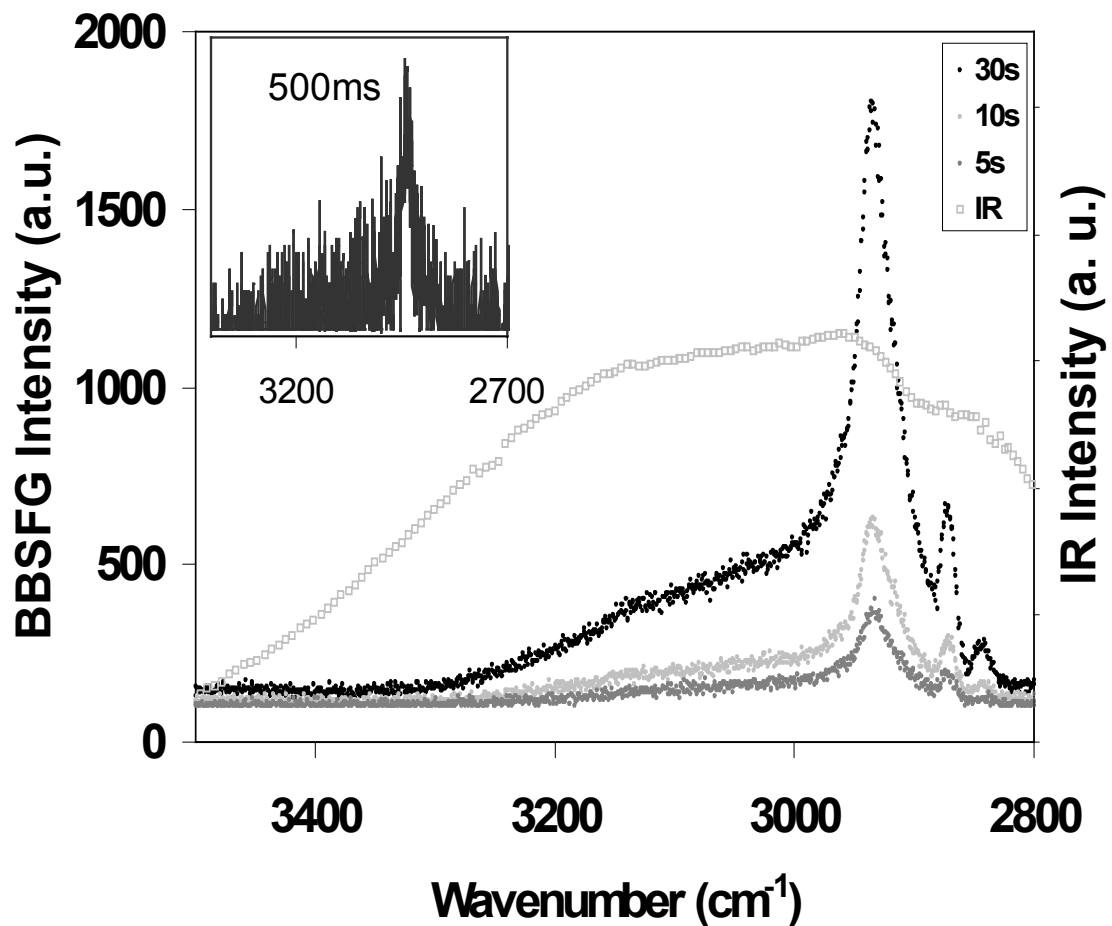
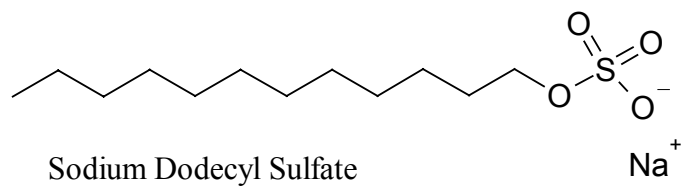


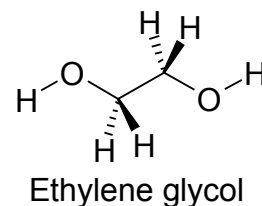
Figure 2.6: BBSFG spectra ($S_{\text{SFG}}S_{\text{vis}}P_{\text{IR}}$) from the surface of a 1 mM sodium dodecyl sulfate solution; 30, 10, and 5 seconds exposures are superimposed with the IR spectrum of the OPA output. Inset: 500 ms exposure.

CHAPTER 3

ETHYLENE GLYCOL—A MODEL HYDROPHILIC AEROSOL

Introduction

Ethylene glycol (EG) is an interesting simple hydrophilic compound for the initial surface BBSFG experiments performed on organic liquids. EG was selected as a model compound for hydrophilic aerosol studies. Due its simplicity, the spectroscopy is not expected to be complicated.



Experimental

Chemicals. Ethylene glycol (EG) was purchased from Aldrich with a purity of 99.8% and used as received. Nanopure water with a resistivity of 18 MΩ·cm was also used. The mole fraction solutions were prepared by mass addition of both components into amber jars. The BBSFG spectra were collected using glass petri dishes cleaned using ammonium persulfate and sulfuric acid and rinsed with copious amounts of nanopure water, and then oven dried.

Instrumentation. The Raman spectra were obtained using 43 mW from a 532 nm continuous wave laser (Spectra-Physics (SP), Millennia II), a 500 mm monochromator (Acton Research, SpectroPro 500i; 1200 g/mm grating blazed at 750 nm), and a liquid

nitrogen cooled CCD camera (Roper Scientific, LN400EB, 1340 x 400 pixel array, back-illuminated, deep depletion CCD). Raman spectra were collected using a fiber optic (Inphotonics, RP 532-05-15-FC), which was coupled to the entrance slit of the monochromator. The slit width was set to 50 μm and the resulting spectral resolution was 4 cm^{-1} . The Raman spectra were acquired with 3-second exposures to the CCD.

The laser system used to obtain the broadband sum frequency generation spectra has been previously described in Chapter 2.^{14,97,30,61,68} However, a brief overview is presented here with regard to the EG experiments performed and to reflect any changes made to the laser system. The laser system used for the BBSFG experiments includes two regenerative amplifiers (SP, Spitfires). The amplifiers are seeded with sub 50 fs, 800 nm pulses from a Ti:Sapphire Oscillator (SP, Tsunami). The amplifiers are pumped using a Nd:YLF (SP, Evolution30) laser operating at a kHz repetition rate. One of the amplifiers produces 85 fs, 800 nm broadband pulses ($\sim 300 \text{ cm}^{-1}$). The resulting pulses then pump an optical parametric amplifier (SP, OPA-800C) to produce a broadband infrared beam ($\sim 600 \text{ cm}^{-1}$, kHz). The second amplifier is equipped with a mask that spectrally narrows the pulse to 17 cm^{-1} ($\sim 2 \text{ ps}$). The infrared beam (P-polarized) energy was 10.8 μJ and the visible beam (S-polarized) energy was 540 μJ for the experiment performed on 1/23/03. The infrared beam energy was 10.0 μJ and the visible beam energy was 550 μJ for the experiments performed on 1/26/03. The infrared and the 800 nm beams were overlapped spatially and temporally on the liquid surface of interest. The resultant sum frequency was dispersed spectrally using a 500 mm monochromator equipped with a 1200 g/mm diffraction grating blazed at 750 nm (Acton Research, SpectroPro 500i) and the dispersed sum frequency light was collected using a liquid nitrogen cooled CCD camera (Roper

Scientific, LN400EB, 1340 x 400 pixel array, back-illuminated CCD). The BBSFG spectra obtained were S-polarized and a Glan laser polarizer was used to verify the resultant BBSFG S-polarization. The spectra were obtained during 30 second acquisitions and 3 spectra were averaged.

Prior to collecting the BBSFG spectra from the samples, a non-resonant BBSFG spectrum from the surface of a GaAs crystal was obtained during each experimental session. The BBSFG spectra, which are then normalized with the GaAs spectrum, show a central region where the peaks are easily discernable above the noise ($\sim 400 \text{ cm}^{-1}$). As one would expect, the edges of these normalized spectra are dominated by noise; thus, only the central region is used for data presentation and interpretation.

The BBSFG spectra were calibrated using a polystyrene thin film and another non-resonant BBSFG spectrum from the same GaAs crystal. The calibration BBSFG spectrum was collected by placing a thin film of polystyrene (infrared absorbencies are well known) in the path of the infrared beam prior to beam overlap on the GaAs crystal. The resultant infrared beam is structured due to absorbance by the polystyrene film, which leads to a structured non-resonant BBSFG spectrum from the GaAs crystal. The peak positions (dips) in the calibration GaAs BBSFG spectrum are used to calibrate the BBSFG spectra obtained during the same experimental session.

Results and Discussion

The surface broad bandwidth sum frequency generation spectra of the ethylene glycol (EG) and water solutions are shown in Figure 3.1 with the Raman spectrum of neat ethylene glycol superimposed. The BBSFG spectra shown are normalized using the non-resonant BBSFG spectrum of a GaAs crystal. The EG solution with a 0.04 mole fraction

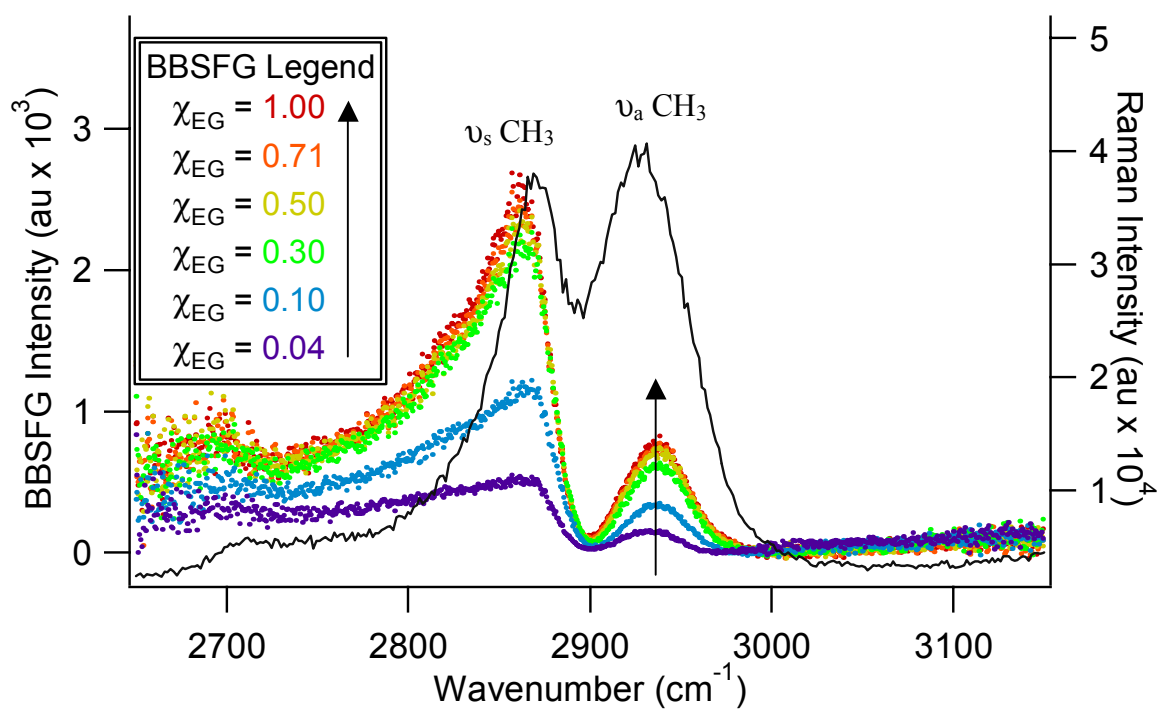


Figure 3.1: The surface BBSFG of several ethylene glycol/water solutions. The Raman spectrum of neat ethylene glycol is superimposed with a black line representing the data points.

has the lowest BBSFG response is shown with purple data points while the neat EG has the strongest SFG is shown with red data points. The relative intensity of the peaks increases with increasing EG concentration; this observation is further discussed in Figure 3.2. The peak below 2900 cm^{-1} is attributed to the CH_2 -symmetric stretching (SS) mode and the peak around 2940 cm^{-1} is assigned to the CH_2 -asymmetric stretching (AS) mode in both the Raman and the BBSFG spectra. The intensities of these two peaks in the Raman spectra are nearly the same while the peak due to the CH_2 -AS is significantly smaller than the peak due to the CH_2 -SS in the BBSFG spectra for all of the solutions evaluated.

The transition moment of the CH_2 -SS is aligned in the plane containing both hydrogen atoms and the carbon atom, bisecting the angle defined by these atoms. The transition moment of the CH_2 -AS is perpendicular to transition moment of the CH_2 -SS. The number density of the molecules being detected affect the strength of the peak observed in a BBSFG spectrum in addition to the orientation of the molecules at the interface being probed. The orientational effects arise since BBSFG is a coherent spectroscopic technique and linearly polarized laser beams are used. The BBSFG spectra presented here are collected using P-polarized infrared light. The P-polarized light contains the electric field vector perpendicular to the interface and only the transition modes tilted from the surface plane can efficiently interact with the IR light. The peak due to the CH_2 -SS mode is significantly larger than predicted when considering the infrared and Raman transition moments. Therefore, the molecules must be arranged such that the CH_2 groups are on average tilted from the surface plane.

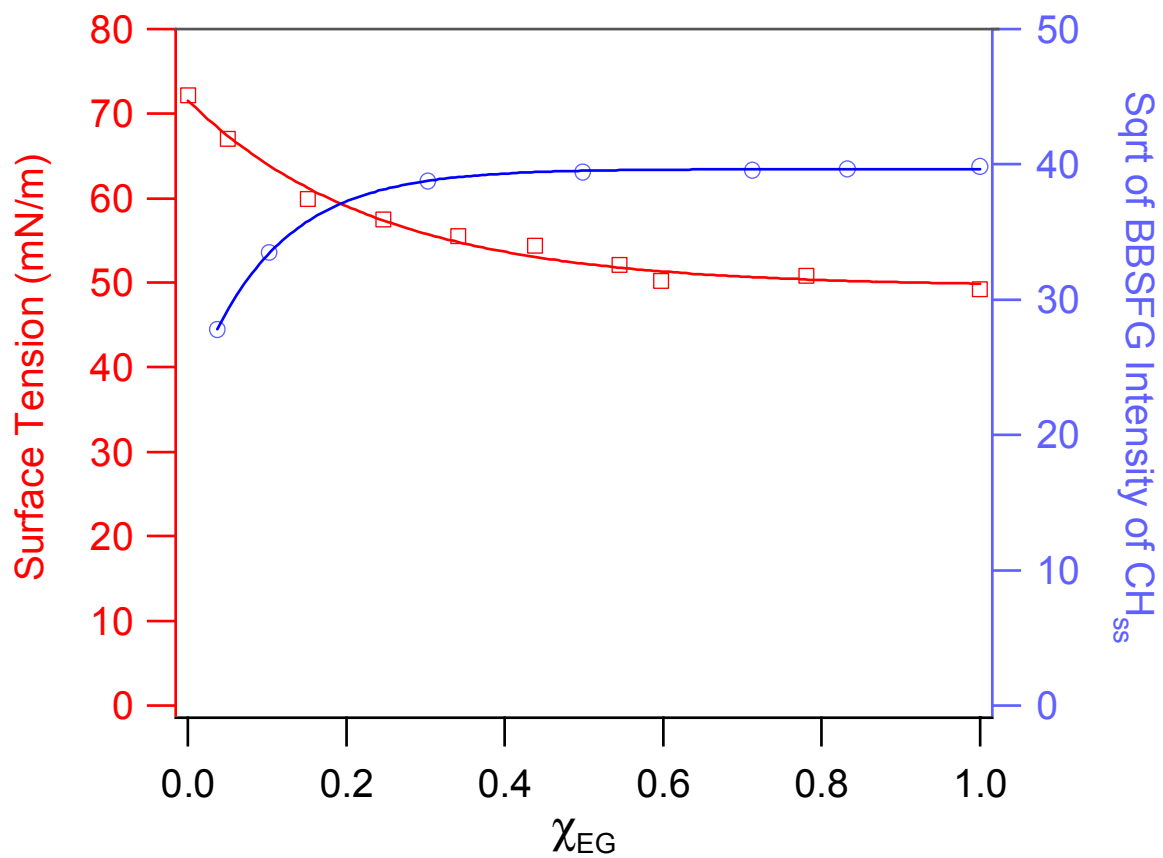


Figure 3.2: The red data points (\square) are the surface tension versus mole fraction of ethylene glycol, while the blue data points (\circ) are the square root of the surface BBSFG intensity of the CH_2 -SS peaks.

The square root of the intensity of the peak assigned to the CH₂-SS is plotted in Figure 3.2 versus the mole fraction of its corresponding EG solution. Additionally, the surface tension of the ethylene glycol / water solutions is plotted in Figure 3.2 versus the mole fraction of the corresponding solution. In the low EG concentration region, the BBSFG intensity increases. The surface tension decreases from the surface tension of water ($ST_{H_2O} = 72.2 \text{ mN/m}$) through the same region. The intensity of BBSFG response for the CH₂-SS appears to level off around 0.3 mole fraction, while the surface tension is continuing to decrease through the entire concentration range.

The constantly changing surface tension for the EG / water solution suggests that as the concentration of the bulk solution increases, more EG molecules exist at the surface. Since the surface BBSFG intensity does not continue to increase with additional molecules at the interface, then the orientation of the molecules is influencing the SFG response. This suggests that the molecules have a larger distribution of orientations at the interface or the EG molecules lie more often in the surface plane in the higher EG concentration regime.

The ratio of the CH₂-SS BBSFG peak area and the CH₂-AS BBSFG peak area is plotted in Figure 3.3 versus the mole fraction of the corresponding EG solution. The comparison of data collected on two different days shows some ambiguity. On one experimental day (1/23/03) the ratio is increasing with concentration in the lower concentration regime while on a different experimental day (1/26/03) the ratio is decreasing in the same concentration range. The increasing ratio was collected on a day (1/23/03) where the frequency of the IR beam was centered on the CH₂ peaks and

normalization does not dramatically affect the relative peaks intensities. While the day with the points (1/26/03) decreasing, the frequency of the IR beam was shifted toward the water region and the CH₂-SS was not detected as efficiently. Figure 3.4 further illustrates this point, where the raw BBSFG spectra of an EG / water solution is plotted with the BBSFG spectra of the GaAs crystal collected on the same day superimposed. This result is indicative of necessary optimization of the normalization process performed on the SFG spectra collected. The results from 1/23/03 are more likely to reflect the surface structure, because the system was optimized for the region being considered.

The results from the optimal day (1/23/03) show that the ratio of the CH₂-SS to CH₂-AS is greatest for the 0.30 mole fraction solution. The ratio describes the average distribution of the molecules at the interface. The increase in the SS versus the AS occurs when the molecules are on average distributed with the CH₂ relatively close to perpendicular to the surface plane.

Summary

In the high EG concentration region, the surface BBSFG spectra of EG / water solutions determine that the EG molecules on average lie with a smaller angle relative to the surface plane or become disordered as the molecules pack tighter at the surface. It is likely that the molecules become disordered with increasing concentration, since more EG molecules are packing into the interfacial region. There appears to be a critical concentration (0.03 M. F.) where the EG molecules are oriented with their methylene groups on average close to perpendicular to the surface plane and the OH groups are buried into the liquid side of the interface.

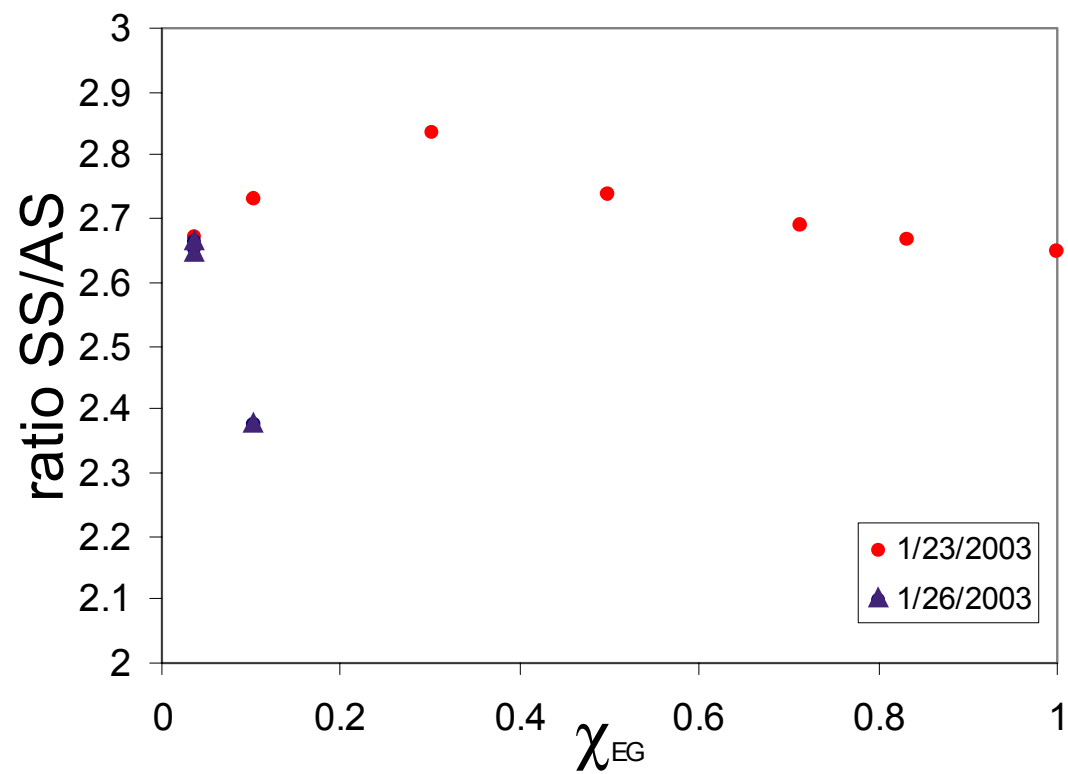


Figure 3.3: Ratio of the peak area of the symmetric stretch to the peak area of the asymmetric stretch of the CH₂ peaks from ethylene glycol in the EG / water solutions at the corresponding ethylene glycol mole fraction.

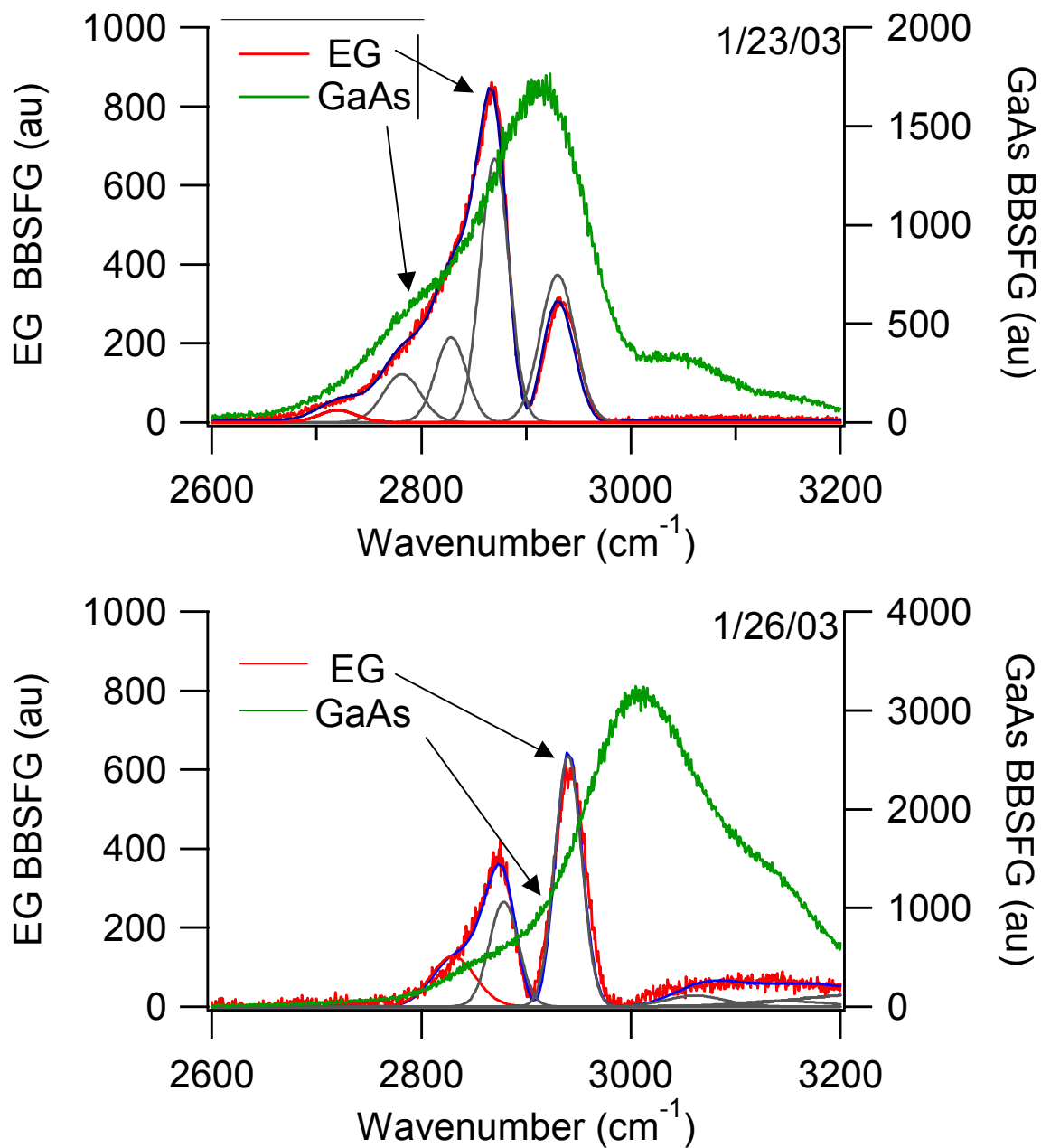


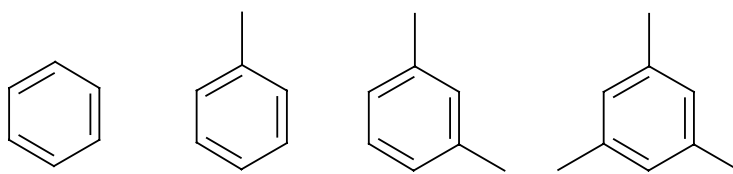
Figure 3.4: (Top graph) The BBSFG spectra of EG / water solution with the BBSFG GaAs spectra collected on 1/23/03. (Bottom graph) The BBSFG of the same EG / water solution and GaAs crystal collected on 1/26/03.

CHAPTER 4

BENZENE, TOLUENE, m-XYLENE, AND MESITYLENE: A SERIES OF METHYL SUBSTITUTED BENZENES.

Introduction

The first group of aromatic compounds investigated using sum frequency generation spectroscopy is presented in this chapter. The ability to detect a surface non-linear response from benzene is a stimulating result. The aromatic compounds are interesting from an atmospheric perspective since they are pervasive in urban regions and benzene is a known carcinogen. The ability to study the surface structure may lead to a better understanding of aromatic compounds on aerosols in the atmosphere.



Benzene

Toluene

m-Xylene

Mesitylene

Experimental

Chemicals. Benzene (99.9+%), toluene (99.8%), m-xylene (99+%), and mesitylene (98%) were obtained from Aldrich and used as received. Pyrex petri dishes, used for sample containment for SFG analysis, were cleaned with ammonium-persulfate

and rinsed with copious amounts of nanopure water with a resistivity of 18 m Ω ·cm, then dried in an oven.

Instrumentation. The Raman spectra were obtained using 88 mW from a 532 nm continuous wave laser (Spectra-Physics (SP), Millennia II), a 500 mm monochromator (Acton Research, SpectroPro 500i; 1200 g/mm grating blazed at 750 nm), and a liquid nitrogen cooled CCD camera (Roper Scientific, LN400EB, 1340 x 400 pixel array, back-illuminated, and deep depletion CCD). Raman spectra were collected using a fiber optic (Inphotonics, RP 532-05-15-FC), which was coupled to the entrance slit of the monochromator. The slit width was set to 10 μ m and the resulting spectral resolution was 0.4 cm^{-1} . The Raman spectra were acquired with 1-second exposures to the CCD and 5 spectra were averaged.

The Infrared spectra were collected using a Fourier transform infrared spectrometer (Perkin Elmer, 16 PC FT-IR) with a spectral resolution of 4 cm^{-1} . A drop of each liquid was placed between two NaCl plates and 16 scans were collected and averaged. The spectral absorbances of the IR spectra collected were scaled to the infrared spectra from the NIST Chemistry WebBook (available online).

The laser system used to obtain the broadband sum frequency generation spectra has been previously described.^{14,97,30,61,68} However, a brief overview is presented here. The laser system used for the BBSFG experiments includes two regenerative amplifiers (SP, Spitfires). The amplifiers are seeded with sub 50 fs, 800 nm pulses from a Ti:Sapphire Oscillator (SP, Tsunami). The amplifiers are pumped using a Nd:YLF (SP, Evolution30) laser operating at a kHz repetition rate. One of the amplifiers produces 85 fs, 800 nm broadband pulses ($\sim 300 \text{ cm}^{-1}$). The resulting pulses then pump an optical

parametric amplifier (SP, OPA-800C) to produce a broadband infrared beam ($\sim 600 \text{ cm}^{-1}$, kHz). The second amplifier is equipped with a mask that spectrally narrows the pulse to 17 cm^{-1} ($\sim 2 \text{ ps}$). To further narrow the pulse spectrally, an additional mask was added to the compressor within this regenerative amplifier resulting in $\sim 5 \text{ cm}^{-1}$ spectral-width pulses.⁶⁸ The infrared beam (P-polarized) energy was $11.3 \mu\text{J}$ and the visible beam (S-polarized) energy was $150 \mu\text{J}$ for this experiment. The infrared and the 800 nm beams were overlapped spatially and temporally on the liquid surface of interest. The resultant sum frequency was dispersed spectrally using a 500 mm monochromator equipped with a 1200 g/mm diffraction grating blazed at 750 nm (Acton Research, SpectroPro 500i) and the dispersed sum frequency light was collected using a liquid nitrogen cooled CCD camera (Roper Scientific, LN400EB, 1340 x 400 pixel array, back-illuminated CCD). The BBSFG spectra obtained were S-polarized and a Glan laser polarizer was used to verify the resultant BBSFG S-polarization. The spectra were obtained during 5-minute acquisitions.

Prior to collecting the BBSFG spectra from the samples, a non-resonant BBSFG spectrum from the surface of a GaAs crystal was obtained during each experimental session. The BBSFG spectra, which are then normalized with the GaAs spectrum, show a central region where the peaks are easily discernable above the noise ($\sim 400 \text{ cm}^{-1}$). As one would expect, the edges of these normalized spectra are dominated by noise; thus, only the central region is used for data presentation and interpretation.

The BBSFG spectra were calibrated using a polystyrene thin film and another non-resonant BBSFG spectrum from the same GaAs crystal. The calibration BBSFG spectrum was collected by placing a thin film of polystyrene (infrared absorbencies are

well known) in the path of the infrared beam prior to beam overlap on the GaAs crystal. The resultant infrared beam is structured due to absorbance by the polystyrene film, which leads to a structured non-resonant BBSFG spectrum from the GaAs crystal. The peak positions (dips) in the calibration GaAs BBSFG spectrum are used to calibrate the BBSFG spectra obtained during the same experimental session.

Results and Discussion

The Raman, IR, and $S_{\text{SFG}}S_{\text{vis}}P_{\text{IR}}$ -polarized broad bandwidth sum frequency generation (BBSFG) spectra of benzene, toluene, m-xylene, and mesitylene from 2700 cm^{-1} to 3150 cm^{-1} are shown in Figure 4.1. Peak assignments were based upon symmetry arguments and assignments from Green⁹⁸ and assignments compiled by Varsanyi.⁹⁹ Also shown in Figure 4.1 are the component peaks calculated using a Voigt profile (See Appendix A) for each spectrum. The assignments to the peaks shown in the spectra of Figure 4.1, including possible combination and overtone modes, are listed in Table 4.1. The focus of this chapter is on the methyl group stretching modes and the aromatic CH stretching modes. Vertical lines are shown in Figure 4.1 passing through the peaks assigned to the methyl symmetric stretching ($\text{CH}_3\text{-SS}$) peaks and the CH stretch region of the Raman, IR, and surface BBSFG spectra for each compound for reference.

The Raman, IR, and surface BBSFG spectra of liquid benzene are shown in the Figures 4.1a1, 4.1a2, and 4.1a3, respectively. The aromatic CH stretching modes (peaks above 3000 cm^{-1}) observed in these spectra are illustrated in Figure 4.2 and correspond to benzene vibrational modes from Varsanyi.⁹⁹ To be able to compare relative intensities within each spectroscopic technique, the scale for each type of spectrum is kept constant. Therefore, we have plotted the full scale Raman spectrum from benzene in the inset of

Figure 4.1a1. In some cases, different aromatic CH modes are observed in each type of spectroscopy, as one would expect from symmetry of the vibrational modes. In the surface BBSFG spectrum from benzene, the peak observed at 3056 cm^{-1} is assigned to the degenerate ν_{20a} and ν_{20b} CH vibrational modes, which are shown in Figure 4.2.

The significant surface BBSFG response from the neat benzene–air interface as shown in Figure 4.1a3 was not an anticipated result since the first hyperpolarizability, β , of benzene is zero.^{31,32} A reasonable explanation is that the benzene molecules at the surface experience a different environment on the air-side versus the liquid-side of the interface. Therefore, distortions in the electron density of the benzene may explain the observation of a peak due to a symmetry forbidden mode in our BBSFG spectrum.

The P-polarized IR used in this experiment efficiently probes only the transition moments that have components perpendicular to the surface plane. Thus, detection of the CH modes requires that the benzene molecules are on average perpendicular to the surface plane. Maximizing entropy at the surface drives the molecules to stack against one another with benzene rings perpendicular to the surface plane. EFISH (electric field induced second harmonic generation) measurements of neat benzene show that upon application of a DC field to the liquid, a second harmonic signal is detected, probing the second hyperpolarizability, γ .³¹ However, in our experiments an electric field is not applied, yet the induced dipole established in the interfacial region combined with asymmetry with respect to the inversion center in the ν_{20a} and ν_{20b} vibrational modes gives rise to the SFG response.

The CH stretching mode frequencies in the BBSFG spectrum from benzene (Figure 4.1a3) shift to lower frequencies as compared to the IR spectra (Figure 4.1a2).

Since sum frequency is probing the air–liquid benzene interface, a change in frequencies is not surprising.

The Raman, IR, and surface BBSFG spectra of liquid toluene are shown in the Figures 4.1b1, 4.1b2, and 4.1b3, respectively. The peaks observed at 2921 cm^{-1} , 2919 cm^{-1} , and 2915 cm^{-1} in the Raman, IR and surface BBSFG spectra of toluene, are assigned to the methyl symmetric stretch ($\text{CH}_3\text{-SS}$) mode, respectively. The peaks observed at 2944 cm^{-1} and 2983 cm^{-1} in the toluene Raman spectrum, 2950 cm^{-1} and 2983 cm^{-1} in the toluene IR spectrum, and 2945 cm^{-1} and 2980 cm^{-1} in the toluene BBSFG spectrum are attributed to the methyl asymmetric stretching ($\text{CH}_3\text{-AS}$) modes. The CH stretching modes, listed in Table 4.1 for toluene, show that the surface BBSFG is only observed from the ν_{20a} and ν_2 vibrations for the CH stretching modes of the aromatic ring. However, a significant frequency shift is observed from the BBSFG benzene CH assignments, as one would expect. In addition, the aromatic CH stretching mode frequencies in the BBSFG spectrum from toluene shift to lower frequencies as compared to the Raman and IR spectra. The calculated peaks using a Voigt profile (See Appendix A) of the toluene BBSFG spectrum determined that the two $\text{CH}_3\text{-AS}$ transitions were 180° out of phase with the $\text{CH}_3\text{-SS}$, and all of the aromatic CH transitions were in phase with the $\text{CH}_3\text{-AS}$.

The Raman, IR, and surface BBSFG spectra of liquid m-xylene (1,3-dimethylbenzene) are shown in the Figures 4.1c1, 4.1c2, and 4.1c3, respectively. The peaks observed at 2920 cm^{-1} , 2919 cm^{-1} , and 2917 cm^{-1} in the Raman, IR, and BBSFG spectra of m-xylene, respectively, are attributed to the $\text{CH}_3\text{-SS}$. Additionally, the peaks observed at 2953 cm^{-1} and 2975 cm^{-1} in the Raman spectrum, 2949 cm^{-1} and 2976 cm^{-1} in

the IR spectrum, and 2948 cm^{-1} and 2985 cm^{-1} in the BBSFG spectrum are assigned to the $\text{CH}_3\text{-AS}$ modes. The aromatic CH stretching modes, listed in Table 4.1 for m-xylene, show that the surface BBSFG is observed from the ν_2 and ν_{20b} aromatic ring vibrational structure shown in Figure 4.2, and that for Raman, IR, and the surface BBSFG, the ν_{7a} mode is no longer relevant and the ν_{7b} structure is below the experimental range.⁹⁹ The ν_2 and ν_{20b} assignments are based on symmetry of the vibrational mode and assignments from Green.⁹⁸ However, we have not completely ruled out the ν_{20a} assignment for this peak. The calculated peaks using a Voigt profile (See Appendix A) of the m-xylene BBSFG spectrum determined that the two $\text{CH}_3\text{-AS}$ transitions were 180° out of phase with the $\text{CH}_3\text{-SS}$ and all of the aromatic CH transitions were in phase with the $\text{CH}_3\text{-AS}$.

The Raman, IR, and surface BBSFG spectra of liquid mesitylene (1,3,5-trimethylbenzene) are shown in the Figures 4.1d1, 4.1d2, and 4.1d3, respectively. The peaks observed at 2919 cm^{-1} , 2916 cm^{-1} , and 2917 cm^{-1} in the mesitylene Raman, IR, and BBSFG spectra, respectively, are assigned to the $\text{CH}_3\text{-SS}$. The peaks observed at 2952 cm^{-1} and 2979 cm^{-1} in the Raman spectrum, 2947 cm^{-1} and 2972 cm^{-1} in the IR spectrum, and 2946 cm^{-1} and 2973 cm^{-1} (barely visible in Figure 4.1d3) in the surface BBSFG spectrum are attributed to the $\text{CH}_3\text{-AS}$ modes. The CH stretching modes, listed in Table 4.1 for mesitylene, show that the surface BBSFG is observed from the ν_{20a} and ν_{20b} aromatic ring vibrational structure shown in Figure 4.2. For the Raman, IR, and the BBSFG, the ν_{7a} and ν_{7b} modes are below the experimental range.⁹⁹ The calculated peaks using a Voigt profile (See Appendix A) of the mesitylene BBSFG spectrum determined that the two $\text{CH}_3\text{-AS}$ transitions were 180° out of phase with the $\text{CH}_3\text{-SS}$ and all of the aromatic CH transitions were in phase with the $\text{CH}_3\text{-AS}$.

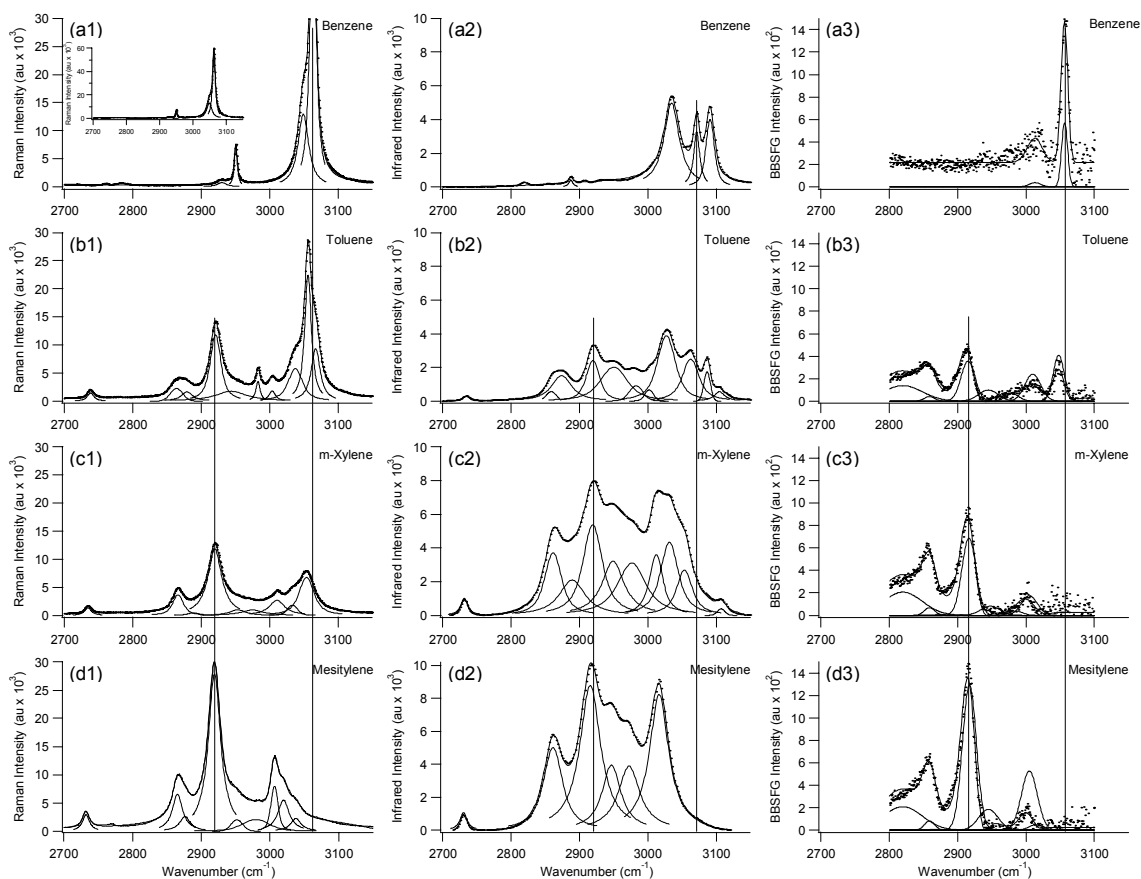


Figure 4.1: Raman (column 1), IR (column 2), surface BBSFG (column 3) spectra of benzene (row a), toluene (row b), m-xylene (row c), and mesitylene (row d). The individual deconvoluted peaks are also shown. Vertical lines are drawn to aid the eye for relative peak positions.

The Raman and IR spectra of toluene, m-xylene, and mesitylene are expected to have peaks in the spectral region above 3000 cm^{-1} due to the aromatic CH stretching modes. The peaks observed below 3000 cm^{-1} are mainly assigned to methyl group vibrational modes as discussed above. Although, the aromatic CH spectral region for toluene, shown in Figures 4.1b1 and 4.1b2 resemble that of benzene, the aromatic CH spectral region has shifted slightly to lower frequencies. The aromatic CH stretches for m-xylene and the mesitylene are further shifted to lower frequencies in the Raman and IR spectra; the highest frequency for an aromatic CH stretch in the mesitylene spectra is 40 cm^{-1} less than the lowest frequency aromatic CH stretch observed from benzene. A previous computational investigation of benzene and several substituted benzenes led to the determination that the preferred orientation of the methyl group has one CH bond eclipsing the benzene ring of toluene, m-xylene and mesitylene.¹⁰⁰ The interaction of the eclipsing methyl hydrogen will lower the energy of the aromatic CH stretching frequencies and this is consistent with our experimental observations.

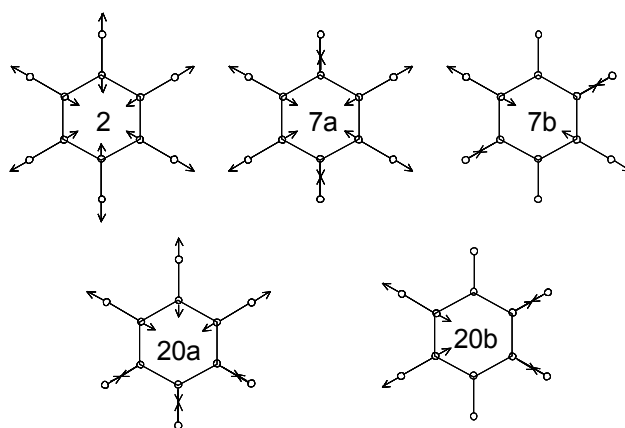
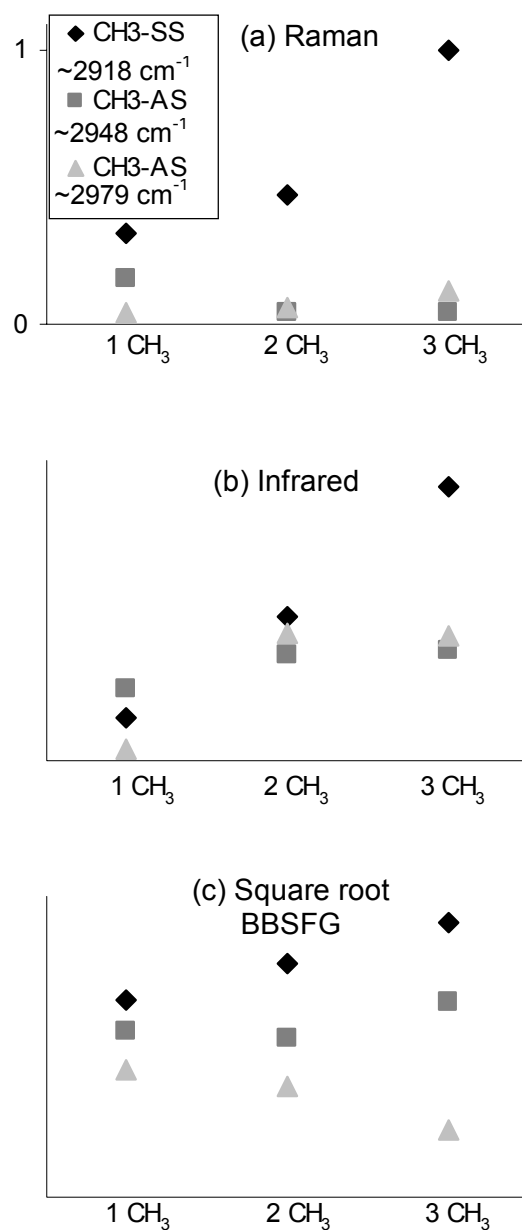


Figure 4.2: The benzene vibrational modes adapted from Varsanyi.⁹⁹

The BBSFG spectra are expected to have characteristics from both the Raman and the IR spectra, since the transition moment is a combination of the Raman and IR transition moments. However, the BBSFG spectrum of mesitylene is expected to have small intensities, since β is nearly zero.³² Nonetheless, the surface BBSFG spectrum of mesitylene is well resolved with a relatively large SFG response. The surface BBSFG spectrum of mesitylene detected at the air–liquid interface is due to an interfacial induced dipole, similar to the interfacial effects on benzene. The resulting surface BBSFG spectra of toluene, m-xylene and mesitylene do contain spectral characteristics analogous to their respective Raman and IR spectra.

The observed positions for the peaks assigned to the CH₃-SS in the Raman, IR, and BBSFG spectra for toluene, m-xylene, and mesitylene all occur within 6 cm⁻¹ of each other; the vertical line drawn in Figure 4.1 through the CH₃-SS peaks further illustrates the minimal differences in the spectra. However, significant differences are observed in the methyl peak integrated areas for the spectra shown in Figure 4.1. To further illustrate how the methyl peak areas vary as a function of the number of methyl group moieties, the Raman, IR, and BBSFG methyl peak areas are plotted in Figure 4.3. The relative areas for the Raman, IR, and BBSFG spectral peaks assigned to the CH₃-SS (diamonds) and the individual peaks assigned to the two CH₃-AS (squares and triangles) versus the number of methyl groups contained in the molecule are shown in Figure 4.3, where 4.3a is the Raman data, 4.3b is the IR data, and 4.3c is the square root of the BBSFG data. The relative peak areas of the CH₃-SS in the toluene (1 CH₃ moiety) spectra have the lowest integrated peak area for all three of the spectroscopic techniques utilized. The integrated peak areas for the CH₃-SS in the m-xylene (2 CH₃) spectra are larger than that of toluene,



I. **Figure 4.3:** The integrated peak areas for the CH₃-SS (\blacklozenge $2918 \pm 2 \text{ cm}^{-1}$) and CH₃-AS (\blacksquare $2948 \pm 3 \text{ cm}^{-1}$ and \blacktriangle $2979 \pm 4 \text{ cm}^{-1}$) for toluene (1 CH₃), m-xylene (2 CH₃), and mesitylene (3 CH₃); (a) is the Raman intensity, (b) is the IR intensity, and (c) is the square root of the surface BBSFG intensity.

yet the CH₃-SS in the mesitylene (3 CH₃) spectra has the largest integrated peak areas. This result is not surprising since the response from all three spectroscopic techniques is proportional to the number density of the moieties being evaluated. However, the peak areas of the CH₃-AS do not scale with the increasing number of methyl groups as one might expect, in particular the Raman and BBSFG spectra of toluene, m-xylene, and mesitylene do not follow any apparent trends. The transition moment of the Raman asymmetric stretching mode is relatively weak; therefore, any changes in the peak intensity are difficult to differentiate.

The surface SFG response for a vibrational mode is proportional to the Raman transition moment multiplied by the IR transition moment and convoluted with molecular orientation at the surface. In Figure 4.4, the square root of the CH₃-SS Raman peak area multiplied by the square root of the corresponding IR peak area is plotted. The square roots of the CH₃-SS peak areas of the BBSFG peaks are also shown in Figure 4.4. The slope of the line through the peak areas for the surface BBSFG CH₃-SS (solid diamonds) is substantially smaller than the slope of the line through the Raman CH₃-SS multiplied by the IR CH₃-SS (hollow diamonds) as observed in Figure 4.4. The smaller slope due to the BBSFG CH₃-SS is attributed to surface orientation and intramolecular cancellation of the stretching modes.

The SFG response from the CH₃-SS for all three of the methyl-substituted benzenes strongly indicates that the molecules are aligned with the benzene rings on average tilted from the surface plane, as shown in Figure 4.5. The transition moment for the CH₃-SS is aligned along the central axis of the methyl group and is contained within

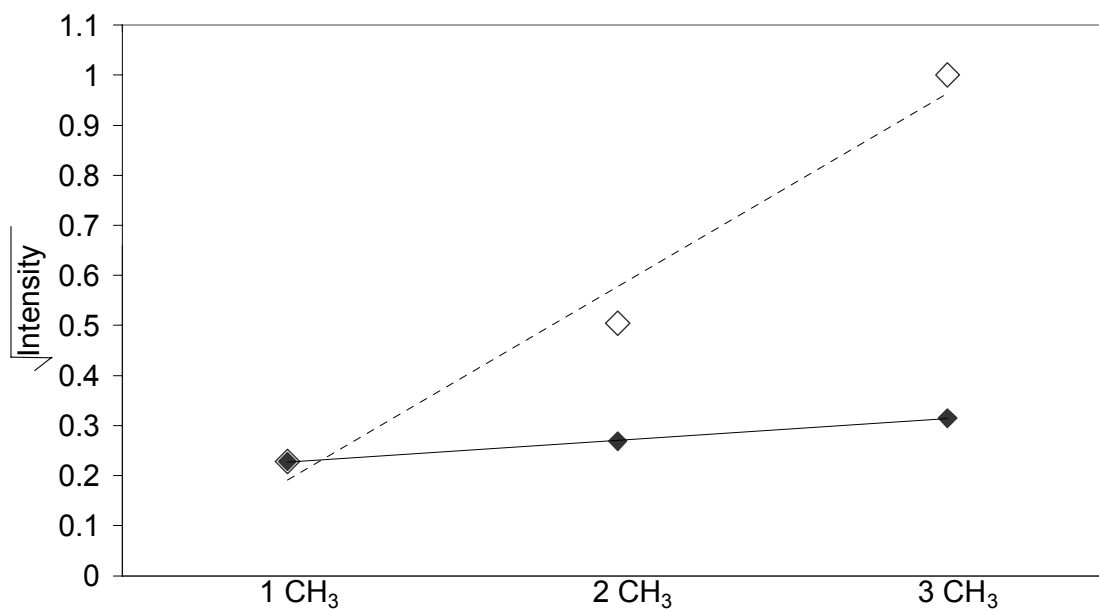


Figure 4.4: The square root of the BBSFG intensity (solid diamonds) and the square root of the Raman intensity times the square root of the IR intensity (hollow diamonds). The BBSFG intensities are normalized to the Raman-IR intensities using the toluene CH₃-SS intensity.

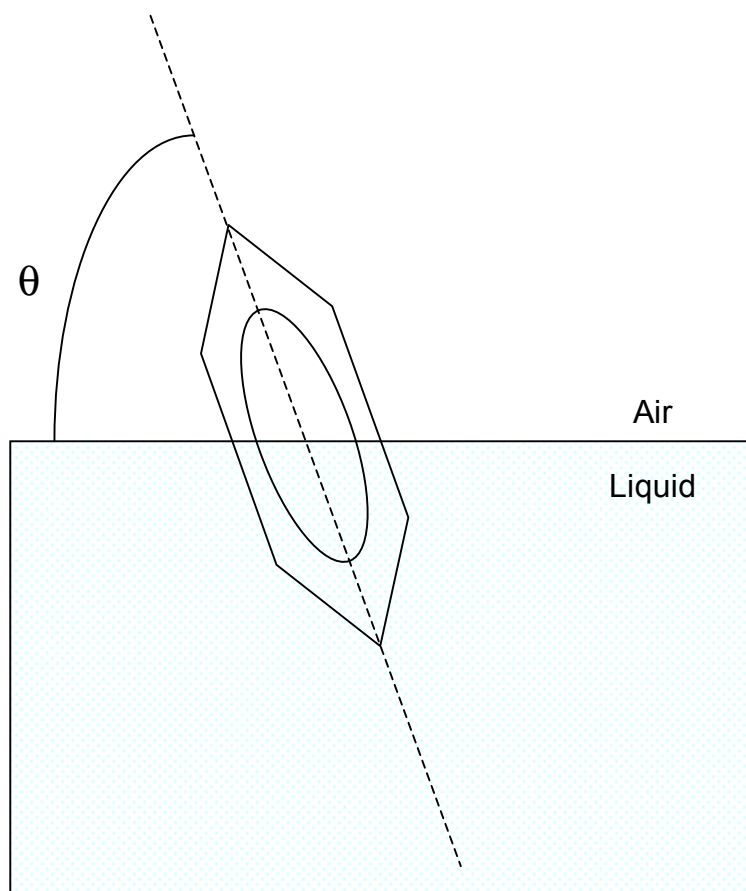


Figure 4.5: A cartoon representation of a benzene molecule oriented at an air–liquid interface.

the plane of the benzene ring. Therefore, the ring must be tilted from the surface plane for interactions between the P-polarized IR and the CH₃-SS to occur. Furthermore, the peak position of the CH₃ stretching modes observed in the surface BBSFG spectra are nearly the same frequency or red-shifted as compared to the liquid IR and Raman stretching frequencies of the same transition as shown in Table 4.1. Previous measurements have indicated that the gas phase peaks are blue shifted as compared to the liquid phase frequencies for these compounds.¹⁰¹ Considering the surface BBSFG peak positions, one could conclude that the methyl groups experience a more liquid-like environment; therefore, in the toluene and m-xylene interfacial regions the methyl groups are oriented on average toward the liquid. The mesitylene however cannot orient all of its methyl groups on the same side of the interface. Yet, on average two of the mesitylene methyl groups may exist on the liquid side.

The symmetry of mesitylene implies that the sum frequency response from the CH₃-SS transition moments may cancel each other out. However, at the interface the transitions due to the CH₃-SS exposed to the air environment arise at a different frequency as compared to the transitions due to the CH₃-SS exposed to the liquid environment. The different frequencies infer a change in the character of the transition of each stretching mode; therefore, the SFG response from the liquid-side CH₃-SS mode cannot efficiently cancel the SFG response from the air-side CH₃-SS mode.

Conclusions

In summary, we have studied a select group of methyl-substituted benzenes: benzene, toluene, m-xylene, and mesitylene. The Raman and IR results are consistent with previously published accounts of these compounds in the investigated region of

2700 cm^{-1} to 3150 cm^{-1} . The predicted SFG response is zero and near zero for benzene and mesitylene molecules, yet we observe large SFG intensities in their respective surface BBSFG spectra. This result indicates that the interfacial region is capable of inducing a dipole in polarizable systems, such as benzene. The detection of both the aromatic CH stretching modes and the CH_3 -SS modes determines that the molecules must on average be tilted relative to the surface plane, as shown in Figure 4.5. The detected frequencies for the CH_3 -SS are liquid-like thus indicating that the methyl portions of the molecules favor the liquid-side of the interface. Furthermore, the lack of cancellation of the CH_3 -SS from mesitylene suggests that the effect of air on the stretching mode differs from that of the liquid.

	Benzene (D _{6h})			Toluene (C _{2v})			m-Xylene (C _{2v})			Mesitylene (D _{3h})		
	Raman	IR	BBSFG	Lit	Raman	IR	BBSFG	Lit	Raman	IR	BBSFG	Lit
Comb/Overtone	—	—	—	—	2738	2734	—	—	2732	2730	—	—
Comb/Overtone	—	—	—	—	2864	2859	2859	—	2865	2861	2859	—
Comb/Overtone	—	—	—	—	2879	2874	—	—	2876	—	2875	—
ν_s (CH ₃)	—	—	—	—	2921	2919	2915	2921*	2920	2919	2917	2923*
ν_a (CH ₃)	—	—	—	—	2944	2950	2945	2952*	2953	2949	2948	2953*
ν_a (CH ₃)	—	—	—	—	2983	2983	2980	2979*	2975	2976	2985	2970*
Comb/Overtone	2950	2887	—	—	—	—	—	—	3011	3012	3005	—
ν (=CH) 7a	3049	—	—	3056*	3004	3002	3010	3003*	—	—	—	935*
ν (=CH) 7b	3049	—	—	3056*	3037	—	—	3039*	—	—	—	935*
ν (=CH) 20a	—	3071	3056	3064*	3067	3063	3048	3063*	3033	3031	—	3032 [†]
ν (=CH) 20b	—	3071	3056	3064*	—	3027	—	3029*	3054	3054	3045	3052 [†]
ν (=CH) 2	3063	—	—	3073*	3056	—	—	3055*	3054	3054	3045	3052 [†]
Comb/Overtone	—	3034	3013	—	—	3087	—	—	—	—	—	—
Comb/Overtone	—	3091	—	—	—	3105	—	—	—	—	—	—
												3107

Table 4.1: Summary of the peak assignments.

*Varsanyi⁹⁹

[†]Green⁹⁸

CHAPTER 5

BBSFG OF BENZENE DERIVATIVES AT THEIR RESPECTIVE AIR– LIQUID INTERFACES

Introduction

The investigation of the aromatic compounds using sum frequency generation spectroscopy is continued in this chapter. In order to interpret the surface BBSFG spectra of the aromatic compounds, these molecules were grouped according to molecular similarities. The first group, toluene and ethylbenzene which is presented in Part I of this chapter, is a comparison between two mono substituted benzenes. The second group, dimethyl substituted benzenes, is presented in Part II of this chapter.

Experimental

Chemicals. Toluene (99.8%), Ethylbenzene (99.8%), o-xylene (98%), m-xylene (99+%), and p-xylene (99+%) were obtained from Aldrich and used as received. Pyrex petri dishes, used for sample containment for SFG analysis, were cleaned with ammonium-persulfate and rinsed with copious amounts of nanopure water with a resistivity of $18 \text{ M } \Omega \cdot \text{cm}$, then dried in an oven.

Instrumentation. The Raman spectra were obtained using 110 mW from a 532 nm continuous wave laser (Spectra-Physics (SP), Millennia II), a 500 mm

monochromator (Acton Research, SpectroPro 500i; 1200 g/mm grating blazed at 750 nm), and a liquid nitrogen cooled CCD camera (Roper Scientific, LN400EB, 1340 x 400 pixel array, back-illuminated, deep depletion CCD). Raman spectra were collected using a fiber optic (Inphotonics, RP 532-05-15-FC), which was coupled to the entrance slit of the monochromator. The slit width was set to 50 μm and the resulting spectral resolution was 4 cm^{-1} . The Raman spectra were acquired with 5-second exposures to the CCD.

The laser system used to obtain the broadband sum frequency generation spectra has been previously described and in Chapter 2.^{14,97,30,61,68} However, a brief overview is presented here to show the details specific for the benzene derivatives presented in this chapter. The laser system used for the BBSFG experiments includes two regenerative amplifiers (SP, Spitfires). The amplifiers are seeded with sub 50 fs, 800 nm pulses from a Ti:Sapphire Oscillator (SP, Tsunami). The amplifiers are pumped using a Nd:YLF (SP, Evolution30) laser operating at a kHz repetition rate. One of the amplifiers produces 85 fs, 800 nm broadband pulses ($\sim 300 \text{ cm}^{-1}$). The resulting pulses then pump an optical parametric amplifier (SP, OPA-800C) to produce a broadband infrared beam ($\sim 600 \text{ cm}^{-1}$, kHz). The second amplifier is equipped with a mask that spectrally narrows the pulse to 17 cm^{-1} ($\sim 2 \text{ ps}$). To further narrow the pulse spectrally, an additional mask was added to the compressor within this regenerative amplifier resulting in $\sim 5 \text{ cm}^{-1}$ spectral-width pulses.⁶⁸ The infrared beam energy was 11.3 μJ and the visible beam energy was 150 μJ for this experiment. The infrared and the 800 nm beams were overlapped spatially and temporally on the liquid surface of interest. The resultant sum frequency was dispersed spectrally using a 500 mm monochromator equipped with a 1200 g/mm diffraction grating blazed at 750 nm (Acton Research, SpectroPro 500i) and the dispersed sum

frequency light was collected using a liquid nitrogen cooled CCD camera (Roper Scientific, LN400EB, 1340 x 400 pixel array, back-illuminated CCD). A Glan laser polarizer was used to verify the resultant BBSFG polarization. The spectra were obtained during 5-minute acquisitions.

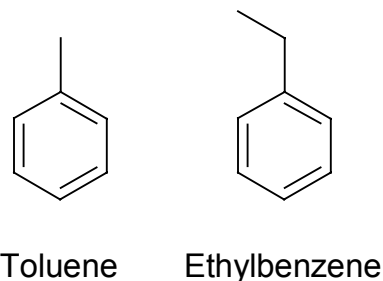
Prior to collecting the BBSFG spectra from the samples, a non-resonant BBSFG spectrum from the surface of a GaAs crystal was obtained during each experimental session. The BBSFG spectra, which are then normalized with the GaAs spectrum, show a central region where the peaks are easily discernable above the noise ($\sim 400 \text{ cm}^{-1}$). As one would expect, the edges of these normalized spectra are dominated by noise; thus, only the central region is used for data presentation and interpretation.

The BBSFG spectra were calibrated using a polystyrene thin film and another non-resonant BBSFG spectrum from the same GaAs crystal. The calibration BBSFG spectrum was collected by placing a thin film of polystyrene (infrared absorbencies are well known) in the path of the infrared beam prior to beam overlap on the GaAs crystal. The resultant infrared beam is structured due to absorbance by the polystyrene film, which leads to a structured non-resonant BBSFG spectrum from the GaAs crystal. The peak positions (dips) in the calibration GaAs BBSFG spectrum are used to calibrate the BBSFG spectra obtained during the same experimental session.

5.1: Toluene and Ethyl Benzene

Results and Discussion

The Raman spectra of toluene and ethylbenzene (EB) are shown in Figure 5.1 from 2700 cm^{-1} to 3100 cm^{-1} . The Raman spectrum of EB is shown with a purple line and the Raman spectrum of toluene is shown with a red line. The EB spectrum is more complex than the toluene Raman spectrum as expected with the addition



of a methylene group. In the EB Raman spectrum, the peak assigned to the CH_2 -symmetric stretching (SS) mode is observed around 2865 cm^{-1} , the peak assigned to the CH_2 -asymmetric stretching (AS) is observed around 2940 cm^{-1} , the peak assigned to the CH_3 -SS is observed around 2900 cm^{-1} , and the peak assigned to the CH_3 -AS mode is observed around 2972 cm^{-1} . These peak assignments are preliminary based on the peak positions reported by Varsanyi.⁹⁹ There appears to be some discrepancies. For example, the CH_2 -AS for EB is significantly stronger than expected compared to the other peak intensities. This suggests that there may be other modes contributing to the peak.

Additional spectroscopic experiments are necessary to verify the peak assignments.

Recall from Chapter 4, that the toluene peak assigned to the CH_3 -SS mode is observed at 2921 cm^{-1} , a peak due to the CH_3 -AS mode is observed as a shoulder on the CH_3 -SS peak at 2944 cm^{-1} , and the other peak assigned to the CH_3 -AS mode is observed at 2983 cm^{-1} .^{99,30} The peaks above 3000 cm^{-1} are assigned to the aromatic CH stretching modes for both the EB and toluene Raman spectra. The two spectra show similarities in this region as expected, since both compounds are mono alkyl substituted benzenes.

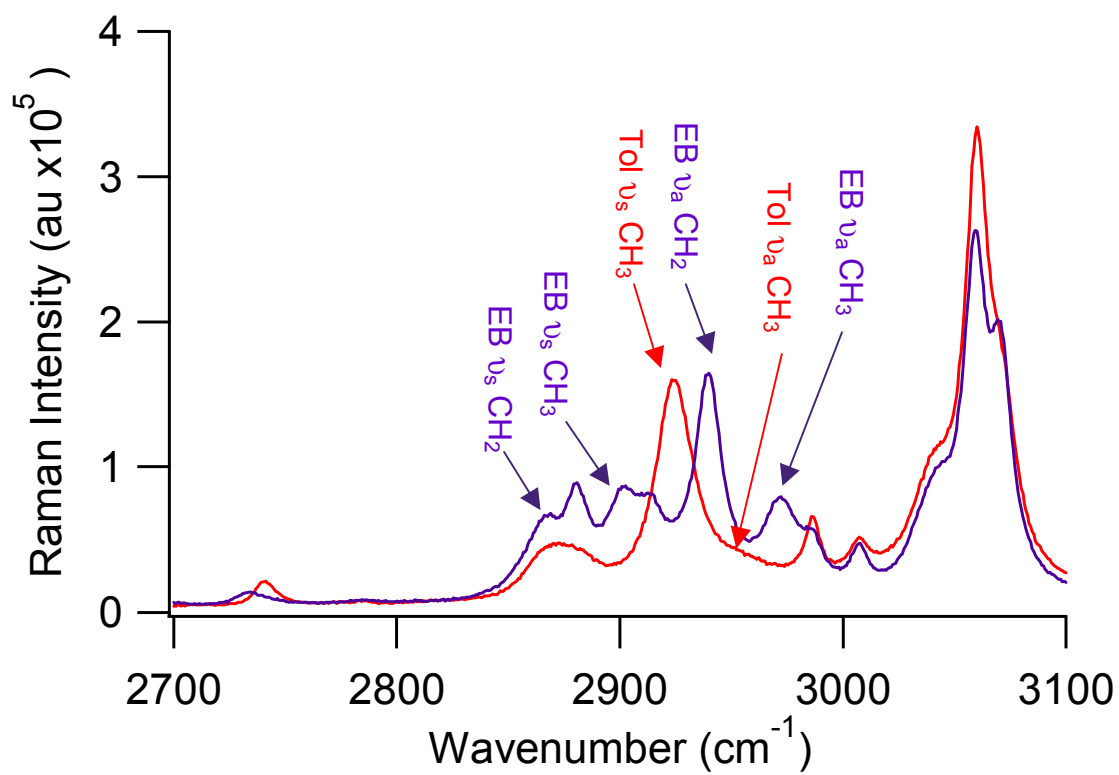


Figure 5.1: The Raman spectra of toluene (red) and ethylbenzene (purple).

The $S_{\text{SFG}}S_{\text{vis}}P_{\text{IR}}$ polarized BBSFG spectra of toluene and EB are shown in Figure 5.2. The toluene BBSFG spectrum is shown with red data points and the EB BBSFG spectrum is shown with purple data points. The EB BBSFG spectrum contains several peaks in the aliphatic CH region. The positions of the peaks observed in the surface BBSFG spectrum of EB correlate with the positions of the peaks observed in the Raman EB spectrum. The peaks in the aromatic region are less resolved. The toluene surface BBSFG spectrum contains two well-resolved peaks in the aliphatic region and the aromatic region is indistinguishable from the EB aromatic BBSFG spectrum.

The similarities between the EB and toluene BBSFG spectra in the aromatic region indicates that the benzene rings for both compounds are oriented on average in the same arrangement in both liquid interfacial regions. Recall from Chapter 4, that the benzene ring for the toluene molecule is aligned tilted from the surface plane,³⁰ thus the benzene ring contained in the EB molecules is also likely to be tilted from the surface plane as opposed to lying flat in the plane of the surface. The relatively strong peaks associated with the CH_2 and CH_3 vibrations further support that the EB molecule is tilted relative to the surface plane.

The $S_{\text{SFG}}P_{\text{vis}}S_{\text{IR}}$ polarized BBSFG spectra of toluene and EB are shown in Figure 5.3. The toluene $S_{\text{SFG}}P_{\text{vis}}S_{\text{IR}}$ BBSFG spectrum does not contain any peaks discernable above the noise, however the EB $S_{\text{SFG}}P_{\text{vis}}S_{\text{IR}}$ BBSFG spectrum contains a strong peak around 2960 cm^{-1} , which is preliminarily assigned to the CH_3 -AS stretching mode. This assignment is based upon the preliminary peaks assignments in the EB Raman spectrum.

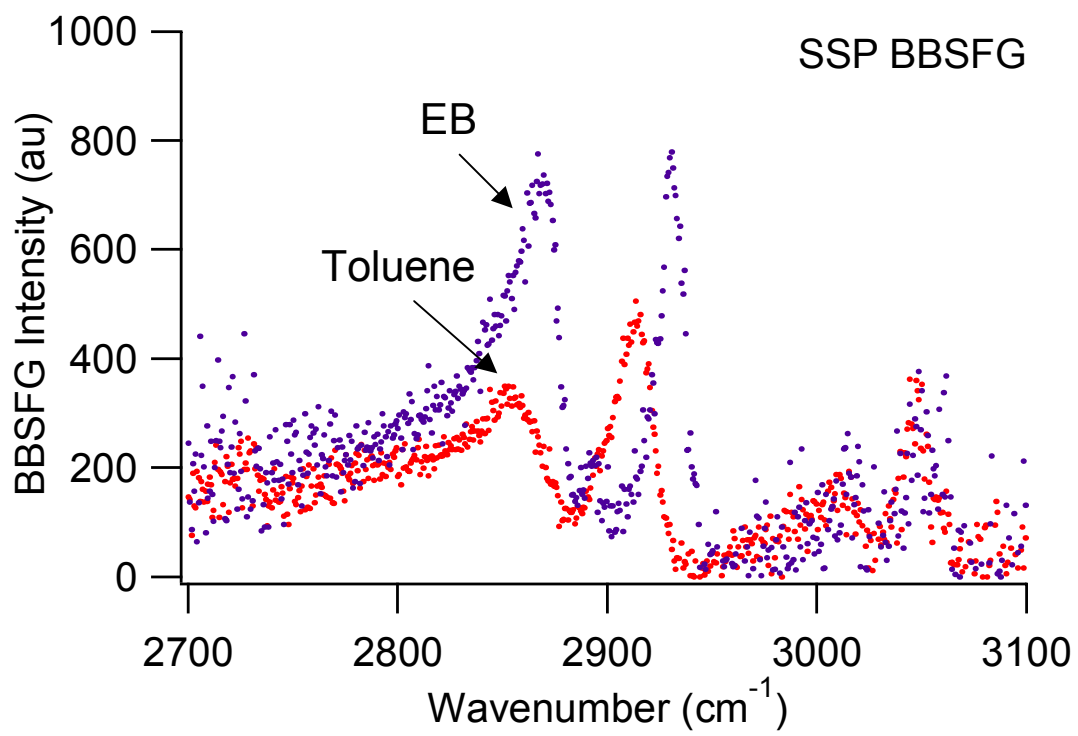


Figure 5.2: The surface $S_{\text{SFG}}S_{\text{vis}}P_{\text{IR}}$ BBSFG spectra of toluene (red) and ethylbenzene (purple).

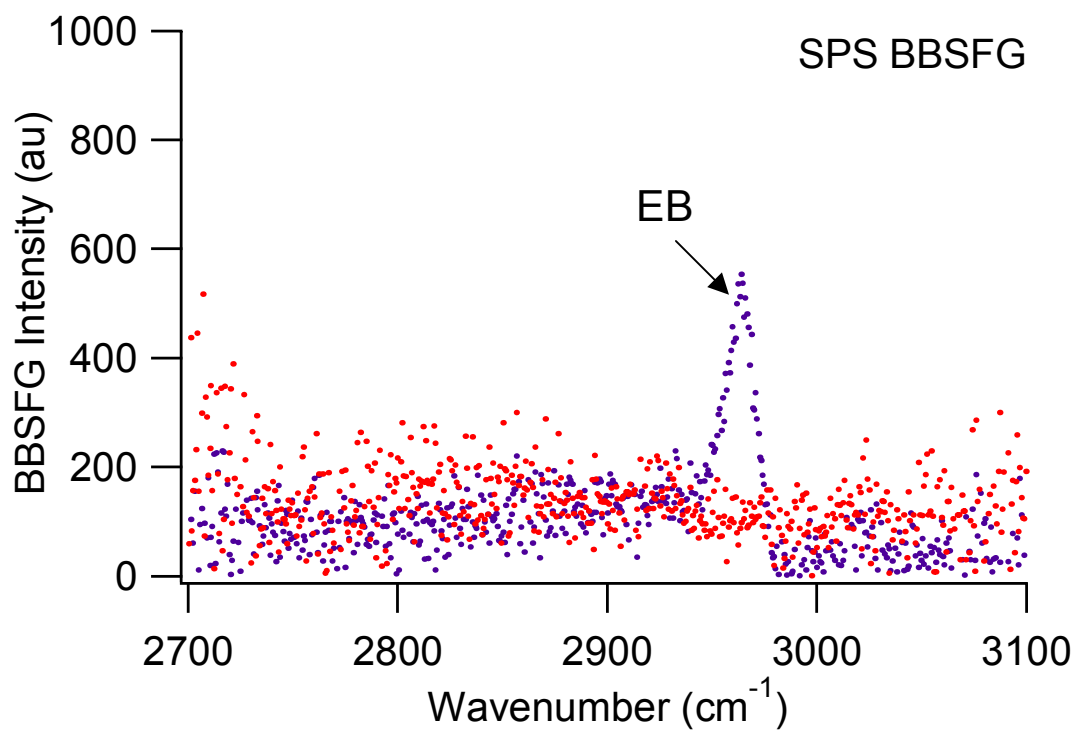


Figure 5.3: The surface $S_{\text{SFG}}P_{\text{vis}}S_{\text{IR}}$ BBSFG spectra of toluene (red) and ethylbenzene (purple)

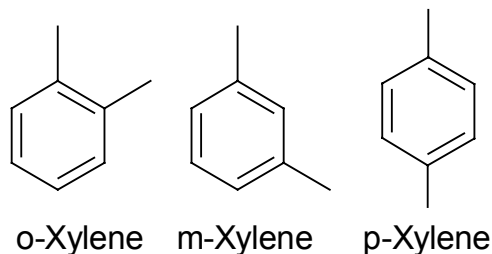
Conclusions

The experiments presented in this section indicate that the benzene ring is aligned in a similar orientational distribution for both the EB and toluene molecules in the liquid surface. This implies that the aromatic portion of the molecule drives the molecular orientation for monosubstituted benzene moieties. Further investigations, such as propyl and higher alkyl substituted benzenes are necessary to elucidate this effect.

5.2: Xylenes

Results and Discussion

The Raman and surface BBSFG spectra of the o-xylene, m-xylene, and p-xylene are shown from 2700 cm^{-1} to 3100 cm^{-1} in Figure 5.4. The BBSFG data are shown with red data points and the Raman data are shown with a blue line in all three of the graphs. The top graph is o-xylene, the middle graph is m-xylene, and the bottom graph is p-xylene.



The Raman spectrum of o-xylene is shown in Figure 5.4 and has two peaks below 2900 cm^{-1} that are attributed to overtone and combination bands. The fundamental CH_3 stretching modes occur between 2900 cm^{-1} and 3000 cm^{-1} . The peak assigned to the CH_3 -symmetric stretching mode (SS) is the strong peak observed around 2933 cm^{-1} and the peaks assigned to the CH_3 -asymmetric stretching modes (AS) are the two smaller peaks, one of which is a shoulder and both are observed above 2933 cm^{-1} . The aromatic CH stretching modes are observed above 3000 cm^{-1} . The o-xylene BBSFG spectrum

superimposed on the top graph in Figure 5.4 also shows a structured BBSFG spectrum in the aliphatic region. The overtone modes are resolved into two peaks. A peak is observed in the BBSFG spectrum around 2925 cm^{-1} , which is assigned to the $\text{CH}_3\text{-SS}$ mode and a dip is observed near the predicted peak position for the $\text{CH}_3\text{-AS}$. The dip observed in the spectrum is indicative of destructive interference between the two modes. This interference is expected due to the relative phase between the $\text{CH}_3\text{-SS}$ and the $\text{CH}_3\text{-AS}$ modes. The aromatic region appears to lack structure.

The Raman spectrum of m-xylene shown in Figure 5.4 contains overtones and combination bands below 2900 cm^{-1} , the fundamental CH_3 stretching modes between 2900 cm^{-1} and 3000 cm^{-1} , and the aromatic CH stretching modes above 3000 cm^{-1} . The BBSFG spectrum shown in Figure 5.4 shows a strong peak associated with the combination band observed in the Raman spectrum and another strong peak assigned to the $\text{CH}_3\text{-SS}$ mode. A dip is observed in the BBSFG spectrum near the predicted peak position from the $\text{CH}_3\text{-AS}$ mode. This dip is expected due to destructive interference between the $\text{CH}_3\text{-SS}$ and the $\text{CH}_3\text{-AS}$ modes. One peak is observed in the BBSFG spectrum above 3000 cm^{-1} , which assigned to an aromatic CH stretching mode.

The Raman spectrum of p-xylene shown in Figure 5.4 closely resembles the m-xylene Raman spectrum below 3000 cm^{-1} and the Raman spectrum in the aromatic region looks distinctly different from both of the other xylene Raman spectra. The combination and overtone modes are observed in the p-xylene Raman spectrum and the $\text{CH}_3\text{-SS}$ mode ($\sim 2920\text{ cm}^{-1}$) is well defined with a broad shoulder on the higher energy side assigned to the $\text{CH}_3\text{-AS}$ modes ($\sim 2950\text{ cm}^{-1}$ and $\sim 2970\text{ cm}^{-1}$). The BBSFG spectrum also shown in Figure 5.4 contains the aliphatic peaks predicted by referring to the Raman spectrum with

the destructive interference between the peaks attributed to the CH₃-SS interfering with the CH₃-AS modes.

The surface BBSFG intensity from o-xylene and m-xylene were not surprising. The molecules possess vibrational modes, which are both Raman and IR active. The surface BBSFG intensity from the p-xylene is an unexpected result. The p-xylene molecule contains an inversion center, which results in the vibration to be either Raman or IR active, thus none of its modes are predicted to be SFG active. Recall from chapter 4 that benzene also demonstrates a SFG response at the air-liquid interface. This SFG response for benzene is attributed to the asymmetry of the interfacial region.³⁰ The molecules at the p-xylene air-liquid interface are also effected by the asymmetry of the interfacial region, thus breaking the inversion symmetry and allowing the vibrational modes to be detected using surface BBSFG spectroscopy. Furthermore, the BBSFG response for the CH₃-SS mode for each of the methyl groups in p-xylene is larger because of inefficient cancellation between the methyl groups positioned on the air-side of the interface and the methyl groups buried in the liquid-side of the interface. Recall from Chapter 4 that the methyl groups on mesitylene (1,3,5-trimethylbenzene) did not efficiently cancel the methyl groups on the opposite side of the interface.

It is also interesting to note that the peak attributed to the CH₃-SS mode has the same relative intensity for all three of the xylene compounds investigated. The intensity of the CH₃-SS is predicted to be lower for the m-xylene and zero for p-xylene. The methyl groups are positioned on the benzene ring where using a vector addition model, the magnitude of the vector is entirely canceled out for p-xylene and partially cancelled out for m-xylene. The detection of the CH₃-SS verifies that the molecules are aligned on

average with the aromatic rings tilted relative to the surface plane. Recall from Chapter 4 that the transition dipole of the CH₃-SS is contained in the plane that contains the benzene ring, thus detection of the CH₃-SS using S_{SFG}S_{vis}P_{IR} polarization requires that the molecules be on average tilted from the surface plane. Furthermore, detection of the aromatic CH peaks only occurs when the molecule is tilted from the surface plane when using the S_{SFG}S_{vis}P_{IR} polarization. The higher intensity of the aromatic peaks for m-xylene as compared to o-xylene and the same intensity of the CH₃-SS for both compounds (m-xylene is predicted to be lower than o-xylene) indicates that the m-xylene molecules have a larger average tilt from the surface plane as compared to the average tilt of o-xylene molecules from the surface plane.

Conclusions

The investigation of o-xylene, m-xylene, and p-xylene has shown that the molecules on average are tilted from the surface plane. The o-xylene appears to have the smaller relative tilt angle from the surface plane as compared to m-xylene. The results from p-xylene were surprising, since the BBSFG theory predicted no SFG response from p-xylene indicating that the interface induces a dipole in p-xylene.

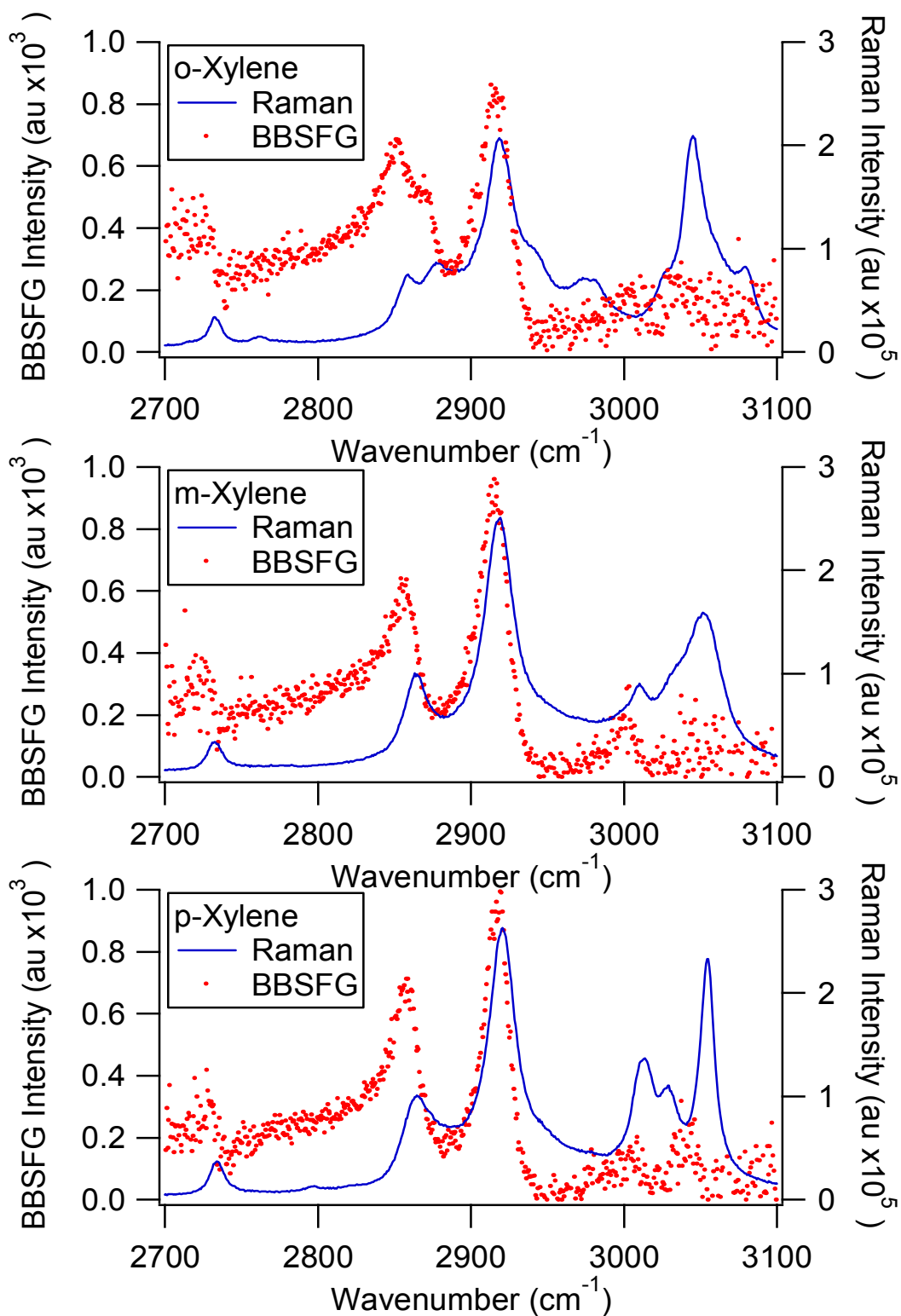


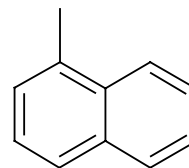
Figure 5. 4: Raman and surface BBSFG spectra of the xylenes. The red data points represent the BBSFG spectra and the blue line represents the Raman spectra. Top graph is o-xylene, middle graph is m-xylene, and the bottom is p-

CHAPTER 6

OBSERVATION OF THE HYDROPHOBIC EFFECT AT THE AIR–HYDRATED 1-METHYL NAPHTHALENE INTERFACE

Introduction

The 1-methyl naphthalene investigation is the first surface study of a polycyclic aromatic hydrocarbon using vibrational sum frequency generation spectroscopy. The ability to observe molecular average orientation at a liquid interface is an exciting prospect. Furthermore, the ability to observe the effect on the surface structure by adding another compound, such as water, is even more exciting. The results of this investigation are discussed in detail in this chapter.



1-Methyl Naphthalene

Experimental

Chemicals. The 1-methyl naphthalene (1-MN) was obtained from Acros Organics with a purity of 97% ($\leq 3\%$ 2-MN) and was used as received. Nanopure water having resistivity of $18.2 \text{ M}\Omega\cdot\text{cm}$ was also used. The hydrated 1-MN solutions were prepared by placing approximately equal volumes of water and 1-MN in a glass container, which was vigorously agitated, sealed, and then allowed to settle overnight. The solubility of water in 1-MN is 0.0377 g in 100 g of 1-MN at 20°C .¹⁰² The 1-MN phase of the hydrated 1-MN

solution was extracted for use in these experiments using a 10 mL syringe. The partially dehydrated 1-MN solution was prepared by placing a vial containing the hydrated 1-MN phase in a boiling water bath for approximately 2-3 hours.

Instrumentation. The Raman spectra were obtained by using 45 mW from a 532 nm continuous wave laser (SP, Millennia II), a 500 mm monochromator (Acton Research, SpectroPro 500i; 600 g/mm grating blazed at 1 μm), and a liquid nitrogen cooled CCD camera (Roper Scientific, LN400EB, 1340 x 400 pixel array, back-illuminated, deep depletion CCD). Raman spectra were collected using a fiber optic (Inphotonics, RP 532-05-15-FC), which was coupled to the entrance slit of the monochromator. The slit width was set to 50 μm and the resulting spectral resolution was 4 cm^{-1} . The Raman spectra were acquired with 2-second exposures to the CCD. The laser system used to obtain the broadband sum frequency generation spectra has been previously described.^{87,14,61,68} The laser system used for the BBSFG experiments includes two regenerative amplifiers (SP, Spitfires). The amplifiers are seeded with sub 50 fs, 800 nm pulses from a Ti:Sapphire Oscillator (SP, Tsunami). The amplifiers are pumped using a Nd:YLF (SP, Evolution 30) laser operating at a kHz repetition rate. One of the amplifiers produces 85 fs, 800 nm broadband pulses ($\sim 300 \text{ cm}^{-1}$). The resulting pulses then pump an optical parametric amplifier (SP, OPA-800C) to produce a broadband infrared beam ($\sim 600 \text{ cm}^{-1}$, kHz) for the BBSFG experiments. The second amplifier is equipped with a mask that spectrally narrows the pulse (17 cm^{-1} and $\sim 2 \text{ ps}$). To further narrow the pulse spectrally, an additional mask was added to the compressor within this amplifier resulting in $\sim 5 \text{ cm}^{-1}$ spectral width pulses.⁶⁸ The infrared beam energy was 10 μJ and the visible beam energy was 115 μJ for this experiment. The infrared and the 800

nm beams were overlapped spatially and temporally on the liquid surface of interest. The resultant sum frequency was dispersed spectrally using a 500 mm monochromator equipped with a 1200 g/mm diffraction grating blazed at 750 nm (Acton Research, SpectroPro 500i) and the dispersed sum frequency light was collected using a liquid nitrogen cooled CCD camera (Roper Scientific, LN400EB, 1340 x 400 pixel array, back-illuminated CCD). The resultant polarization of the BBSFG signal was verified using a Glan laser polarizer. The BBSFG spectra were obtained during 5-minute acquisitions and 3 spectra were averaged.

Prior to collecting the BBSFG spectra from the solutions of interest, a non-resonant BBSFG spectrum from the surface of a GaAs crystal was obtained during each experimental session. The BBSFG spectra, which are then normalized with the GaAs spectrum, show a central region where the peaks are easily discernable above the noise. As one would expect, the edges of these normalized spectra are dominated by noise, thus only the central region is used for data presentation and interpretation.

The BBSFG spectra were calibrated using a polystyrene thin film and another non-resonant BBSFG spectrum from the same GaAs crystal. The calibration BBSFG spectrum was collected by placing a thin film of polystyrene (infrared absorption spectrum is well known) in the path of the infrared beam prior to beam overlap on the GaAs crystal. The resultant infrared beam is structured due to absorption by the polystyrene film, which leads to a structured non-resonant BBSFG spectrum from the GaAs crystal. The peak positions (dips) in the calibration GaAs BBSFG spectrum are used to calibrate the BBSFG spectra obtained during the same experimental session.

Results and Discussion

The Raman and surface BBSFG spectra of 1-methyl naphthalene (1-MN) are presented in Figures 1 and 2. The Raman spectrum of neat 1-MN, the Lorentzian fit, and the peaks from the deconvoluted spectral fit (Igor Pro 4.05A) are shown in Figure 6.1. A comparison of the fits calculated using the Voigt profile and the Lorentzian profile were made, and the Lorentzian profile fit the Raman data more effectively. The peak positions were obtained directly from the Lorentzian peak fits. The positions of the peaks observed in the Raman spectrum also agree with the infrared results of 1-MN previously published.¹⁰³

The Raman spectrum reveals several peaks in the CH stretching region. The assignments of these peaks were accomplished by considering peaks assignments for toluene.^{104,105} Methyl bending overtones and the aromatic CH stretching overtones also occur in the aliphatic CH stretching region. Furthermore, there is evidence of splitting of the symmetric stretching mode of the methyl group for the 1-MN molecule.¹⁰⁶ The peaks observed at 2733 cm^{-1} and 2850 cm^{-1} are assigned to an overtone of a methyl-bending mode and a combination band, respectively. The peak observed at 2900 cm^{-1} is assigned to the methyl symmetric stretching (SS) mode while the peak observed at 2922 cm^{-1} is assigned to an overtone of a methyl-bending mode in addition to the methyl SS. The peak observed at 2939 cm^{-1} is attributed to the overtone of an aromatic C=C stretching mode convoluted with a CH₃ asymmetric stretching (AS) mode, and the peak observed at 2971 cm^{-1} is assigned to a CH₃ AS mode. The peak observed at 3004 cm^{-1} is assigned to an overtone of the aromatic C=C stretching mode and the large peak at 3052 cm^{-1} is assigned to the aromatic C-H stretching modes.

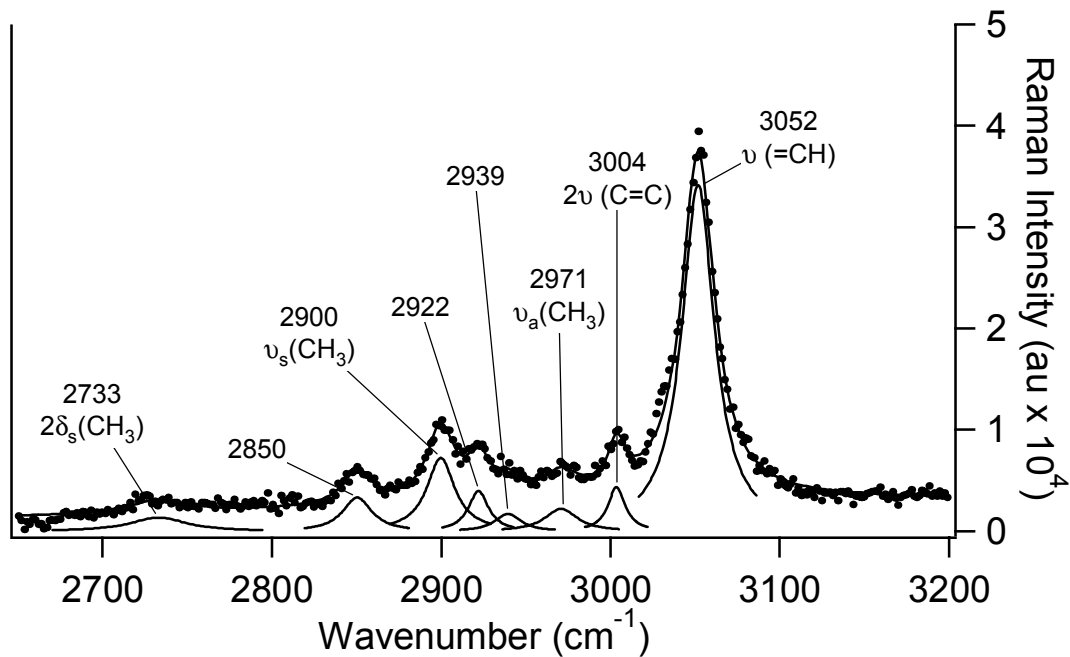


Figure 6.1. Neat 1-methyl naphthalene Raman spectrum (data points) with a Lorentzian peak profile and the deconvoluted peaks. The $2\delta_s$ represents the overtone of the methyl symmetric bending mode, the ν_s is the methyl symmetric stretch, the ν_a is the methyl asymmetric stretch, 2ν (C=C) is the overtone of the carbon/carbon stretching mode, and ν (=CH) is the aromatic C-H stretching mode.

The BBSFG spectrum, $S_{\text{SFG}}S_{\text{vis}}P_{\text{IR}}$ polarized, of neat 1-MN is shown in Figure 6.2a with the Raman spectrum (solid line) from Figure 6.1 superimposed. To our knowledge, this is the first published SFG spectrum of 1-MN. The fitting program used to fit this spectrum was written as a separate routine within Igor 4.05A to account for the coherent nature of the SFG, this is discussed in further detail in Appendix A. The data was fit using both a Lorentzian line shape and a Voigt line shape. The results using the Lorentzian line shape more accurately described the BBSFG data. Therefore, the fits shown in the inset of Figure 6.2a are Lorentzian profiles. The peak positions were taken from the calculated fits and the vibrational assignments were based on the Raman peak assignments as discussed above. The peaks at 2865 cm^{-1} , 2908 cm^{-1} , 2932 cm^{-1} , and 2967 cm^{-1} are assigned to an overtone of the methyl bending mode, a methyl symmetric stretching mode, another bending mode overtone and a methyl asymmetric stretching mode, respectively. The splitting of the CH_3 -SS mode in the Raman spectrum collapses to one CH_3 -SS peak in the BBSFG spectrum. The aromatic peaks discerned at 3010 cm^{-1} and 3061 cm^{-1} are attributed to an overtone of the $\text{C}=\text{C}$ stretching mode and the CH stretching mode, respectively. The CH_3 -AS mode at 2967 cm^{-1} is 180° out of phase with the other transitions in this spectrum, and is shown in the inset of Figure 6.2a. The real portion of the non-resonant (NR) contribution is in the same phase as the CH_3 -AS stretch and is therefore 180° out of phase with the other modes, and the imaginary portion is 180° out of phase from the real component of the NR SFG response.

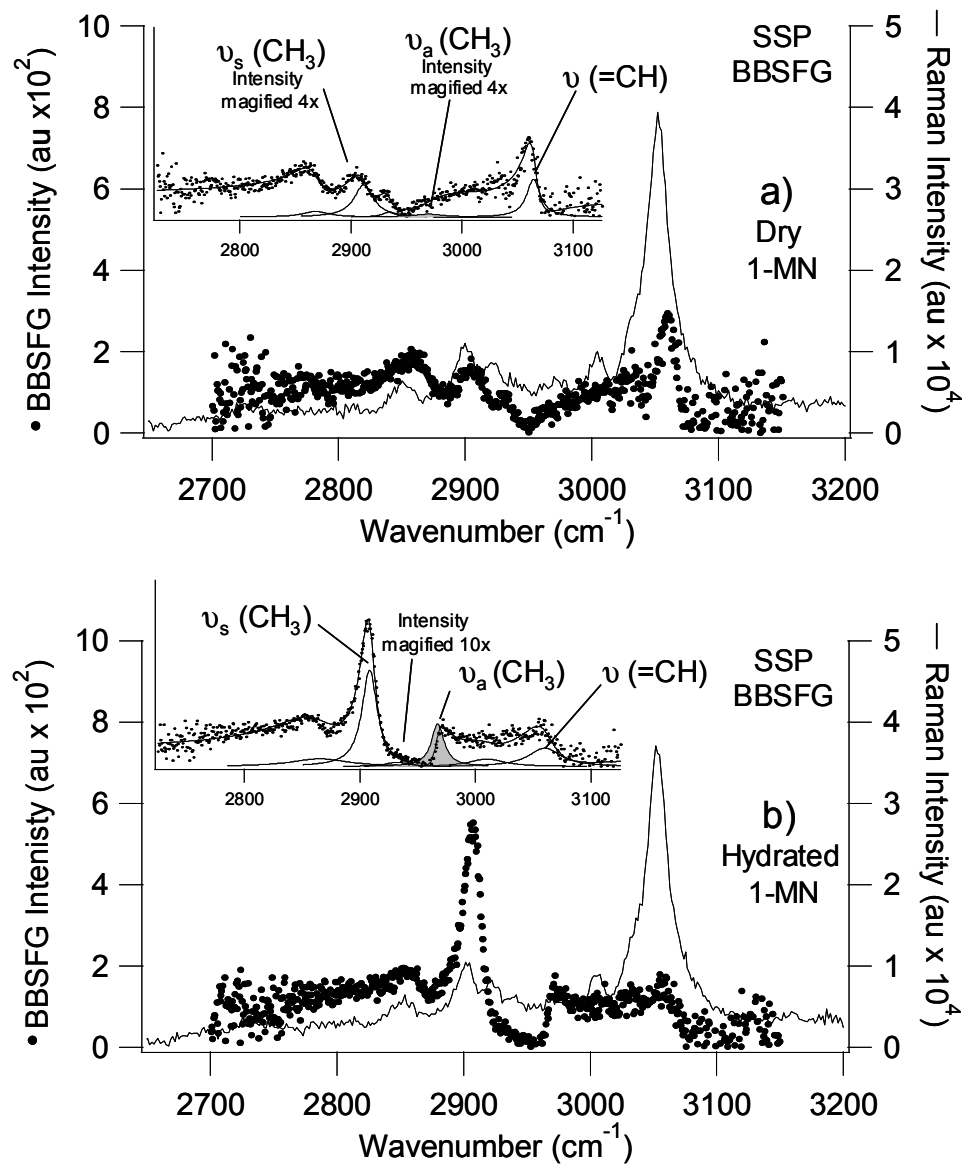


Figure 6.2. The solid lines in the main figures are the Raman spectra and data points are the surface $S_{SFG}S_{vis}P_{IR}$ BBSFG spectra of a) neat 1-methyl naphthalene and b) hydrated 1-methyl naphthalene. The Lorentzian peak fits for each of the BBSFG spectra are shown as solid lines in the inset. The inset in a) has both the symmetric (ν_s) and the asymmetric stretching (ν_a) peaks expanded 4x for clarity.

The peak positions of the vibrational modes of the surface 1-MN molecules shown in Figure 6.2a do in fact differ from the peak positions observed for the corresponding modes from the Raman spectrum. However, these BBSFG peak positions are typically within 10 cm^{-1} of the Raman peak positions. As one might expect, there are observed differences between the Raman spectrum and the BBSFG spectrum (Figure 6.2a) given that the Raman data describes the bulk environment and the BBSFG data describes the surface environment. Furthermore, the BBSFG is a coherent spectroscopy which gives rise to differences in the appearance of the BBSFG spectrum due to interference effects.^{107,108}

BBSFG spectra also reveal information about the orientation of the surface molecules. The p-polarized infrared beam used in the $S_{\text{SFG}}S_{\text{vis}}P_{\text{IR}}$ polarization combination has an infrared electric field vector component perpendicular to the surface plane, thus the transition moments perpendicular to the surface can efficiently interact with the electric field of the infrared pulse. The fact that the CH-SS and the CH₃-SS modes are observed in the $S_{\text{SFG}}S_{\text{vis}}P_{\text{IR}}$ polarized BBSFG spectrum shown in Figure 6.2a indicates that the 1-MN molecules do not lie flat in the plane of the interface. Yet, it is likely that these molecules are tilted relative to the surface. Recall from the SFG theory that the $S_{\text{SFG}}S_{\text{vis}}P_{\text{IR}}$ polarized BBSFG signal intensity is determined by both the orientation of the surface molecules and the surface number density. The observed intensity in the BBSFG spectrum of Figure 6.2a is relatively low even though the surface number density is high; the orientation of the 1-MN molecules is contributing to the observed BBSFG spectral shape and intensity. Drozdowski found using X-ray diffraction of the bulk 1-MN liquid that the molecules tend to stack on top of one another with the

methyl groups on alternating sides of the stack such that the dipoles of the 1-MN molecules are aligned anti-parallel as shown in the schematic of Figure 6.3a.¹⁰⁹ The surface of the neat 1-MN may also be arranged in a similar manner, which is inferred from the relatively low BBSFG signal strength from the CH₃-SS mode. However, the fact that we observe a BBSFG response indicates that the CH₃ moieties experience a different environment when exposed to the air as the CH₃ groups experience when buried into the liquid side of the interface. An ensuing polarizability change could enhance the observation of this extended dimer-like system in the stacking conformation with some tilt angle relative to the surface normal.

The Raman and the S_{SFG}S_{vis}P_{IR} polarized BBSFG spectra of the hydrated 1-MN are shown in Figure 6.2b. The hydrated 1-MN solution prepared according to the experimental section contains approximately 1 water molecule for every 336 1-MN molecules based on the solubility of water in 1-MN.¹⁰² (The solubility of 1-MN in water is much lower; 1 1-MN to $\sim 2.6 \times 10^5$ H₂O.^{110,111}) However, the Raman spectrum of the hydrated 1-MN and the neat 1-MN are indistinguishable from each other as observed by comparing the Raman spectra in Figures 2a and 2b. (We have also obtained Raman spectra in the OH bonding regions and do not observe any contribution from these regions of the spectrum from water absorption.) Yet, the surface BBSFG spectrum dramatically changes upon saturation of 1-MN with water as observed by comparing the BBSFG spectra in Figures 6.2a and 6.2b. The BBSFG peak positions and their vibrational assignments shown within the Figure 6.2 insets are unaffected, yet a change in the relative peak intensities is observed; therefore, the peaks assignments are the same as that for the dry 1-MN BBSFG spectrum shown in Figure 6.2a. As expected, the phase of the

peaks and the nonresonant response remains unaffected upon hydration. However, the peaks intensities of methyl stretches observed at 2908 cm^{-1} ($\text{CH}_3\text{-SS}$) and 2967 cm^{-1} ($\text{CH}_3\text{-AS}$) are enhanced, while the peak intensity of the aromatic CH stretch at 3063 cm^{-1} has decreased.

As revealed from Figure 6.2b, the hydration of the 1-MN solution affects the orientation of the 1-MN molecules at the surface, with undetectable effects to the bulk liquid as demonstrated by the BBSFG and the Raman spectra shown in Figures 6.2a and 6.2b. The increased $\text{CH}_3\text{-SS}$ and $\text{CH}_3\text{-AS}$ intensities in the $S_{\text{SFG}}S_{\text{vis}}P_{\text{IR}}$ polarized BBSFG spectrum from Figure 6.2b demonstrate an increased sensitivity of the SFG to the methyl groups at the surface of the hydrated 1-MN solution. This indicates an increased surface number density of the CH_3 groups at the air-liquid interface and is interpreted where the methyl groups on neighboring surface 1-MN molecules are adjacent to one another on the same side of the adjacent rings as shown in the schematic of Figure 6.3b. The result observed in Figure 6.2b also suggests that the 1-MN molecules do not lie flat in the interface, yet on average there is some tilt angle associated with the plane of this molecule relative to the surface normal. The $\text{CH}_3\text{-AS}$ peak intensity has also increased, and to the approximate extent that is observed for the $\text{CH}_3\text{-SS}$ peak as shown in the inset of Figure 6.2b. This infers that the average distribution of the tilt angles of the surface 1-MN molecules of the hydrated solution are similarly tilted relative to the surface normal as compared to the surface 1-MN molecules of the neat 1-MN solution. The SFG intensity of the $\text{CH}_3\text{-SS}$ is expected to be enhanced if the 1-MN molecules are stacked as shown in Figure 6.3b. The surface was also investigated using capillary rise method to discern any change in surface tension upon hydration. Within our experimental error, we

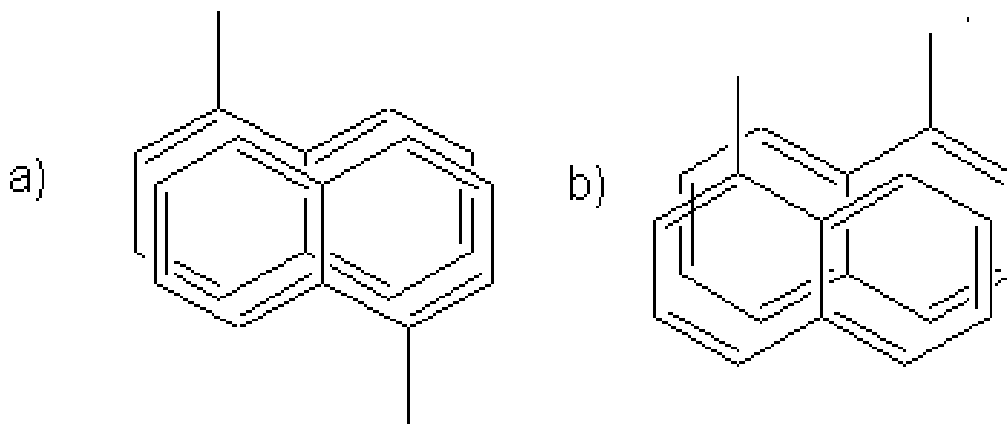


Figure 6.3. Proposed stacking of the 1-methyl naphthalene molecules at the surface of a) neat 1-methyl naphthalene and b) hydrated 1-methyl naphthalene. The plane of the surface is perpendicular to the aromatic rings.

were unable to detect a change in surface tension. In addition, ^1H nuclear magnetic resonance (NMR) studies were attempted to further quantify the hydration content; however, the small changes in the water peak in the ^1H NMR spectrum were smaller than the error of the integration since trace amounts of water are present in NMR solvents. In spite of this, it is clear the surface structure has changed significantly by the observations of the changes to the $S_{\text{SFG}}S_{\text{vis}}P_{\text{IR}}$ polarized surface BBSFG spectrum from the hydrated 1-MN solution.

To further investigate the orientation of the surface 1-MN molecules of the hydrated solution relative to the neat 1-MN liquid, additional BBSFG spectra were acquired using the $S_{\text{SFG}}P_{\text{vis}}S_{\text{IR}}$ polarization combination. The $S_{\text{SFG}}P_{\text{vis}}S_{\text{IR}}$ BBSFG spectra of both the water-saturated 1-MN and the neat 1-MN solutions were collected and the

resultant spectra are shown in Figure 6.4. The hydrated 1-MN (Figure 6.4b) has one well-resolved peak at 2970 cm^{-1} which is attributed to the CH₃-AS, consistent with the $S_{\text{SFG}}S_{\text{vis}}P_{\text{IR}}$ BBSFG data, while the spectrum of the neat 1-MN (Figure 6.4a) is somewhat featureless.

Recall that the transition moment of the CH₃-SS is along the methyl group central axis and a component of the transition moment of the CH₃-AS is perpendicular to the methyl group central axis. The $S_{\text{SFG}}P_{\text{vis}}S_{\text{IR}}$ polarization combination contains s-polarized infrared light relative to the surface plane, which means that the electric field vector for the infrared beam is in the plane of the surface and the infrared light interacts efficiently with modes that have components in the plane of the surface. The enhancement of only the CH₃-AS mode using $S_{\text{SFG}}P_{\text{vis}}S_{\text{IR}}$ polarized BBSFG and the lack of intensity for the CH₃-SS strongly suggests that the CH₃ groups of the surface 1-MN molecules from the hydrated solution are preferentially aligned with an average distribution that lies closer to the surface normal relative to the surface 1-MN molecules from the neat 1-MN liquid. This reorientation of the 1-MN surface molecules has clearly occurred after hydration of the 1-MN solution even though the water content is relatively small.

The BBSFG, $S_{\text{SFG}}S_{\text{vis}}P_{\text{IR}}$ polarization, spectrum was also obtained for a partially dehydrated water-saturated 1-MN solution to further elucidate this reorientation phenomenon. The $S_{\text{SFG}}S_{\text{vis}}P_{\text{IR}}$ BBSFG spectra of this solution along with $S_{\text{SFG}}S_{\text{vis}}P_{\text{IR}}$ BBSFG spectra from the neat 1-MN liquid and hydrated 1-MN solution are shown in Figure 6.5. Figure 6.5a shows the $S_{\text{SFG}}S_{\text{vis}}P_{\text{IR}}$ BBSFG spectrum from the neat 1-MN (untreated) liquid. Figure 6.5b shows the $S_{\text{SFG}}S_{\text{vis}}P_{\text{IR}}$ BBSFG spectrum from the water-saturated 1-MN solution after partial dehydration, and Figure 6.5c shows the $S_{\text{SFG}}S_{\text{vis}}P_{\text{IR}}$

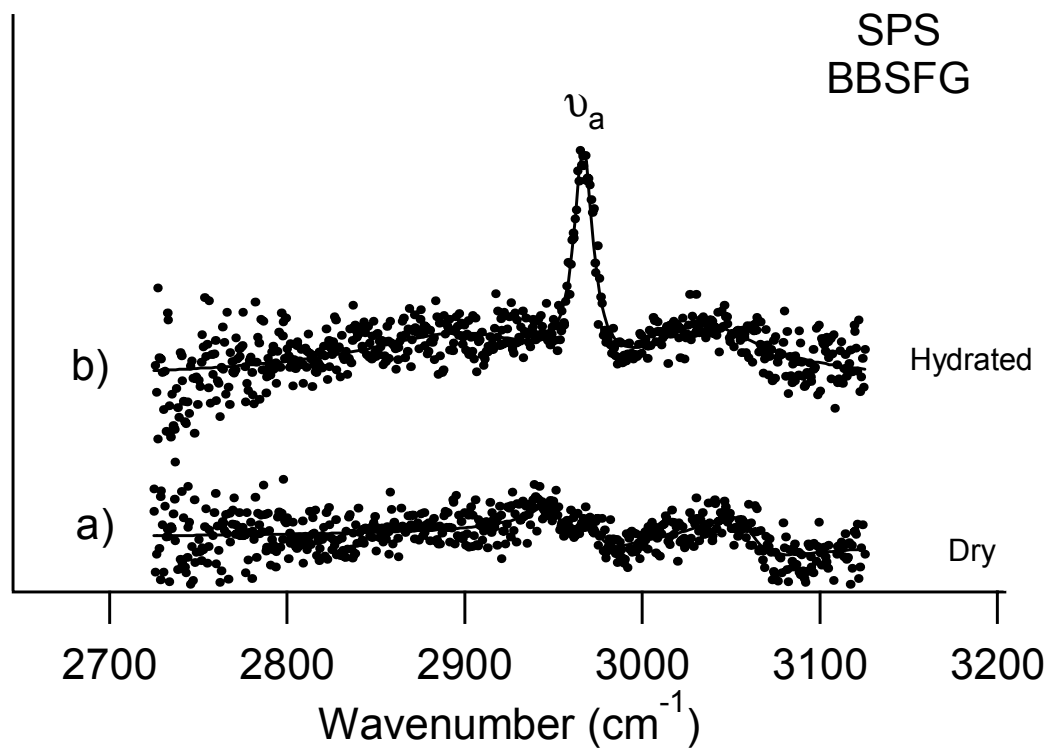


Figure 6.4: Surface $S_{\text{SFG}}P_{\text{vis}}S_{\text{IR}}$ BBSFG spectra of a) neat (dry) 1-methyl naphthalene and b) fully hydrated (wet) 1-methyl naphthalene are shown. The only discernable peak is the asymmetric stretching mode of the methyl group and is shown in b).

BBSFG spectrum from the fully hydrated 1-MN solution. The BBSFG intensities of the $\text{CH}_3\text{-SS}$ and the $\text{CH}_3\text{-AS}$, observed at 2908 cm^{-1} and 2967 cm^{-1} for spectrum 5b are larger than these peaks observed from the spectrum from the neat 1-MN liquid (Figure 6.5a) and smaller than these peaks observed from the spectrum of the fully hydrated 1-MN solution (Figure 6.5c). While on the other hand, the CH aromatic stretching vibration observed at 3063 cm^{-1} is smaller than the CH aromatic peak observed from the spectrum of the neat 1-MN (Figure 6.5a) and is slightly larger than the peak observed in the spectrum from the fully hydrated 1-MN solution (Figure 6.5c).

As observed in Figure 6.5, the increase of the peak intensity from the aromatic CH stretching mode and the reduction of the peak intensity from the methyl stretching modes upon partial dehydration of the fully water-saturated 1-MN solution strongly indicates that the hydration process is reversible for 1-MN solutions. (The solution was first fully hydrated and then partially dehydrated as described in the Experimental Section.) Although the BBSFG intensities of the observed peaks are changing with the level of hydration, frequency shifts are not observed, and this confirms that the water has neither reacted nor perturbed the solvation of the 1-MN molecules. Furthermore, it is clear from the observations in Figures 6.5a, 6.5b, and 6.5c, that the level of hydration of the 1-MN solution influences the extent of the CH_3 orientation of the surface 1-MN molecules.

Atmospheric Implications. Many organic molecules emitted into the atmosphere partition between the gas and condensed phases in the atmosphere. These molecules can exist either in the particle phase, liquid phase, or possibly as a liquid coating at the surface of solid phase atmospheric particles. It has been shown that the surface of liquid

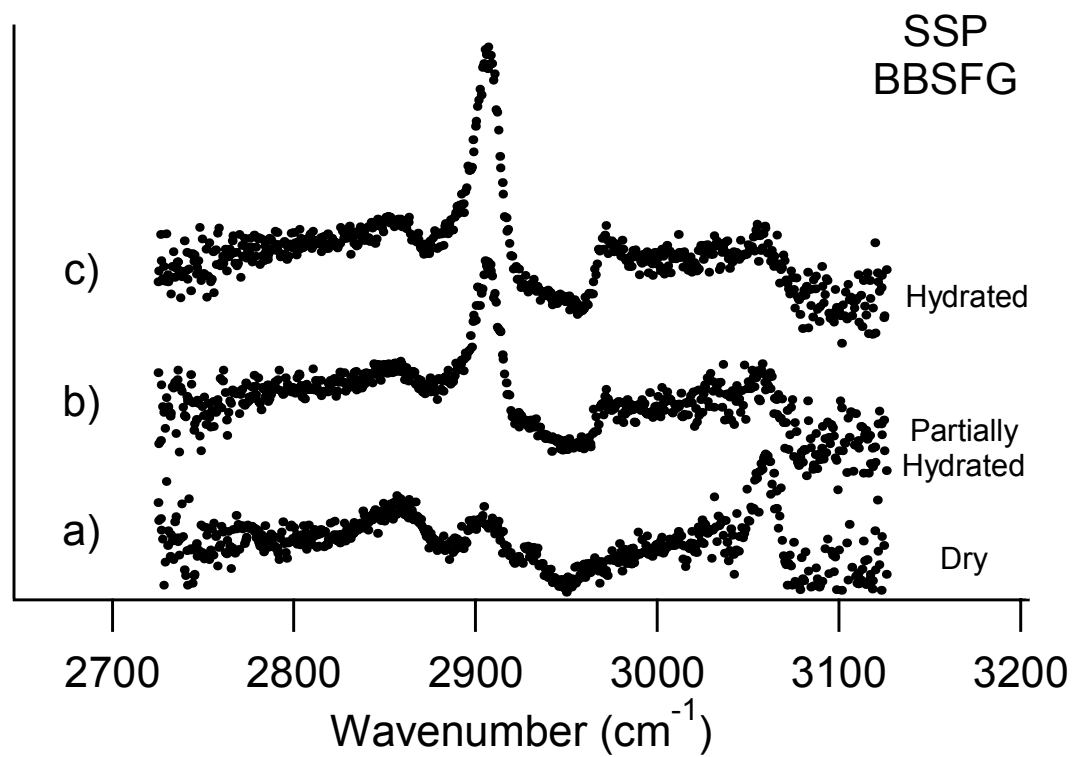


Figure 6.5: Surface $S_{SFG}S_{vis}P_{IR}$ BBSFG spectra of a) neat 1-methyl naphthalene, b) partially hydrated 1-methyl naphthalene, and c) fully hydrated 1-methyl naphthalene.

droplets (or liquid surfaces) play an important role in the evolution of aerosols in the atmosphere.⁵² When a potential reactant collides with the droplet surface, the reactant can diffuse into the drop, react on the surface or evaporate from the surface.^{52,51,112,113}

Preferred molecular orientations at the surface of such atmospheric aerosols are of interest since aerosol particles will encounter gas phase water molecules or may react with atmospheric oxidants. The uptake and reaction mechanisms are not well understood on these surfaces.¹¹⁴ Moreover, aerosol growth and reactivity may be affected by the surface structure if in fact the molecular orientation inhibits, enhances, or in any way alters the reaction pathway.

Water is among the most abundant trace species in the troposphere, and 1-MN, like many small PAHs, is a prevalent species in the lower troposphere of urban regions. The studies presented here indicate that the surface structure of a hydrophobic solution, such as 1-MN, or possibly that of an atmospheric aerosol, can be dramatically altered by small amounts of adsorbed and absorbed water. The increase in the surface number density of methyl groups from 1-MN as observed here and the preferred alignment of the methyl groups into the air phase after water absorption may alter the atmospheric fate of these and similar atmospherically prevalent alkylated PAHs. Certain reaction pathways, more typical of gas and bulk liquid phase PAHs, may be sterically hindered at the surface of an aerosol particle due to reorientation. Thus, the more common gas and liquid phase reaction pathways involving the aromatic CH groups are to be questioned for relevancy to the surface of an aerosol particle with alkyl aromatic species present since the CH groups may be less accessible at the surface of a hydrated organic aerosol. As shown in this study, the methyl groups dominate at the surface of a hydrated 1-MN solution and

therefore, the methyls will be more available for reaction with an incident gas phase oxidant as compared to the more abundant, but sterically hidden CH sites.

Conclusions

In summary, we have elucidated the surface structure of neat (pure) 1-methyl naphthalene (1-MN) and hydrated 1-MN liquids using broad bandwidth sum frequency generation spectroscopy, $S_{\text{SFG}}S_{\text{vis}}P_{\text{IR}}$ and $S_{\text{SFG}}P_{\text{vis}}S_{\text{IR}}$ polarized, in addition to the bulk structure of 1-MN using Raman spectroscopy. The surface 1-MN molecules of the neat 1-MN liquid have their aromatic rings stacked adjacent to one another with their methyl groups alternating out of the surface and into the subsurface region from molecule to molecule. With the introduction of relatively few water molecules into the 1-MN liquid (1 water: 336 1-MN) a rearrangement of the surface molecules is induced, leading to an increased number density of the methyl groups arranged such that more methyl groups are oriented in the same direction into the air phase at the air-liquid 1-MN interface. The observed hydrophobic effect, by the reorientation of 1-MN molecules at its hydrated solution surface, is not well understood. Yet, water appears to induce self-assembly of the surface 1-MN molecules. There are relatively few water molecules in the bulk and no direct evidence for water molecules being present in the surface region; however, it is clear that this hydrophobic reorientation is reversible through dehydration of the hydrated 1-MN solutions. Currently, we are investigating this reorientation phenomenon with several other aromatic hydrocarbon molecules at their respective air-liquid interfaces.

REFERENCES

- (1) Solomon, S. *Rev. Geophys.* **1999**, *37*, 275.
- (2) Solomon, S.; Garcia, R. R.; Rowland, F. S.; Wuebbles, D. J. *Nature* **1986**, *321*, 755.
- (3) Tolbert, M. A.; Toon, O. B. *Science* **2001**, *292*, 61.
- (4) Ravishankara, A. R. *Science* **1997**, *276*, 1058.
- (5) Luthy, R. G.; Aiken, G. R.; Brusseau, M. L.; Cunningham, S. D.; Gschwend, P. M.; Pignatello, J. J.; Reinhard, M.; Traina, S. J.; Weber Jr., W. J.; Westall, J. C. *Env. Sci. & Technol.* **1997**, *31*, 3341.
- (6) Richter, L. J.; Petralli-Mallow, T. P.; Stephenson, J. C. *Opt. lett.* **1998**, *23*, 1594.
- (7) Briggman, K. A.; Stephenson, J. C.; Wallace, W. E.; Richter, L. J. *J. Phys. Chem. B* **2001**, *105*, 2785.
- (8) Funk, S.; Bonn, M.; Denzier, D. N.; Hess, C.; Wolf, M.; Ertl, G. *J. Chem. Phys.* **2000**, *112*, 9888.
- (9) Bonn, M.; Hess, C.; Funk, S.; Miners, J. H.; Persson, B. N. J.; Wolf, M.; Ertl, G. *Phys. Rev. Lett.* **2000**, *84*, 4653.
- (10) Star, D.; Kikteva, T.; Leach, G. W. *Journal of Chemical Physics* **1999**, *111*, 14.
- (11) Hess, C.; Bonn, M.; Funk, S.; Wolf, M. *Chem. Phys. Lett.* **2000**, *325*, 139.
- (12) Hess, C.; Wolf, M.; Bonn, M. *Phys. Rev. Lett.* **2000**, *85*, 4341.
- (13) Van der Ham, E. W. M.; Vreken, Q. H. F.; Eiel, E. R. *Surf. Sci.* **1996**, *368*, 96.
- (14) Hommel, E. L.; Ma, G.; Allen, H. C. *Anal. Sci.* **2001**, *17*, 1325.

- (15) Li, Y. Q.; Zhang, H. Z.; Davidovits, P.; Jayne, J. T.; Kolb, C. E.; Worsnop, D. R. *J. Phys. Chem. A* **2002**, *106*, 1220.
- (16) Corsi, S. R.; Hall, D. W.; Geis, S. W. *Environmental Toxicology and Chemistry* **2001**, *20*, 1483.
- (17) Fisher, D. J.; Knott, M. H.; Turley, S. D.; Turley, B. S.; Yonkos, L. T.; Ziegler, G. P. *Environmental Toxicology and Chemistry* **1995**, *14*, 1103.
- (18) Kent, R. A.; Andersen, D.; Caux, P.-Y.; Teed, S. *Env. Tox.* **1999**, *14*, 481.
- (19) Fraser, M. P.; Cass, G. R.; Simoneit, B. R. T. *Environ. Sci. Technol.* **1998**, *32*, 2051.
- (20) Fraser, M. P.; Cass, G. R.; Simoneit, B. R. T.; Rasmussen, R. A. *Environ. Sci. Technol.* **1998**, *32*, 1760.
- (21) Bekins, B. A.; Cozzarelli, I. M.; Godsy, E. M.; Essaid, H. I.; Tuccillo, M. E. *J. Contam. Hydrol.* **2001**, *53*, 387.
- (22) Cozzarelli, I. M.; Bekins, B. A.; Baedecker, M. J.; Aiken, G. R.; Eganhouse, R. P.; Tuccillo, M. E. *J. Contam. Hydrol.* **2001**, *53*, 369.
- (23) Marianna, C. *Fresenius Environmental Bulletin* **2002**, *11*, 91.
- (24) Kim, Y. M.; Harrad, S.; Harrison, R. M. *Env. Sci. & Technol.* **2001**, *35*, 997.
- (25) Siegl, W. O.; Hammerle, R. H.; Herrmann, H. M.; Wenclawiak, B. W.; Luers-Jongan, B. *Atmos. Environ.* **1999**, *33*, 797.
- (26) Schauer, J. J.; Kleeman, M. J.; Cass, G. R.; Simoneit, B. R. T. *Environ. Sci. Technol.* **2002**, *36*, 1169.
- (27) Ueno, Y.; Horiuchi, T.; Niwa, O. *Anal. Chem.* **2002**, *74*, 1712.
- (28) Finlayson-Pitts, B. J.; Pitts Jr., J. N. Chemistry of the Upper and Lower Atmosphere: Theory, Experiments and Applications. In *Chapter 10: Airborne Polycyclic Aromatic Hydrocarbons and Their Derivatives*; Academic Press: San Diego, CA, 2000; pp 436.
- (29) Basak, S. C.; Grunwald, G. D.; Gute, B. D.; Balasubramanian; Opitz, D. *J. Chem. Inf. Comput. Sci.* **2000**, *40*, 885.
- (30) Hommel, E. L.; Allen, H. C. *The Analyst* **Submitted**.
- (31) Cheng, L.-T.; Tam, W.; Stevenson, S. H.; Meredith, G. R.; Rikken, G.; Marder, S. R. *J. Phys. Chem.* **1991**, *95*, 10631.

- (32) Papadopoulos, M. G.; Waite, J. J. *Chem. Soc. Perkin Trans. II* **1988**, 1988, 2055.
- (33) Arey, J.; Atkinson, R.; Zielinska, B.; McElroy, P. A. *Environ. Sci. Technol.* **1989**, 23, 321.
- (34) Fraser, M. P.; Kleeman, M. J.; Schauer, J. J.; Cass, G. R. *Environ. Sci. Technol.* **2000**, 34, 1302.
- (35) Hawthorne, S. B.; Grabanski, C. B. *Environ. Sci. Technol.* **2000**, 34, 4348.
- (36) Forstner, H. J. L.; Flagan, R. C.; Seinfeld, J. H. *Environ. Sci. Technol.* **1997**, 31, 1345.
- (37) Smith, D. J. T.; Harrison, R. M. In *Atmospheric Particles*; Harrison, R. M.; Ed.; IUPAC Series on Analytical and Physical Chemistry; John Wiley & Sons Ltd.: Chichester, England, 1998; Vol. 5; pp 253.
- (38) Wingfors, H.; Sjodin, A.; Haglund, P.; Brorstrom-Lunden, E. *Atmospheric Environment* **2001**, 35, 6361.
- (39) Shihua, Q.; Jun, Y.; Gan, Z.; Jiamo, F.; Guoying, S.; Zhishi, W.; Tong, S. M.; Tang, U. W.; Yunshun, M. *Environmental Monitoring and Assessment* **2001**, 72, 115.
- (40) Kado, N. Y.; Okamoto, R. A.; Kuzmicky, P. A.; Rathbun, C. J.; Hsieh, D. P. H. *Chemosphere* **1996**, 33, 495.
- (41) Rhead, M. M.; Pemberton, R. D. *Energy & Fuels* **1996**, 10, 837.
- (42) Short, J. W.; Heintz, R. A. *Environ. Sci. Technol.* **1997**, 31, 2375.
- (43) Sauer, T. C.; Michel, J.; Hayes, M. O.; Aurand, D. V. *Environment International* **1998**, 24, 43.
- (44) Finlayson-Pitts, B. J.; Pitts Jr., J. N. *Chemistry of the Upper and Lower Atmosphere: Theory, Experiments and Applications*; 1 ed.; Academic Press: San Diego, CA, 2000.
- (45) Day, M. *New Scientist* **1998**, 158, 23.
- (46) Dockery, D. W.; Pope, C. A.; Xu, X. P.; Spengler, J. D.; Ware, J. H.; Fay, M. E.; Ferris, B. G.; Speizer, F. E. *New England Journal of Medicine* **1993**, 329, 1753.
- (47) Li, N.; Wang, M. Y.; Oberley, T. D.; Sempf, J. M.; Nel, A. E. *Journal of Immunology* **2002**, 169, 4531.

- (48) Yin, X. J.; Schafer, R.; Ma, J. Y. C.; Antonini, J. M.; Weissman, D. D.; Siegel, P. D.; Barger, M. W.; Roberts, J. R.; Ma, J. K. H. *Environ. Health Perspect* **2002**, *110*, 1105.
- (49) Gupta, P.; Harger, W. P.; Arey, J. *Atmos. Environ.* **1996**, *30*, 3157.
- (50) Atkinson, R.; Arey, J. *Environ. Health Perspect* **1994**, *102*, 117.
- (51) Boniface, J.; Shi, Q.; Li, Y. Q.; Cheung, J. L.; Rattigan, O. V.; Davidovits, P.; Worsnop, D. R.; Jayne, J. T.; Kolb, C. E. *J. phys. Chem. A* **2000**, *104*, 7502.
- (52) Kolb, C. E.; Davidovits, P.; Jayne, J. T.; Shi, Q.; Worsnop, D. R. *Progress in Reaction Kinetics and Mechanism* **2002**, *27*, 1.
- (53) Shen, Y. R. *The Principles of Nonlinear Optics*; 1st ed.; John Wiley & Sons: New York, 1984.
- (54) Bain, C. D. *J. Chem. Soc. Faraday Trans.* **1995**, *91*, 1281.
- (55) Dick, B.; Gierulski, A.; Marowsky, G. *Appl. Phys. B* **1985**, *38*, 107.
- (56) Hirose, C.; Akamatsu, N.; Domen, K. *Appl. Spectrosc.* **1992**, *46*, 1051.
- (57) Morita, A.; Hynes, J. T. *Chem. Phys.* **2000**, *258*, 371.
- (58) Shultz, M. J.; Baldelli, S.; Schnitzer, C.; Simonelli, D. *J. Phys. Chem. B* **2002**, *106*, 5313.
- (59) Lambert, A. G.; Neivandt, D. J.; Briggs, A. M.; Usadi, E. W.; Davies, P. B. *J. Phys. Chem. B* **2002**, *106*, 5461.
- (60) Richmond, G. L. *Chem. Rev.* **2002**, *102*, 2693.
- (61) Ma, G.; Allen, H. C. *J. Am. Chem. Soc.* **2002**, *124*, 9374.
- (62) Miranda, P. B.; Shen, Y. R. *J. Phys. Chem. B* **1999**, *103*, 3292.
- (63) Yang, C. S.-C.; Richter, L. J.; Stephenson, J. C.; Briggman, K. A. *Langmuir* **2002**, *18*, 7549.
- (64) Kim, G.; Gurau, M.; Kim, J.; Cremer, P. S. *Langmuir* **2002**, *18*, 2807.
- (65) Kim, J.; Kim, G.; Cremer, P. S. *J. Am. Chem. Soc.* **2002**, *124*, 8751.
- (66) Allen, H. C.; Raymond, E. A.; Richmond, G. L. *Current Opinion in Colloid & Interface Science* **2000**, *5*, 74.

- (67) Allen, H. C.; Raymond, E. A.; Richmond, G. L. *J. Phys. Chem.* **2001**, *105*, 1649.
- (68) Ma, G.; Allen, H. C. *J. Phys. Chem. B* **Submitted**.
- (69) Simonelli, D.; Baldelli, S.; Shultz, M. J. *Chem. Phys. Lett.* **1998**, *298*, 400.
- (70) Raduge, C.; Pflumio, V.; Shen, Y. R. *Chem. Phys. Lett.* **1997**, *274*, 140.
- (71) Hirose, C.; Akamatsu, N.; Domen, K. *J. Chem. Phys.* **1992**, *96*, 997.
- (72) Hirose, C.; Yamamoto, H.; Akamatsu, N.; Domen, K. *J. Phys. Chem.* **1993**, *97*, 10064.
- (73) Walker, R. A.; Smiley, B. L.; Richmond, G. L. *Spectroscopy* **1999**, *14*, 18.
- (74) Dederichs, F.; Friedrich, K. A.; Daum, W. *J. Phys. Chem. B* **2000**, *104*, 6626.
- (75) Gragson, D. E.; McCarty, B. M.; Richmond, G. L. *J. Am. Chem. Soc.* **1997**, *119*, 6144.
- (76) Conboy, J. C.; Messmer, M. C.; Richmond, G. L. *J. Phys. Chem. B* **1997**, *101*, 6724.
- (77) Cremer, P. S.; Su, X.; Somorjai, G. A.; Shen, Y. R. *J. Mol. Catal. A: Chem.* **1998**, *131*, 225.
- (78) Ruppachter, G.; Dellwig, T.; Unterhalt, H.; Freund, H.-J. *Stud. Surf. Sci. Catal.* **2000**, *130D*, 3131.
- (79) Wang, H.; Borguet, E.; Yan, E. C. Y.; Zhang, D.; Gutow, J.; Eisenthal, K. *B. Langmuir* **1998**, *14*, 1472.
- (80) Vogel, V. *Curr. Opin. Colloid Interface Sci.* **1996**, *1*, 257.
- (81) Tadjeddine, A. "Adsorption of anions and neutral molecules studied by SFG"; 217th ACS National Meeting, 1999, Anaheim, Calif.
- (82) Gragson, D. E.; McCarty, B. M.; Richmond, G. L. *J. Opt. Soc. Am. B* **1996**, *13*, 2075.
- (83) Van Der Ham, E. W. M.; Vreken, Q. H. F.; Eliel, E. R. *Opt. Lett.* **1996**, *21*, 1448.

- (84) Petralli-Mallow, T. P.; Briggman, K. A.; Richter, L. J.; Stephenson, J. C.; Plant, A. L. "Nonlinear optics as a detection scheme for biomimetic sensors: SFG spectroscopy of hybrid bilayer membrane formation"; Proc. SPIE-Int. Soc. Opt. Eng., 1999, Gaithersburg, MD, USA.
- (85) Eisenthal, K. B. *Chem. Rev.* **1996**, *96*, 1343.
- (86) Bain, C. D. *Surfactant Sci. Ser.* **1999**, *83*, 335.
- (87) Hommel, E. L.; Allen, H. C. *Anal. Sci.* **2001**, *17*, 137.
- (88) Shen, Y. R. *Solid State Communications* **1998**, *108*, 399.
- (89) Yeh, U. L.; Zhang, C.; Held, H.; Mebel, A. M.; Wei, X.; Lin, S. H.; Shen, Y. R. *J. Chem. Phys.* **2001**, *114*, 1837.
- (90) Lobau, J.; Wolfrum, K. *J. Opt. Soc. Am. B* **1997**, *14*, 2505.
- (91) Williams, C. T.; Yang, Y.; Bain, C. D. *Langmuir* **2000**, *16*, 23343.
- (92) Baldelli, S.; Schnitzer, C.; Shultz, M. J. *Chem. Phys. Lett.* **1999**, *302*, 157.
- (93) Baldelli, S.; Schnitzer, C.; Shultz, M. J.; Campbell, D. J. *J. Phys. Chem. B* **1997**, *101*, 10435.
- (94) Scatena, L. F.; Brown, M. G.; Richmond, G. L. *Science* **2001**, *292*, 908.
- (95) Shorter, J. A.; De Bruyn, W. J.; Ju, J.; Swartz, E.; Davidovits, P.; Worsnop, D. R.; Zahniser, M. S.; Kolb, C. E. *Env. Sci. & Technol.* **1995**, *29*, 1171.
- (96) Moise, T.; Rudich, Y. *J. Geophys. Res.* **2000**, *105*, 14667.
- (97) Hommel, E. L.; Allen, H. C. *J. Phys. Chem. B* **Submitted**.
- (98) Green, J. H. S. *Spectrochim. Acta, Part A* **1970**, *26*, 1523.
- (99) Varsanyi, G. *Assignments for Vibrational Spectra of Seven Hundred Benzene Derivatives*; John Wiley & Sons: New York, 1974; Vol. 1.
- (100) Hadad, C. M.; Damewood, J., James R.; Liebman, J. F. *Tetrahedron* **1989**, *45*, 1623.
- (101) Fuson, N.; Garrigou-Lagrange, C.; Josien, M. L. *Spectrochim. Acta, Part A* **1960**, *16*, 106.
- (102) Englin, B. A.; Plate, A. F.; Tugolukov, V. M.; Pryanishnikova, M. A. *Khim. Tekhnol. Topl. Masel* **1965**, *10*, 42.

- (103) Fox, J. J.; Martin, A. E. *J. Chem. Soc.* **1939**, 318.
- (104) Morrison, V. J.; Laposa, J. D. *Spectrochimica Acta* **1976**, 32A, 443.
- (105) Balfour, W. J.; Fried, Y. *Canadian Journal of Chemistry* **1994**, 72, 1218.
- (106) Galli, J.; Fruwert, J.; Geisler, G. *Zeitschrift fur Chemie* **1976**, 16, 57.
- (107) Brown, M. G.; Raymond, E. A.; Allen, H. C.; Scatena, L. F.; Richmond, G. L. *J. Phys. Chem. A* **2000**, 104, 10220.
- (108) Wolfrum, K.; Laubereau, A. *Chem. Phys. Lett.* **1994**, 228, 83.
- (109) Drozdowski, H. *Chem. Phys. Lett.* **2002**, 351, 53.
- (110) Mackay, D.; Shiu, W. Y. *J. Chem. Eng. Data* **1977**, 22, 399.
- (111) Schwarz, F. P. *J. Chem. Eng. Data* **1977**, 22, 273.
- (112) Gershenson, M.; Davidovits, P.; Jayne, J. T.; Kolb, C. E.; Worsnop, D. R. *J. Phys. Chem. A* **2001**, 105, 7031.
- (113) Nathanson, G. M.; Davidovits, P.; Worsnop, D. R.; Kolb, C. E. *J. Phys. Chem.* **1996**, 100, 13007.
- (114) Zhang, H. Z.; Li, Y. Q.; Davidovits, P.; Williams, L. R.; Jayne, J. T.; Kolb, C. E.; Worsnop, D. R. *J. Phys. Chem.* **2002**, submitted Dec-2002.
- (115) Armstrong, B. H. *J. Quant. Spectrosc. Radiat. Transfer* **1967**, 7, 61.
- (116) Bain, C. D.; Davies, P. B.; Ong, T. H.; Ward, R. N. *Langmuir* **1991**, 7, 1563.

APPENDIX A

COHERENT PEAK PROFILE FITS USING IGOR 4.05A

Sum frequency generation spectroscopy is a coherent process; therefore, traditional curve fitting routines cannot describe the SFG spectra. Most curve fitting routines fit each individual peak and the sum of the individual peaks describe the overall observed spectrum. Due to the coherency of SFG spectroscopy this is not adequate, thus it is necessary to include cross terms between the peaks to accurately describe the SFG spectra. This procedure is not available in commercially prepackaged analysis software. In order to fit the BBSFG spectra obtained in the experiments presented in this dissertation, it was necessary to write a program to fit the spectra.

A.1: The Lorentzian Profile

In the Lorentzian peak profile, the peak widths are based on the collisional broadening effects. Frequently, published SFG spectra are described using a coherent Lorentzian line shape. The common equation used to describe a Lorentzian profile is shown in equation (1), but for SFG spectroscopy, the equation in this form cannot be used.

$$\phi(\omega) = \frac{A_v}{(\omega_v - \omega)^2 + \Gamma_v^2} \quad (1)$$

The Lorentzian equation necessary for SFG spectroscopy is described with equation (2),⁷ where each peak is summed with the non-resonant contribution before the whole expression is multiplied by its complex conjugate. This equation allows for both

$$signal = \left| B_{NR} e^{i\varphi} + \left(\sum_{i=1}^v \frac{A_v}{\omega_v - \omega + i\Gamma_v} \right) \right|^2 \quad (2)$$

constructive and destructive interference between the peaks, depending on the phase of the transition. In both equations the strength and phase of the transition is denoted by A_v , the center frequency of the transition is denoted by ω_v , and the half width at half max is the square of the dampening factor, Γ_v . In equation (2), the $B_{NR} e^{i\varphi}$ represents the non-resonant contribution to the observed SFG response. In order to use the coherent Lorentzian peak profile described by equation (2) a separate routine needed to be written. This was accomplished using Igor Pro 4.05A. The program allows the user to write their own curve fitting routines. The routine written to perform the Lorentzian profile is shown below:

```
#pragma rtGlobals=1      // Use modern global access method.

function sfg_lor(w,x) : fitfunc

    wave w //coefficient wave for the lorentzian fit
           // term 0, 1 are the non resonant
           // 2, 5, 8, ... amplitude
           // 3, 6, 9, ... peak position
           // 4, 7,10,... lorentzian width
    variable x //Infrared frequency
    variable j = 2, np = (numpnts(w)-2)/3 //np is the number of peaks to be fit
    variable/c val // val is a holding variable for the fitting equation
    variable/c i = sqrt(-1) // defining the imaginary i
    val = w[0] + i*w[1] // the nonresonant wave

    do // Loop which collects the peaks into the holding variable val
        val += w[j]/(x-w[j+1]-i*w[j+2])
        j += 3
    while (j < np*3+1)
    return magsqr(val) // Returns the calculated fit back to Igor
End
```

A.2: The Voigt Profile

The Lorentzian line shape is accurate, but it may be lacking in a complete description for some SFG spectra. Thus the Voigt peak profile is also used to fit SFG spectra. The Voigt profile is a superposition of both Lorentzian line broadening effects and Gaussian line broadening effects and the basic equation is shown in equation (3) with equations (4) thru (6) to further illustrate the process of solving a Voigt line profile.¹¹⁵

$$\phi(\nu) = \frac{1}{\alpha_D} \sqrt{\frac{\ln 2}{\pi}} K(x, y) \quad (3)$$

$$K(x, y) = \frac{y}{\pi} \int_{-\infty}^{\infty} \frac{e^{-t^2}}{y^2 + (x-t)^2} dt \quad (4)$$

$$y = \frac{\alpha_L}{\alpha_D} \sqrt{\ln 2} \quad (5)$$

$$x = \frac{\nu - \nu_0}{\alpha_D} \sqrt{\ln 2} \quad (6)$$

The line broadening is denoted by α_D for Gaussian and α_L for Lorentzian line shapes and the center frequency is denoted by ν_0 . The Voigt profile does not contain an explicit solution; therefore, the fit requires a numerical approximation. The final equation used for the SFG spectra was taken from a paper from Bain et al¹¹⁶ and is shown in equation (7). The routine written in Igor Pro 4.05A used to calculate the Voigt profile is shown below.

$$I_{\text{SFG}} \propto |\chi_{\text{NR}}^{(2)}|^2 + \frac{\pi B_v^2}{2\sigma_v^2} [\text{Re}\{w_v(z)\}^2 + \text{Im}\{w_v(z)\}^2] + 2|\chi_{\text{NR}}^{(2)}|B_v \left(\frac{\pi}{2\sigma_v^2}\right)^{1/2} [\text{Re}\{w_v(z)\}\sin\theta - \text{Im}\{w_v(z)\}\cos\theta] \quad (7)$$

$$z = \frac{1}{(2\sigma_v^2)^{1/2}} (\omega - \omega_v + i\Gamma_v) \quad (8)$$

```
#pragma rtGlobals=1      // Use modern global access method.
```

```
function sfg_voigt(w,x) : fitfunc
```

```
  wave w //coefficient wave for the Voigt fit
```

```
    // term 0, 1 are the non resonant
```

```
    // 2 is the phase between the resonant and the nonresonant term
```

```
    // 3 is the Lorentzian width
```

```
    // 4, 7, 10 ... amplitude
```

```
    // 5, 8, 11 ... peak position
```

```
    // 6, 9, 12 ... Gaussian width
```

```
  variable x //Infrared frequency
```

```
  variable j = 4, np = (numpnts(w)-4)/3 //np is the number of peaks to be fit
```

```
  variable imVal, reVal, erfcz //imVal holding variable for the imaginary component
```

```
    //reVal for the real component of the Voigt
```

```
  variable/c non, val
```

```
  variable/c i = sqrt(-1) // Imaginary i definition
```

```
  non = w[0] + i*w[1] // the nonresonant wave
```

```
  reVal = 0;imVal = 0 // zero the holding variables
```

```
  // Loop which collects the peaks into the holding variables reVal and imVal
```

```
  do
```

```
    erfcz = erfc(w[3]/(sqrt(2)*w[j+2])) //calculates the error function
```

```
    val = sqrt(pi/2)*(w[j]/w[j+2])*exp(-0.5*((x-w[j+1]+i*w[3])/w[j+2])^2)*erfcz
```

```
    reVal += real(val)
```

```
    imVal += imag(val)
```

```
    j += 3
```

```
  while (j < np*3+2)
```

```
  // Returns the calculated fit back to Igor
```

```
  return reVal^2 + imVal^2 + 2*cabs(non)*reVal*sin(w[2]) - 2*cabs(non)*imVal*cos(w[2]) + magsqr(non)
```

```
End
```

A.3: Procedure – Using Igor 4.05A for SFG Data

This section is intended to walk someone through the routines written to fit SFG data in Igor using either the Voigt or the Lorentzian routine. It is not necessary to be familiar with Igor to follow this procedure.

1. Open data in Igor
 - a. Name the wave for your IR frequency as 'xwave'.
 - b. Name the wave for your SFG data as 'ywave'.
2. In the command line type 'make/d/n=x coef'.
 - a. For the Lorentzian profile, $x = 2 + 3 n$, where n is the number of peaks being fit.
 - b. For the Voigt profile, $x = 4 + 3 n$, where n is the number of peaks being fit.
3. Plot data by generating a new graph.
 - a. Click on "Windows".
 - b. Select "New Graph".
 - i. Highlight 'xwave' in the Xwave list.
 - ii. Highlight 'ywave' in the Ywave list.
 - iii. Click on "Add".
 - iv. Click on "Do It".
4. Perform curve fitting.
 - a. Click on "Analysis".
 - b. Select "Curve Fitting ...".
 - i. Select "Function and Data" tab.

1. Under the “Function” pull down menu, select fitting equation.
 - a. Voigt profile => “sfg_voigt”.
 - b. Lorentzian profile => “sfg_lor”.
 2. Under the “Ydata” pull down menu, select ‘ydata’.
 3. Under the “Xdata” pull down menu, select ‘xdata’.
- ii. Select “Coefficients” tab.
1. Under the “Coefficient” pull down menu, select ‘coef’.
 2. Enter initial guess for each coefficient. It is necessary to make a “good” first guess. Mark the box to the right of the initial for any value that the computer needs to hold constant during the fitting routine.
 3. Click on “Graph Now” to see a graph of the initial guess.
 4. Change any coefficient values and repeat step 3 if necessary.
 5. Click on “Do It”.
 6. Repeat steps 2-5 until an acceptable fit is achieved.

The computer graphs the calculated spectra and continues to update it during the entire curve fitting process. During each iteration, the ‘coef’ wave is updated with the new values. Upon completion of the calculated fit, a new wave is created and the program names it ‘W_Sigma’, which contains the standard deviation for each coefficient in the ‘coef’ wave. The specific wave names are designed to simplify the procedure and different names can be substituted, although that would be discouraged. The individual

peaks can be displayed on the graph by typing ‘plot_peaks()’ in the command line if the Voigt profile had been used in the procedure above. Type ‘plot_lor_peaks()’ in the command line if the Lorentzian profile had been used in the procedure above. The computer will give a “Function Execution Error” that “While executing RemoveFromGraph the following error occurred: trace is not on graph” click on “OK” and ignore message. The process of fitting and plotting can be repeated as many times as necessary to achieve a desirable fit. It does take time getting used to the process and deciding on a “good” initial guess.

The routine written to plot the individual peaks calculated using the Lorentzian profile is shown below:

```
#pragma rtGlobals=1 // Use modern global access method.

function plot_lor_peaks()
    wave coef, xwave
    RemoveFromGraph peak1, peak2, peak3, peak4, peak5, peak6, peak7, peak8
    killwaves f_x
    variable np = (numpnts(coef)-2)/3 //np is the number of peaks to be fit
    variable xnp = numpnts(xwave)
    variable/d imVal, reVal, erfcZ, x
    variable/d/c non = 0, val = 0
    variable/d/c i = sqrt(-1) // defining the imaginary i
    make/d/n=(xnp,np) f_x
    non = coef[0] + i*coef[1] // the nonresonant wave
    variable k = 0 , j = 2, m = 0
    do
        k = 0
        val = 0
        do
            val = coef[j]/(xwave[k]-coef[j+1]-i*coef[j+2])
            f_x[k][m] = magsqr(val)
            k+=1
        while (k < xnp)
        j += 3
        m += 1
    while (j < np*3+2)
    k = 0
    killwaves peak1, peak2, peak3, peak4, peak5, peak6, peak7, peak8, peak9, peak10, peak11,
    peak12
```

```

    make/d/n=(xnp) peak1, peak2, peak3, peak4, peak5, peak6, peak7, peak8, peak9, peak10,
    peak11, peak12
    peak12 = coef[0]^2
    do
        j = 0
        do
            peak1[j] = f_x[j][0]
            peak2[j] = f_x[j][1]
            peak3[j] = f_x[j][2]
            peak4[j] = f_x[j][3]
            peak5[j] = f_x[j][4]
            peak6[j] = f_x[j][5]
            peak7[j] = f_x[j][6]
            peak8[j] = f_x[j][7]
            peak9[j] = f_x[j][8]
            peak10[j] = f_x[j][9]
            peak11[j] = f_x[j][10]
            peak12[j] += f_x[j][k]
            j += 1
        while (j < xnp)
        k += 1
    while (k < np)
    AppendtoGraph peak1, peak2, peak3, peak4, peak5, peak6, peak7, peak8 vs xwave
    j = 0; k = 2
    do
        print j+1, coef[k], coef[k+1], coef[k+2]
        k+=3
        j+=1
    while (j < np)

```

End

The routine written to plot component peaks calculated using the Voigt profile is shown below:

```

#pragma rtGlobals=1    // Use modern global access method.

function plot_peaks()
    wave coef, xwave
    RemoveFromGraph peak1, peak2, peak3, peak4, peak5, peak6, peak7, peak12
    killwaves f_x, junk
    variable np = (numpnts(coef)-4)/3    //np is the number of peaks to be fit
    variable xnp = numpnts(xwave)
    variable/d imVal, reVal, erfciz, x
    variable/d/c non = 0, val = 0
    variable/d/c i = sqrt(-1)    // defining the imaginary i
    make/d/n=(xnp,np) f_x
    non = coef[0] + i*coef[1]    // the nonresonant wave
    variable k = 0, j = 4, m = 0
    make/c/n=(xnp) junk
    do
        k = 0

```

```

do
  x = xwave[k]
  erfcZ = erfc(coef[3]/(sqrt(2)*coef[j+2]))
  val = sqrt(pi/2)*(coef[j]/coef[j+2])*exp(-0.5*((xwave[k] -
coef[j+1]+i*coef[3])/coef[j+2])^2)*erfcZ
  reVal = real(val)
  imVal = imag(val)
  junk[k] = val
  f_x[k][m] = reVal^2 + imVal^2
  k+=1
while (k < xnp)
j += 3
m += 1
while (j < np*3+2)
k = 0
killwaves peak1, peak2, peak3, peak4, peak5, peak6, peak7, peak8, peak9, peak10, peak11,
peak12
make/d/n=(xnp) peak1, peak2, peak3, peak4, peak5, peak6, peak7, peak8, peak9, peak10,
peak11, peak12
peak12 = coef[0]^2
do
  j = 0
  do
    peak1[j] = f_x[j][0]
    peak2[j] = f_x[j][1]
    peak3[j] = f_x[j][2]
    peak4[j] = f_x[j][3]
    peak5[j] = f_x[j][4]
    peak6[j] = f_x[j][5]
    peak7[j] = f_x[j][6]
    peak8[j] = f_x[j][7]
    peak9[j] = f_x[j][8]
    peak10[j] = f_x[j][9]
    peak11[j] = f_x[j][10]
    peak12[j] += f_x[j][k]
    j += 1
  while (j < xnp)
  k += 1
while (k < np)
AppendtoGraph peak1, peak2, peak3, peak4, peak5, peak6, peak7, peak12 vs xwave
j = 0; k = 4
do
  print j+1, coef[k], coef[k+1], coef[k+2], coef[3]
  k+=3
  j+=1
while (j < np)

```

End